A SEARCH FOR HEAVY STABLE CHARGED PARTICLES PRODUCED IN PAIRS IN THE DECAY OF THE NEUTRAL INTERMEDIATE VECTOR BOSON Z

Thesis by
Eric Soderstrom

In Partial Fulfillment of the Requirements
for the Degree of
Doctor of Philosophy

California Institute of Technology
Pasadena, California

1991

(Submitted October 16, 1990)

To my parents Phil and Ruth Soderstrom

Abstract

A search for new stable charged particles produced in pairs in the decays of the intermediate vector boson Z is performed with the MARK II detector at the SLAC Linear Collider. Particle masses are determined from momentum, ionization energy loss and time-of-flight measurements. No candidates for new particles are found. A limit excluding the production of pairs of stable fourth generation charged leptons and stable mirror fermions with masses between the muon mass and 36.3 GeV/c^2 is set at the 95% confidence level. The production of pairs of stable supersymmetric scalar leptons with masses between the muon mass and 32.6 GeV/c^2 is also excluded at the 95% confidence level under the assumption that the left- and right-handed scalar leptons are degenerate in mass.

Acknowledgments

I would like to thank my advisor Barry Barish for giving me the opportunity to join the Caltech/MARK II group. For his guidance during my years at Caltech and SLAC and for giving advice while I was performing my thesis research and writing I offer additional thanks. Likewise, I would like to thank Ryszard Stroynowski for advising me, and for freely providing ideas and encouragement throughout my graduate career. I also thank him for much help with writing this thesis.

I would like to thank the rest of the Caltech/MarkII group as well for all they did to educate me, and also for their help in developing this thesis analysis. They are Professors Charlie Peck, Frank Porter and Alan Weinstein and post-docs Chris Hawkes, Michael Kuhlen, Janis McKenna, Barrett Milliken, Mark Nelson and Eric Wicklund. I particularly thank Janis McKenna for aiding me in performing the analysis and in writing a paper on it. I am especially grateful to Mark Nelson for getting me started on the MARK II hardware and software, and also to Ryszard Stroynowski and Eric Wicklund for all they did on the Time-of-Flight system. It has been a pleasure to know and work with the other Caltech/MARK II students Andrew Weir (aka "the thin man"), Ralph Wolf and House Dolly Wu (it was Andrew who first encouraged me to talk to Barry about joining the group).

I would like to thank all of the members of the MARKII Collaboration. At SLAC I thank Jonathan Dorfan and the rest of Group C for offering their hospitality and resources while I was there. Andy Lankford deserves special thanks for his invaluable assistance with the online systems. I also thank Rick Van Kooten and Dave Coupal for getting the dE/dx system into shape for this analysis.

I am very grateful to Gerry Abrams and John Seeman for introducing me to accelerator physics and fast feedback systems during my time with the SLC Linac group.

Down at the pit I would like to thank to Sean Dyer and his crew for all the fine

engineering support over the years and Bob Bejsovec for helping me out of a couple of tight spots with the electronics. I would also like to thank John Hanson, Hans Grau, Larry Mossbarger, Svend Sondergaard and Keith Warfield of the Caltech technical staff for the hard work they put into the design, construction, and installation of the TOF system.

I would like to thank Nina Adelman-Stolar of SLAC Public Affairs for giving me the chance to be a SLAC tour guide, and my friend Sam Braunstein for helping me with course work at Caltech.

I would like to thank all of my undergraduate Professors at the University of Minnesota, Duluth particularly Bo Casserberg, Thomas F. Jordan and Michael Sydor; it was Michael Sydor who first inspired me to become a physicist.

I would like to thank Charlotte Hee (aka CHEE) for help on the computer and also for adventures on foot and many fine meals and whatnot. To my housemates Paul Weber (alias PXW) and Bill Gabella: thanks for the same kind of everything like that.

I would like to thank my sister for her love and friendship over the years and for visiting me several times in California.

I would like to thank my wife Lisa Michael for her friendship and the love she has given me since I met her (at one of the Pat Burchat *et al.,* SLAC Halloween parties). It is she I love most of all and I am happy that we have a daughter Blake together.

I dedicate this thesis to my parents Phil and Ruth Soderstrom.

Table of Contents

List of Tables

List of Figures

Chapter 1

Introduction

This thesis presents the results of a direct experimental search for new stable charged particles produced in pairs in Z boson decay. The search is performed using the MARK II detector at the SLAC Linear Collider. It is motivated by the fact that, should any of these new particles be found, the knowledge of their existence may help in providing answers to some of the outstanding fundamental questions in the field of elementary particle physics. It is also motivated by the fact that the copious production of the Z boson opens a new energy range for searches for new particle production in the clean environment of e^+e^- colliding beam experiments.

1.1 Thesis outline

We begin this thesis in Chapter 2 with an introduction to the methods used to search for the production of pairs of new stable charged particles in Z boson decay. We then try to motivate the search by discussing theories which predict the existence of new stable charged particles. All of these theories are extensions of the current Standard Model of the weak and electromagnetic interactions. Previous searches for stable charged particles, also summarized here, do not rule out the production of such objects in Z boson decay.

In Chapter 3 we focus on deriving the mathematical formulæ needed to predict the new particle production rates in Z boson decay. We derive the differential cross-section for fermion-antifermion production through electron-positron annihila-

tion. This leads to expressions for the total cross-section for Z production and the Z partial decay widths. We then discuss the radiative corrections to these expressions before presenting the measurement of the Z total cross-section at the SLC based on the luminosity and center-of-mass energy of the e^+e^- collisions.

In chapters 4 and 5 we present detailed descriptions of the experimental apparatus used to carry out our search. The SLAC Linear Collider (SLC) and the MARK II detector are described in Chapter 4, followed by a description of the MARK II time-of-flight system in Chapter 5.

In Chapters 6 and 7 we discuss the details of the analysis of the data. We begin in Chapter 6 with a description of our data sample. This is followed by a discussion of the data reduction procedures that are used eliminate most of the background that constitutes the bulk of the data. In Chapter 7 we discuss the maximum likelihood method used to determine the masses of the particles in events having a stable charged pair production topology. We then determine if there is any evidence for the production of heavy stable charged particles. We present the final results of our search in terms of limits on the predictions derived from extensions of the Standard Model.

We conclude this thesis in Chapter 8 by discussing the results of our search in terms of their implication to the problems and extensions of the Standard Model.

Two appendices to this thesis are also included. Appendix A contains the details of the Monte Carlo simulations used to test the search method. The discussion focuses on the comparisons between real and simulated data. Appendix B presents the methods used to determine the systematic errors on the efficiency of the candidate event selection and particle mass assignment procedure.

Chapter 2

Method and Motivation

In this chapter we present the methods used in the search for new stable charged particles with direct couplings to the intermediate vector boson Z. Such particles would be produced in pairs in Z boson decay. Next, in an attempt to motivate this general experimental search, we discuss theories which predict, or are at least compatible with, the existence of new stable charged particles. These theories must be in agreement with all existing experimental observations which are well described by the so-called Standard Model.[1] A brief outline of the Standard Model is therefore presented to serve as a foundation from which those other theories can be discussed.

The Standard Model, though very successful, depends on the explicit input of experimentally determined information. This is not satisfactory since it then fails to address several fundamental questions. One of these, for which there is no explanation, is what is the origin of the observed mass values of particles. Possibly related to this problem is the apparent grouping of these particles into families or generations. Another unexplained phenomenon is the non-conservation of parity in the weak interactions. This experimentally observed fact must be built into the theory explicitly.

Any attempt to overcome the above shortcomings with a broader theoretical framework has implications concerning the existence of new stable charged particles. This is also true of attempts to include the Standard Model in theories which can

offer a description of the gravitational interaction between massive particles. The new theories as discussed in the literature predict the existence of new particles but do not have any explicit predictions concerning their masses. However, in general, they do provide the strength of the coupling of such particles to the Z. This allows for the calculation of the production rate of such new particles in Z decays.

2.1 The search method

In this thesis we search for new stable charged particles which couple directly to the Z boson. The Z is produced in the e^+e^- collisions at the SLAC Linear Collider (SLC) and its decay is recorded with the MARK II detector. We limit the number of all possible final states to those in which new particles are produced in pairs with no additional accompanying particles. Thus, the expected signal consists of two charged particles with large and equal masses. The particle masses are determined from momentum (p), ionization energy loss (dE/dx) and time-of-flight (TOF) measurements. These measurements are independent and complementary, with the combination of the three providing the mass assignment. Although the search procedure we have developed is completely general, the results can be interpreted in terms of specific extensions of the Standard Model.

The total energy E of any particle can be written in terms of its momentum p, and its rest mass M, and setting the speed of light $c = 1$ as

$$E^2 = M^2 + p^2. \tag{2.1}$$

In order to fulfill the energy-momentum conservation requirements, the momenta of the product particles must be equal in magnitude but opposite in direction. Under the assumption of mass equality, the energy of each of the particles must also be the same. The total energy of the system in this case is equal to the mass of the Z boson, M_Z, which is shared equally between the two particles in the final state:

$$M_Z = 2\sqrt{p^2 + M^2}. \tag{2.2}$$

This expression can be rearranged as

$$p = \left[\left(\frac{M_Z}{2} \right)^2 - M^2 \right]^{\frac{1}{2}} . \tag{2.3}$$

Since the velocity is given by $v = p/M$, for a given mass M we can predict the expected value of the particles' momentum p and velocity v. These quantities in turn allow us to calculate the expected values of other quantities measurable in the experiment. The knowledge of the velocity, together with the particle trajectories, allows the estimation[2] of the ionization energy loss in the central drift chamber from the Bethe-Block formula[3] and also allows for the computation of the expected time-of-flight of the particles through the chamber.

The mass range accessible for production of new particles is limited by energy-momentum conservation and extends from zero to half the Z mass. Correspondingly, the values of the momentum, dE/dx and TOF for massive particles, as expected to be measured by the MARK II detector, are shown in fig. 2.1 for this range of particle masses. The shaded bands shown in the figure correspond to the $\pm 1\sigma$ variations of these expected measurements due to the resolution of each of the measuring systems (a detailed description of the experimental resolution is given in Chapters 4 and 5). Conversely, the information contained in fig. 2.1 can be used to provide mass assignments to candidates which are compatible with a stable charged particle pair production topology.

The events of interest have three main distinguishing features. These are:

1) There must be two and only two charged tracks found in the detector.

2) The tracks must be back-to-back, i.e., traveling in opposite directions, inside the detector.

3) The tracks must have equal momenta.

Such criteria are fulfilled by the production of known particles as well, i.e., electron and muon pairs. The Z decays to electron pairs are removed from further consid-

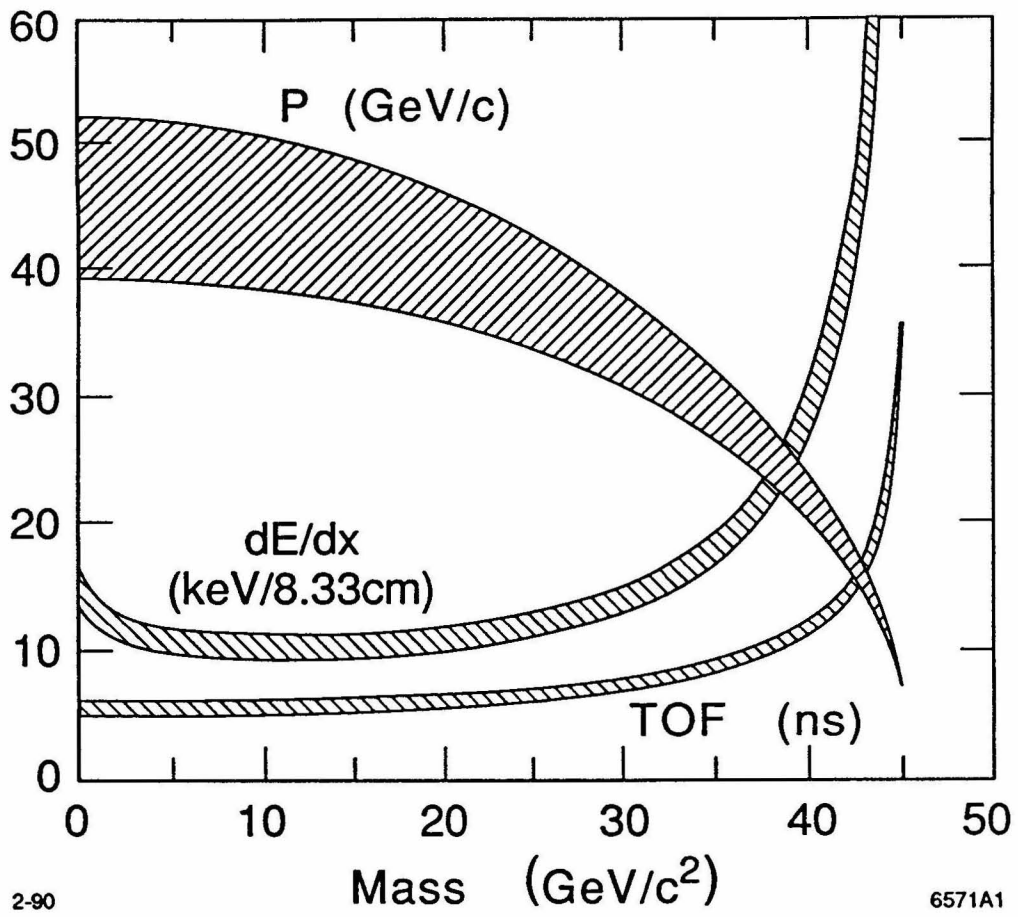

Figure 2.1. The expected values of the momentum, dE/dx, and TOF measurements as a function of particle mass for stable particle-antiparticle pairs produced in Z boson decay. The shaded bands show the $\pm 1\sigma$ variation in the measured quantities.

eration as candidate events by using additional information from the electromagnetic calorimeter in the MARK II. The decays to muon pairs remain in the analyzed sample of the data.

To determine the masses of the particles in candidate events we rely on the maximum likelihood method. The likelihood function is formed from the product of the probability density distributions for the momentum, dE/dx, and TOF of each

track. These distributions are based on the resolutions of each measurement system and centered at the measured value of these quantities for each track in a selected event. A test on the magnitude of the logarithm of the likelihood function is also made to test the validity of the assumption of stable pair production. This test is needed in order to remove background events which survive the selection criteria.

The events selected from the data with the above topology and which have maximum likelihood masses above 2 GeV/c^2 are taken to be the candidates for new stable charged particle production. Such signal is compared with the expected number of events due to various backgrounds which survive the same selection criteria. For masses below 2 GeV/c^2, such signal is indistinguishable from Z decays to muon pairs. We perform an indirect search for new particle production in this region by comparing the number of candidate events to the number expected from Z decays to $\mu^+\mu^-$ pairs alone.

2.2 The Standard Model

The term Standard Model refers to the presently accepted version of the gauge theory of the electromagnetic and weak interactions between elementary particles. The elements of the theory which are relevant to our search are presented in this and the next chapter. Much of the information presented here is extracted from refs. 1 and 4.

The fundamental objects of the theory are spin-$\frac{1}{2}$ particles called *fermions* which interact with each other by coupling to spin-1 particles called *gauge bosons*,* i.e., the gauge bosons *mediate* these interactions. The strengths of the couplings in the theory

---

* The quantum number describing a particle's intrinsic angular momentum is referred to as *spin*. Particles with half integral values of spin called fermions obey Fermi statistics. Particles with integral values of spin called bosons obey Bose-Einstein statistics. The gauge bosons are sometimes referred to as *intermediate vector bosons* since the operators which describe the interactions they mediate transform as vectors or axial-vectors under Lorentz transformations.

are given in terms of the arbitrary constants α and G_F and $\sin^2\theta_W$ which must be determined by experiment.

The framework of the Standard Model can also be extended to include quantum chromodynamics[5] (QCD) – the theory of the strong interactions. The electromagnetic, weak and strong interactions, together with the commonly known gravitational attraction between particles with mass, constitute the only known forces in nature.

2.2.1 The fundamental fermions

The fundamental fermions are classified as either *quarks* or *leptons*. This classification is based on whether or not they participate in the strong interactions. The quarks and leptons are point particles in the theory. This is in agreement with experiment where they appear to be structureless at the level of 1×10^{-16} cm, which is the current limit of resolution.

The quarks and leptons can be further classified by their electric charge. There are three leptons with unit* charges: the electron (e), the muon (μ), and the tau (τ). Each of these has its own conserved leptonic quantum number. A compilation of experimental measurements by the Particle Data Group[6] gives the following values for their masses: for the electron $M_e = 0.51099906 \pm 0.00000015$ MeV/c^2, for the muon $M_\mu = 105.65839 \pm 0.00006$ MeV/c^2 and for the tau $M_\tau = 1784.1^{+2.7}_{-3.6}$ MeV/c^2. There are also three distinct neutral leptons called neutrinos carrying distinct electron, muon and tau quantum numbers: ν_e, ν_μ and ν_τ. The masses of the neutrinos are assumed to be zero in the Standard Model. Experimentally, the neutrino masses have not been determined and are limited[6] at present to be $M_{\nu_e} < 18\text{eV}/c^2$, $M_{\nu_\mu} < 0.25$ MeV/c^2 and $M_{\nu_\tau} < 35$ MeV/c^2. In almost all extensions of the Standard Model additional symmetries allow neutrinos to be massive, although their masses may be arbitrarily small. In the Standard Model the quark charges differ from unity. The up (u), charm

* Here one unit of electric charge is equal to 1.6×10^{-19} Coulomb. There are two polarities of electric charge denoted + for positive and − for negative. The charged leptons have one unit of negative charge.

(c), and top (t) quarks have charge 2/3 and the down (d), strange (s), and bottom (b) quarks have charge -1/3. The name or type of a quark is also referred to as its *flavor.*

A summary of the fundamental fermions is presented in Table 2.1. All of the particles listed* in the table have been observed in experiment with the exception of the top quark and tau neutrino, although there is mounting indirect evidence of their existence. These two particles are needed to complete the family grouping of the Standard Model.

Table 2.1. Table of the fundamental fermions.

Family	Charged Leptons	Neutral Leptons	Charge -1/3 Quarks	Charge 2/3 Quarks
I	e	ν_e	d	u
II	μ	ν_μ	s	c
III	τ	ν_τ	b	t

The fundamental fermions are grouped into *families* (also referred to as *generations*) in the Standard Model. This grouping is indicated in Table 2.1. Its significance not completely understood. It arises from several empirical observations, the simplest being the ascending masses of the charged leptons and quarks in each successive generation. Other evidence supporting this grouping is the representation of the quarks and leptons of each family as weak isospin doublets in the Standard Model and the observed conservation of the lepton quantum numbers in all electromagnetic and weak interactions. The family grouping is also a natural property of many theories which attempt to unify the known forces of nature.

* It should be noted that there also exists an anti-particle with opposite electric charge for each of the fermions listed in Table 2.1. The particle/anti-particle states are usually denoted as $f/\bar{f}$, where f stands for one of the fermions in the table. In the case of the charged leptons however, the states are also commonly referred to as e^-/e^+ , μ^-/μ^+ and τ^-/τ^+.

2.2.2 The strong interaction

The theory describing the strong interactions between particles is called Quantum Chromodynamics.[5] In this theory the interactions between quarks are described by the forces acting upon a strong charge called *color*. Each quark has one of the three color charges: red, green or blue. There are also three anticharges for the antiquarks: antired, antigreen and antiblue. The charges are additive quantum numbers with the following properties: the combination of a color and anticolor charge is color neutral and the combination of three different color charges is also color neutral.

The particles which mediate the strong interaction between quarks are called *gluons*. Gluons are massless, have zero electric charge, and carry two different color charges each such that color is conserved in all quark-gluon-quark interactions. For example, a blue quark can turn into a red quark by emitting a blue-antired gluon. Gluons can interact only with particles which have a color charge: quarks and other gluons.

The nature of the strong interaction is such that experimentally observed particles are color neutral. This means that individual quarks do not exist alone, but are bound by gluons in color neutral combinations. These combinations are either in the form of oppositely colored quark-antiquark pairs (called *mesons*) or as three quarks each with a different color (called *baryons*). The quarks in any given combination can have the same or mixed flavors; what is important is that the color charges combine to be color neutral. Mesons and baryons are specific classes of *hadrons*, i.e., particles which participate in the strong interaction. Some examples of observed hadrons are listed in Table 2.2 and a complete and current listing can be found in ref. 6.

Since the quarks can not be observed as free particles in experiment, their masses must be estimated from the masses of hadrons which they form and the knowledge of the strong force which binds them via gluons.[7] These estimates are $M_u \simeq 0.005$ GeV/c^2, $M_d \simeq 0.008$ GeV/c^2, $M_s \simeq 175$ GeV/c^2, $M_c \simeq 1270$ GeV/c^2, $M_b \simeq 4250$ GeV/c^2. The lower experimental limit on the top quark mass is 77 GeV/c^2.[8]

Table 2.2. Examples of hadrons.

Name	Type	Quarks	Mass
Proton p	Baryon	uud	938.27231 ± 0.00028 MeV/c^2
Neutron n	Baryon	udd	939.56563 ± 0.00028 MeV/c^2
Kaon K^+	Meson	$u\bar{s}$	493.646 ± 0.009 MeV/c^2
J/Ψ	Meson	$c\bar{c}$	3096.9 ± 0.1 MeV/c^2
B^-	Meson	$\bar{u}b$	5277.6 ± 1.4 MeV/c^2

2.2.3 *The gauge theory of the electroweak interactions*

The gauge theory of the electroweak interactions unifies the electromagnetic interaction described by Quantum Electrodynamics[9] (QED) with the Fermi theory of the weak interactions. This unification preserves the properties of both theories.

The Lagrangian function of QED is unchanged under a *local gauge transformation* of the electron field $\psi(x)$ and the photon field $A_\mu(x)$ at all space-time points x:

$$\begin{aligned} \psi(x) &\rightarrow \exp[ie\Lambda(x)]\psi(x), \\ \mu(x) &\rightarrow A_\mu(x) + \partial\Lambda(x)/\partial x_\mu, \end{aligned} \tag{2.4}$$

where e is the electron-photon coupling and $\Lambda(x)$ is an arbitrary function. In other words, we can alter $\psi(x)$ by an arbitrary phase factor, provided that we simultaneously adjust $A_\mu(x)$ in a suitable way. The photon field plays an intrinsic part; there could be no gauge invariance without it. Hence, if we take the postulate of this local gauge invariance for spin-$\frac{1}{2}$ particles as a starting point, the existence of gauge bosons (in this case photons) is required and in fact their coupling to electric charge is specified, too. For exact gauge invariance, the gauge bosons must be massless.

The product of the phase factors $\exp[ie\Lambda(x)]$ generate the symmetry group U(1) of unitary transformations in one dimension. The generalization of QED to other forces is made by looking for other possible symmetry groups and using them as the basis of more general gauge transformations. For example, we may choose to regard

the electron and electron neutrino as a doublet (ν_e, e), i.e., as two members of the same family since both are light spin-$\frac{1}{2}$ particles. We can then describe this doublet by a two-component field $\psi = (\psi_\nu, \psi_e)$ and introduce gauge transformations where the generator of these transformations, Λ, is a 2×2 hermitian matrix operating on ψ. We can put the other leptons and the quarks, too, into doublets $(\nu_\mu, \mu), (\nu_\tau, \tau), (u, d)$, *etc.*, and subject them to similar gauge transformations. These transformations are much more than phase factors, since the off-diagonal elements of Λ can change one member of a doublet into the other. These transformations belong to the symmetry group SU(2) of unitary unimodular transformations in two dimensions.

The Glashow-Salam-Weinberg[10] theory of the electroweak interactions is a SU(2) $\times$U(1) gauge theory which unifies the electromagnetic and weak interactions. The generators of the SU(2) symmetry are given by the matrices $\tau/2$ where the τ are the weak isospin Pauli matrices:

$$\tau_1 = \begin{pmatrix} 0 & 1 \\ 1 & 0 \end{pmatrix}, \quad \tau_2 = \begin{pmatrix} 0 & -i \\ i & 0 \end{pmatrix}, \quad \tau_3 = \begin{pmatrix} 1 & 0 \\ 0 & 1 \end{pmatrix}. \tag{2.5}$$

These matrices have the property that the operator $T^{\pm} = \frac{1}{2}(\tau_1 \pm i\tau_2)$ raises or lowers the *weak isospin* quantum numbers of a particle by one unit and the operator $T_3 = \frac{1}{2}\tau_3$ projects out the third component of weak isospin. Local gauge invariance in this case requires the introduction of three massless spin-1 gauge bosons W^+, W^0, W^- which couple to the weak isospin of the fermions. The superscript on the gauge bosons refers to their electric charge. The generator of the U(1) symmetry is the weak hypercharge quantum number given by

$$Y = 2(Q - T_3), \tag{2.6}$$

where Q is the electric charge and T_3 is the third component of the weak isospin of the particle. Local gauge invariance introduces one more gauge boson, B^0, which couples to the weak hypercharge. These two symmetries are combined in the theory and the product of transformations generated by T and Y form the gauge group SU(2)$\times$U(1).

The SU(2)×U(1) symmetry of the Glashhow-Salam-Weinberg theory is broken and, therefore, not all of the electroweak gauge bosons are massless. As a result of the symmetry breaking, the physical neutral gauge bosons γ and Z are mixed as linear combinations of the neutral gauge bosons of the unbroken theory:

$$\gamma = B^0 \cos\theta_W + W^0 \sin\theta_W, \tag{2.7}$$

and

$$Z = B^0 \sin\theta_W - W^0 \cos\theta_W, \tag{2.8}$$

where the mixing or Weinberg angle θ_W is a arbitrary parameter of the theory. As a result of the symmetry breaking and mixing, the gauge bosons acquire masses. The relation between the masses of the gauge bosons and the coupling constants is given by

$$\begin{aligned} M_W &= (\frac{\pi\alpha}{\sqrt{2}G_F})^{\frac{1}{2}} \frac{1}{\sin\theta_W}, \\ M_Z &= \frac{M_W}{\cos\theta_W} = (\frac{\pi\alpha}{\sqrt{2}G_F})^{\frac{1}{2}} \frac{1}{\sin\theta_W \cos\theta_W}, \\ M_\gamma &= 0, \end{aligned} \tag{2.9}$$

where α is the fine structure constant and G_F is the Fermi constant, also called the weak coupling constant. The values of these constants are measured[6,11] to be

$$\begin{aligned} \alpha &= 1/137.0359895(61), \\ G_F &= (1.16632 \pm 0.00004) \times 10^{-5}\mathrm{GeV}^{-2}. \end{aligned} \tag{2.10}$$

2.2.3.1 The Higgs boson and the Higgs mechanism

In the simplest or minimal version of the Standard Model, an additional field is needed to give rise to the SU(2)×U(1) symmetry breaking and the observed masses of the W and Z bosons and the fundamental fermions. This is accomplished in the theory by introducing into the Lagrangian an SU(2) doublet consisting of four real

fields. Three of these fields are absorbed by the W^+, W^- and the Z which become massive as a result. The remaining Higgs field which was not absorbed by a gauge boson should exist as a particle.

In order for this *Higgs mechanism* described above to work, the vacuum expectation value of the Higgs doublet must be chosen to be non-zero. This has the consequence that the vacuum state is not invariant under group transformations generated by the weak isospin and the weak hypercharge. In this case, the symmetry of the SU(2)×U(1) group is said to be broken. The Higgs mechanism is an example of the general phenomenon of *spontaneous symmetry breaking* in which the ground state of a physical system, in this case the vacuum, has less symmetry than the Lagrangian.

The experimental detection of the Higgs boson would lend a firmer phenomenological basis to the Higgs mechanism. The experimental search is complicated by the fact that the Higgs particle mass is not given by the Standard Model. Several experiments designed to detect Higgs particle production in colliding beam experiments have failed to find any evidence for its existence. The experimental lower limit[12] on the mass of the Higgs boson is currently 41.6 GeV/c^2. The Higgs particle search is one of the major justifications for the construction of the Superconducting Super Collider.[13] The Higgs should be discovered at the SSC even if its mass is as high as 800 GeV/c^2.

2.2.4 *Lepton states*

The electroweak theory is said to be chiral in nature because its interactions distinguish between the handedness of particles.* The left-handed lepton states of each family form weak isospin doublets and the right-handed states form weak isospin singlets

$$\begin{pmatrix}\nu_e\\ e\end{pmatrix}_L \quad (e)_R, \quad \begin{pmatrix}\nu_\mu\\ \mu\end{pmatrix}_L \quad (\mu)_R, \quad \begin{pmatrix}\nu_\tau\\ \tau\end{pmatrix}_L \quad (\tau)_R. \tag{2.11}$$

* A right-handed particle state has its spin aligned with its direction of motion and a left-handed particle state has its spin aligned against the direction of motion.

Here the left-handed states of a charged lepton l and neutrino ν of the same family are given in terms of the spin projection operator $(1-\gamma_5)$ as

$$\begin{aligned} \nu_L &= \frac{1}{2}(1-\gamma_5)\nu, \\ l_L &= \frac{1}{2}(1-\gamma_5)l. \end{aligned} \tag{2.12}$$

The third component of weak isospin T_3 is equal to $+1/2$ for the left-handed neutrino states and equal to -1/2 for the left-handed charged lepton states. The right-handed charged lepton states are given by

$$l_R = \frac{1}{2}(1+\gamma_5)l, \tag{2.13}$$

and have weak isospin $T_3 = 0$. In the Standard Model, the right-handed neutrino states

$$\nu_R = \frac{1}{2}(1+\gamma_5)\nu = 0, \tag{2.14}$$

do not exist. The requirement that the electric charge of the states is given by $Q = T_3 + \frac{1}{2}Y$ leads to the weak hypercharge assignments $Y_L = -1$ for left-handed states and $Y_R = -2$ for right-handed states.

2.2.5 *Lepton-gauge boson interactions*

The leptons interact with the electroweak gauge bosons as shown in fig. 2.2. The corresponding Feynman rules for these interactions are given as follows:

(a) For the electromagnetic interaction shown in fig. 2.2(a), the Feynman rules give for the coupling:

$$-iQ_f \bar{f} \gamma_\lambda f, \tag{2.15}$$

where Q_f is the charge of the lepton and γ_λ is an operator which represents the interaction between the lepton wave function spinors f and $\bar{f}$* and λ is a spinor index. This coupling is zero for neutrinos since Q_ν=0.

* Since we will later generalize these couplings to quarks we use the symbol f for fermion.

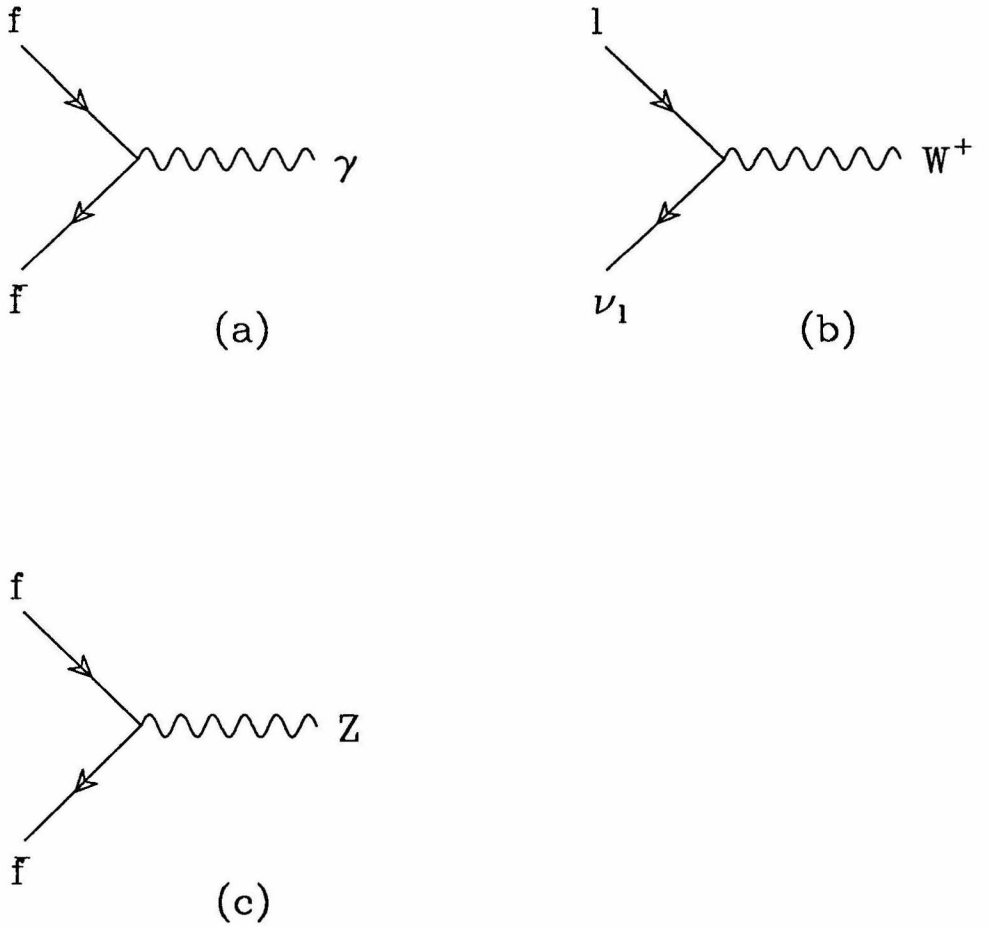

Figure 2.2. Feynman diagrams for the fermion-gauge boson interactions of the Standard Model: (a) The coupling of a fermion anti-fermion pair to the photon, (b) the coupling of a charged and neutral lepton to the W boson, (c) the coupling of a fermion anti-fermion pair to the Z boson.

(b) The Feynman rules for the interaction of a lepton doublet with the W, shown in fig. 2.2 (b), give for the coupling

$$-i\left(\frac{G_F M_W^2}{\sqrt{2}}\right)^{\frac{1}{2}} \bar{\nu}\gamma_\lambda(1-\gamma_5)l. \tag{2.16}$$

This is sometimes referred to as the *charged current* interaction because one unit of electric charge is exchanged between the leptons through the coupling. Only

leptons from the same family can couple in this way. For example a τ can only couple to a ν_τ and not a ν_μ or ν_e.

Here, the operator representing the transition from a lepton state l to the neutrino ν is given by $\gamma_\lambda(1-\gamma_5)$, where the factor $(1-\gamma_5)$ is present to project out the left-handed neutrino state. In order to display the vector (V) − axial-vector (A) nature of this interaction, one may rewrite this as $\gamma_\lambda - \gamma_\lambda\gamma_5$. Here, the operator γ_λ behaves like a vector under Lorentz transformations and, while $\gamma_\lambda\gamma_5$ also behaves like a vector under rotations, it changes sign under spatial inversions and thus has axial-vector symmetry. A consequence of the (V−A) nature of the weak charged current interactions is that they violate the law of parity conservation that requires an interaction and its spatial inversion to be identical.

(c) The coupling of leptons to the Z , shown in fig. 2.2(c), is also called the *neutral current* interaction since no charge is exchanged between the leptons. The Feynman rules for this interaction give for the coupling

$$\frac{-i}{\sqrt{2}}\left(\frac{G_F M_Z^2}{\sqrt{2}}\right)^{\frac{1}{2}} \bar{f}\gamma_\lambda[R_f(1+\gamma_5)+L_f(1-\gamma_5)]f. \tag{2.17}$$

Here both the left- and right-handed states of the charged leptons take part in the interaction with their relative strengths given by

$$\begin{aligned} L_f &= 2T_3 - 2Q_f \sin^2\theta_W, \\ R_f &= -2Q_f \sin^2\theta_W, \end{aligned} \tag{2.18}$$

where $T_3 = 0$ for right-handed states. For the neutrinos, which are always left-handed and electrically neutral, the coupling reduces to

$$\frac{-i}{\sqrt{2}}\left(\frac{G_F M_Z^2}{\sqrt{2}}\right)^{\frac{1}{2}} \bar{\nu}\gamma_\lambda(1-\gamma_5)\nu. \tag{2.19}$$

2.2.6 *Quark states and mixing*

In the Standard Model, a similar approach to that used for the leptons is taken

to describe the electroweak interactions of quarks. In this case, however, the weak quark states which couple to the W boson are not the same as the quark mass states described before. In the weak interactions, the quark family symmetry is seen to be broken so that the quark mass states with the same electric charge (the d, s and b states or the u, c and t states) can mix. The weak isospin doublets which couple to the $W^{\pm}$ are given by

$$\begin{pmatrix} u \\ d' \end{pmatrix}, \quad \begin{pmatrix} c \\ s' \end{pmatrix}, \quad \begin{pmatrix} t \\ b' \end{pmatrix}, \tag{2.20}$$

where a 3×3 unitary matrix known as the Kobayashi-Maskawa (K-M) matrix rotates the mass eigenstates d, s and b into the weak doublet states d', s' and b'

$$\begin{pmatrix} d' \\ s' \\ b' \end{pmatrix} = \begin{pmatrix} V_{ud} & V_{us} & V_{ub} \\ V_{cd} & V_{cs} & V_{cb} \\ V_{td} & V_{ts} & V_{tb} \end{pmatrix} \begin{pmatrix} d \\ s \\ b \end{pmatrix}. \tag{2.21}$$

The values of the individual matrix elements are not specified in the Standard Model and must be determined from experimental measurements of the weak decays of the corresponding quarks.

It has been noticed by Wolfenstein[14] that the following parameterization of the K-M matrix approximates the experimental values of the matrix elements

$$\begin{pmatrix} V_{ud} & V_{us} & V_{ub} \\ V_{cd} & V_{cs} & V_{cb} \\ V_{td} & V_{ts} & V_{tb} \end{pmatrix} \simeq \begin{pmatrix} 1 & \lambda & \lambda^3 \\ -\lambda & 1 & \lambda^2 \\ -\lambda^3 & -\lambda^2 & 1 \end{pmatrix}, \tag{2.22}$$

where $\lambda \simeq \sin\theta_c \simeq 0.23$ is given in terms of the Cabibbo[15] angle θ_c which describes the mixing between the first two families only.

2.2.7 *Lepton decays*

The process of lepton decay is described in the Standard Model as shown diagrammatically in fig. 2.3 for the decay of the muon to an electron, $\mu \longrightarrow \nu_\mu e \bar{\nu}_e$. Similar

diagrams describe the decay of the τ lepton, in which case the W can couple to either of the lighter lepton doublets and also to the lightest quark doublet (actually the lightest 3 quark doublets, one for each color) in the final state. The matrix element $\mathcal{M}$ for the muon decay process is given by the product of the couplings at each of the lepton-W vertices (eqn. 2.16) plus a propagator term $1/M_W^2$ to account for the mass of the mediating W boson

$$\mathcal{M} = \frac{G_F M_W^2}{\sqrt{2}} \bar{u}(\nu_\mu)\gamma_\lambda(1-\gamma_5)v(\mu)\frac{1}{M_W^2}\bar{u}(e)\gamma^\lambda(1-\gamma_5)v(\bar{\nu}_e). \tag{2.23}$$

The decay rate is given by

$$d\Gamma = \frac{1}{2M_\mu(2\pi)^5}\sum|\mathcal{M}|^2\delta^4\left(p_\mu - p_{\nu_\mu} - p_e - p_{\bar{\nu}_e}\right)\frac{d^3p_{\nu_\mu}}{2E_{\nu_\mu}}\frac{d^3p_e}{2E_e}\frac{d^3p_{\bar{\nu}_e}}{2E_{\bar{\nu}_e}}, \tag{2.24}$$

where p_i and E_i are the momenta and energies of the final state particles $i = \nu_\mu,\ e,\ \bar{\nu}_e$. After integration, this expression is reduced to

$$\Gamma = \frac{G_F^2 M_\mu^5}{192\pi^3}[1 - 8y + 8y^3 - y^4 - 12y^2\ln y], \tag{2.25}$$

where $y = (M_e^2/M_\mu^2)$. If the expression $\hbar/t_\mu$ where $\hbar = 1$ is the Planck constant and t_μ is the muon lifetime is substituted for Γ in eqn. 2.25, we obtain the weak coupling constant G_F in terms of the muon and electron masses and the muon lifetime as

$$G_F^{-2} = \frac{t_\mu M_\mu^5}{192\pi^3}[1 - 8y + 8y^3 - y^4 - 12y^2\ln y]. \tag{2.26}$$

The value

$$G_F = (1.16632 \pm 0.00004) \times 10^{-5}\text{GeV}^{-2}, \tag{2.27}$$

is obtained from the electron and muon mass values listed above combined with the value[6] for the muon lifetime of $t_\mu = (2.19703 \pm 0.00004) \times 10^{-6}$ sec., and using a

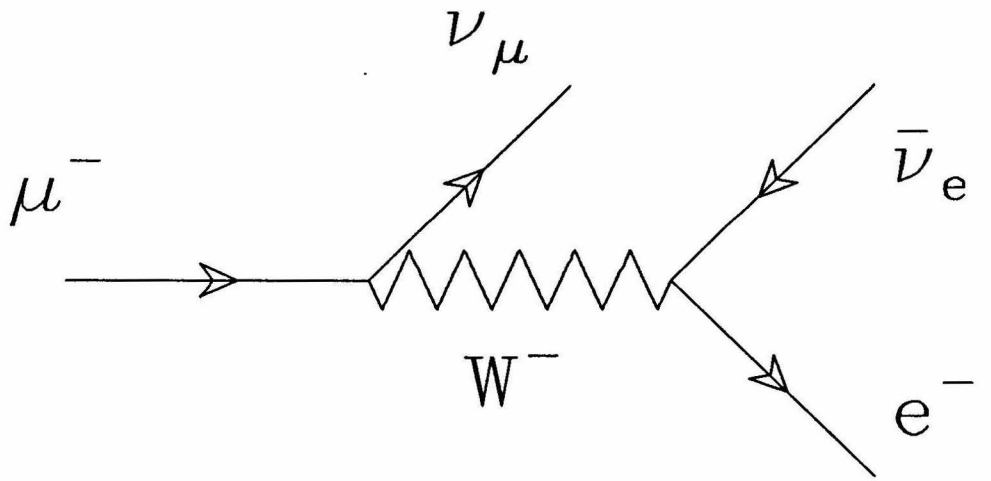

Figure 2.3. Diagram for the charged current lepton decay $\mu^- \rightarrow \nu_\mu e^- \bar{\nu}_e$.

form of eqn. 2.26 that includes an extra term to account for higher order radiative corrections.[11]

The electroweak theory assumes *lepton universality* so that the value of the weak coupling constant G_F determined from muon decay also applies to the analogous tau lepton decay $\tau \rightarrow \nu_\tau e \bar{\nu}_e$. Under this assumption the partial decay widths are related

$$\Gamma(\tau \rightarrow e\nu_\tau\bar{\nu}_e) = \Gamma(\mu \rightarrow e\nu_\mu\bar{\nu}_e)(m_\tau/m_\mu)^5, \tag{2.28}$$

or, in terms of the tau and muon lifetimes

$$t_\tau = t_\mu(m_\tau/m_\mu)^5 \mathrm{Br}(\tau \rightarrow e\nu_\tau\bar{\nu}_e), \tag{2.29}$$

in which the terms of order y or greater in eqn. 2.25 have been dropped. Using the decay branching ratio for tau decay to electron of $Br(\tau \rightarrow e\nu_\tau\bar{\nu}_e) = 17.4 \pm 0.4\%$[16] and the values for the tau and muon masses listed above, we predict the lifetime $t_\tau = (2.80 \pm 0.06) \times 10^{-13}$sec. This number is compatible with the measured lifetime

of $t_\tau = (3.04 \pm 0.09) \times 10^{-13}$ sec within two standard deviations. Thus, the assumption of lepton universality is consistent with experiment.

2.2.7.1 *Lepton number conservation*

No mixing between lepton families, like that discussed above for the quarks, has been observed in lepton decays.[17] This fact is built into the Standard Model through the conservation of an additive lepton family number as assigned in Table 2.3. In any decay process, the empirical conservation law states that

$$\begin{aligned} \Sigma L_e &= \text{constant}, \\ \Sigma L_\mu &= \text{constant}, \\ \Sigma L_\tau &= \text{constant}. \end{aligned} \tag{2.30}$$

Table 2.3– Lepton number assignments.

Family	Lepton	Lepton Number
I	e^-, ν_e	$L_e = +1$
	$e^+, \bar{\nu}_e$	$L_e = -1$
II	μ^-, ν_μ	$L_\mu = +1$
	$\mu^+, \bar{\nu}_\mu$	$L_\mu = -1$
III	τ^-, ν_τ	$L_\tau = +1$
	$\tau^+, \bar{\nu}_\tau$	$L_\tau = -1$

2.2.8 *Quark decays*

The quarks, like the charged leptons, also decay via coupling to the charged current. The process is called *semileptonic decay* if the mediating $W^\pm$ couples to a lepton doublet in the final state.

2.3 The Family Problem and the fourth generation

The origin of masses of the fundamental particles is one of the most puzzling problems in particle physics today. It is also a question to which the Standard Model offers an incomplete answer. In the Standard Model, particles such as the electron acquire a mass term in the Lagrangian via the Higgs mechanism. This mass term arises due to the interaction of the electron with the non-zero vacuum expectation value of the Higgs field. The problem with the Higgs mechanism, however, is that it does not specify the actual measurable value of the electron mass. Likewise, the masses of the other quarks and leptons are unspecified. These masses must be treated as input parameters to the theory. Therefore, the Higgs mechanism does not provide a fundamental understanding of the origin of the quark and lepton mass values.

An issue possibly related to that of the origin of particle mass is the so-called *Family Problem.* The fundamental fermions that have been observed so far in experiment form the three families in the Standard Model as listed in Table 2.1. The fact that only three generations are currently observed is not specified in any way by the theory. Indeed, there is an indication from QCD corrections[18] that the number of quark families should be smaller than 33/2, i.e., not a very restrictive number. An important question, then, is whether a fourth or higher generation of quarks and leptons exists.

2.3.1 Methods to search for the fourth generation

There are several ways in which evidence for a fourth generation can be uncovered. An obvious one is the direct observation in accelerator experiments of new particles whose existence could only be explained in terms of a new family in the Standard Model. These searches are sensitive to the assumptions of the mass range of such new particles and depend on the mass hierarchy within the assumed new generation. Evidence for a fourth generation can also be obtained from a precision measurement of the width of the Z boson resonance. Here, the total width of the Z

depends on the number of particle species into which it can decay. A fourth generation fermion with a mass smaller than one-half the mass of the Z could be produced in Z decay. As a result, the measured value of the total width of the Z would be larger than expected for three families only.

The Standard Model gives no prediction as to the mass hierarchy among the quarks and leptons of a possible fourth generation. The simplest assumption is that the hierarchy is analogous to that of the first three families and, therefore, that the fourth generation neutrino is the lightest member. If the fourth generation neutrino mass were smaller than half the Z boson mass then it would be produced in pairs in Z decay and thus affect the measured width of the Z. One expects a 7% increase of the width of the Z for each additional generation of massless neutrinos. An increase in the Z width would also be expected if any of the masses of the top quark, the fourth generation charge -1/3 bottom type quark (b') or fourth generation charged lepton are below $M_Z/2$. Precision measurements of the Z width can, in principle, discriminate between the various particle production possibilities due to the different coupling strengths given by eqn. 2.18.

A unique type of search can also be designed for the case in which the fourth generation neutrino is more massive than the charged lepton, in which case the charged lepton will be stable. If the mass of the charged lepton is less than half the Z boson mass, it will be produced in Z decay as a particle-antiparticle pair. This thesis addresses such a possibility.

Over the past twenty years, many searches have been conducted at different accelerators. None of them have found any evidence for the existence of a fourth generation of quarks and leptons. The results of these searches limit the possible mass ranges of the fourth generation particles. These limits have been recently updated in several experiments at SLAC and CERN and Fermilab. We will now discuss the results from these experiments.

2.3.2 Results of searches for the fourth generation

The width of the Z has recently been measured[19] using the MARK II detector at the Stanford Linear Accelerator Center (SLAC) Linear Collider (SLC). The experiment measured the cross-section for resonant formation of the Z boson in e^+e^- collisions over a center-of-mass energy ($E_{\rm cm}$) range from 89.2 to 93.0 GeV. The measured cross-section is plotted in fig. 2.4. The width of the resonance was extracted from the data and compared to that expected in the three family Standard Model. The sensitivity of the measurement was such that the size of the measured width excludes the existence of a massless fourth generation neutrino at the 95% confidence level. The same experiment has been repeated by the ALEPH,[20] DELPHI,[21] L3,[22] and OPAL[23] detector collaborations working at the Large Electron-Positron collider (LEP) at CERN. The experimental results from CERN are all in agreement with the MARK II result. The combination[24] of the recent measurements from all the groups gives the number of massless neutrinos in the Standard Model as 2.95 ± 0.11. This eliminates the possibility of the existence of a massless fourth generation neutrino beyond all reasonable doubt. The combination of the measurements has also been used to set[24] a 95% confidence level lower limit of 44 GeV/c^2 on the mass of a possible heavy stable fourth generation neutrino.

Another possibility is that the fourth generation neutrino is massive and unstable. Here the weak eigenstates of the neutrinos $\nu_l (l = e, \mu, \tau, l_4)$ are mixtures of the mass eigenstates $\nu_i (i = 1, 2, 3, 4 = \text{generation number})$

$$\nu_l = \sum_{i=1}^{4} U_{li} \nu_i, \tag{2.31}$$

where U_{li} is a unitary mixing matrix. This mixing allows the ν_4 to couple to the lighter charged leptons through the weak charged current $\nu_4 \rightarrow l^- W^+ (l^- = e^-, \mu^-, \tau^-)$ with (V−A) coupling at the W vertex. A simple analogy with the mixing structure of the quark sector would indicate that the ν_4 would couple most strongly to the third

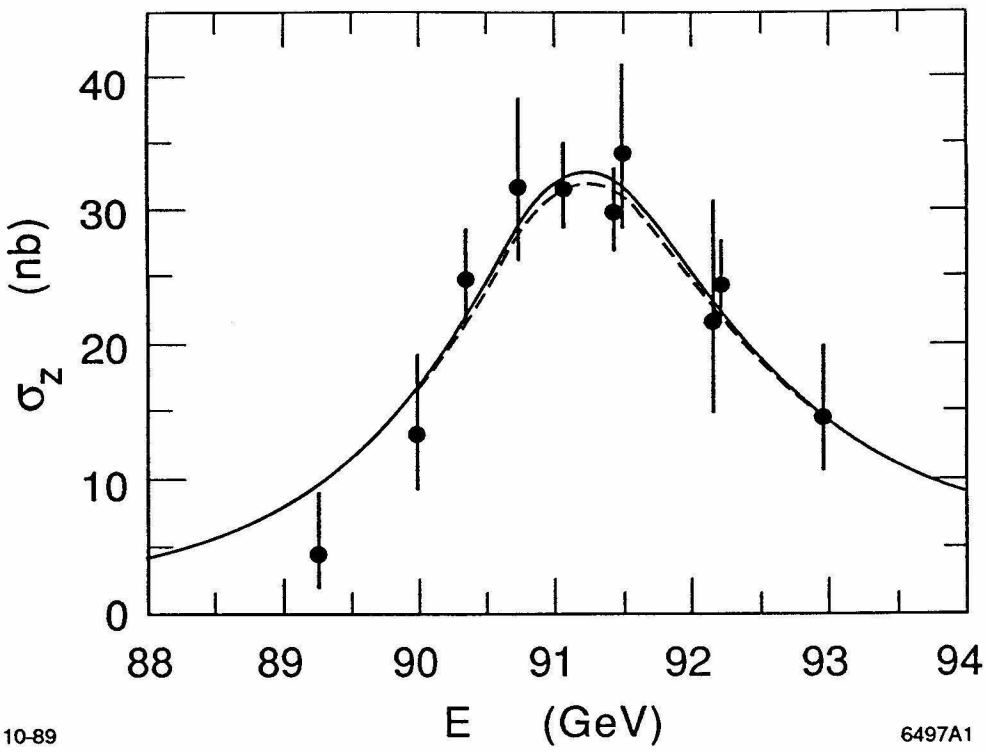

Figure 2.4. The Z boson production cross-section in e^+e^- annihilations as a function of center-of-mass energy. The data are shown as points with error bars. The solid and dotted lines represent the results of alternate fitting procedures used to extract the width of the resonance.

generation charged lepton, the $\tau^{\pm}$. If we assume that the ν_4 couples exclusively to a single generation then its lifetime, t_{ν_4}, can be expressed in terms of the muon lifetime t_μ as

$$t_{\nu 4} = \left[\frac{M_\mu}{M_{\nu_4}}\right]^5 \frac{t_\mu Br(\nu_4 \to l^- e^+ \nu_e)}{|U_{l4}|^2 f}, \tag{2.32}$$

where f is a phase space suppression factor[25] for massive final state particles that differs appreciably from unity when one or more of the final state particles is a τ lepton or charm quark, and the mass M_{ν_4} of the ν_4 is relatively small.

Several searches for massive unstable neutrinos have been conducted at SLC and at LEP. The analyses all differ in the range of ν_4 masses and lifetimes to which they are sensitive. The results of these searches are shown in fig. 2.5. All of these searches

are sensitive to the existence of a new neutral lepton which couples to the charged lepton of any of the first three generations. The combination of the results shown in the figure rule out, at the 95% confidence level, the possible existence of a massive unstable fourth generation neutrino with a mass less than one-half the Z boson mass.

Searches for an unstable fourth generation charged lepton l_4 were also performed at LEP. The search strategy of the ALEPH Collaboration[31] was to look for an excess in the Z decay width to hadrons due to a contamination from l_4 decays. The precision of their measurement allowed them to exclude, at the 95% confidence level, the region of the l_4 mass versus the fourth generation neutrino mass plane shown in fig. 2.6. A direct search for l_4 charged current decays was conducted by the OPAL Collaboration.[32] Their limit on the l_4 mass is also shown in fig. 2.6.

Finally, direct searches for a fourth generation charge -1/3 quark (b') distinct from the top quark were also performed at CERN, SLAC and Fermilab. One expects the top quark to decay via the charged current process $t \rightarrow bW^*$ where the W^* is a virtual-W. Naively, one also expects the b' to decay via the charged current process $b' \rightarrow cW^*$ if the mass of the b' quark is less than the mass of the top quark. Assuming that a new quark decays 100% via the charged current mode, the UA1 Collaboration[33] has excluded top quarks with masses less than 44 GeV/c^2 and b' quarks with masses less than 32 GeV/c^2. With the same assumption, the CDF Collaboration[8] has excluded top quarks with masses between 40 and 77 GeV/c^2.

A b' quark may not decay 100% of the time via the charged current decay because of increased suppression of transitions which cross two generations.[34] Consequently, the flavor changing neutral current loop decays[35] of $b' \rightarrow b + gluon$ and $b' \rightarrow b\gamma$ shown in fig. 2.7 must also be considered. Furthermore, in extensions of the Standard Model with two Higgs doublets, the top and b' quarks can decay into charged Higgs particles ($H^{\pm}$) by $t \rightarrow H^+ b$ or $b' \rightarrow H^- c$ if the mass of the Higgs particle is less than the mass of the decaying quark. This two body decay mode would dominate over the charged current decay mode.

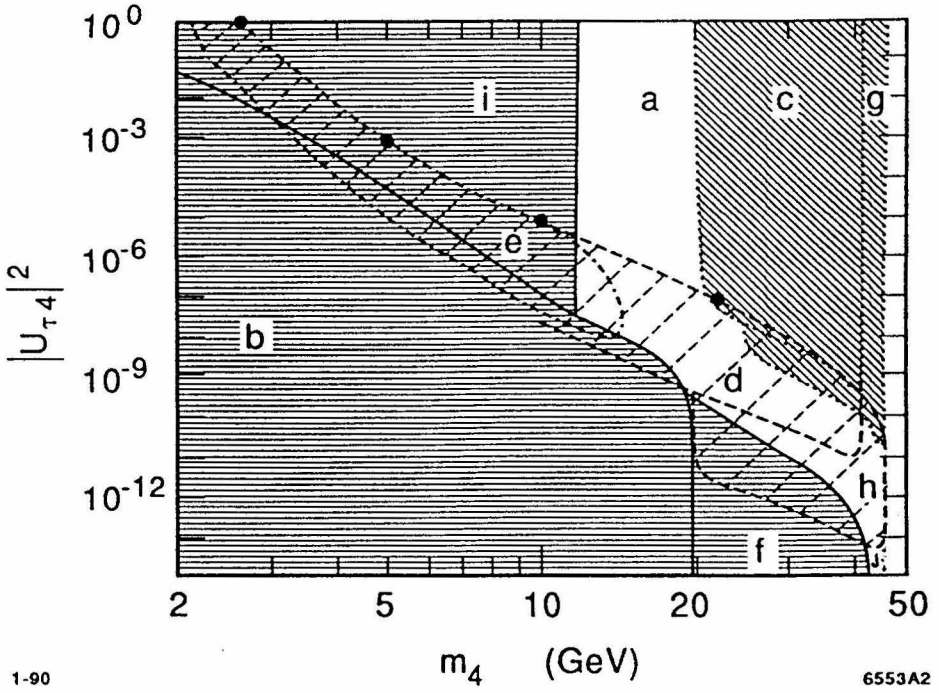

Figure 2.5. Regions in the plane of m_4 versus $|U_{\tau 4}|$ which are excluded at a confidence level of at least 95% for a fourth-generation neutrino by a search at SLC for its decay to two charged lepton tracks[26] (regions *a* and *i* above the solid dots); by the measurement of the decay width of the Z to invisible final states at SLC[19,27] (region *b*); by a search for high-energy, isolated tracks at SLC[28] (region *c*); by a search for events with a large number of high-impact-parameter tracks at SLC[29] (region *d*) and by a search for events with track vertices detached from the interaction point at PEP[30] (region *e*). The additional regions excluded by the ALEPH collaboration at LEP[31], but not previously excluded by Mark II, are shown as regions *f*, *g*, *h*, and *i*. The small remaining region *j* is excluded by a combination of LEP measurements.[24] The shading has the following meaning: horizontal lines indicate regions excluded by measurements of the Z resonance parameters; dashed diagonal lines indicate regions excluded by direct searches for tracks not originating from the collision point; and solid diagonal lines indicate regions excluded by direct searches for events with isolated tracks. The solid dots indicate the cases simulated for study *a* from which the figure was taken (ref. 26).

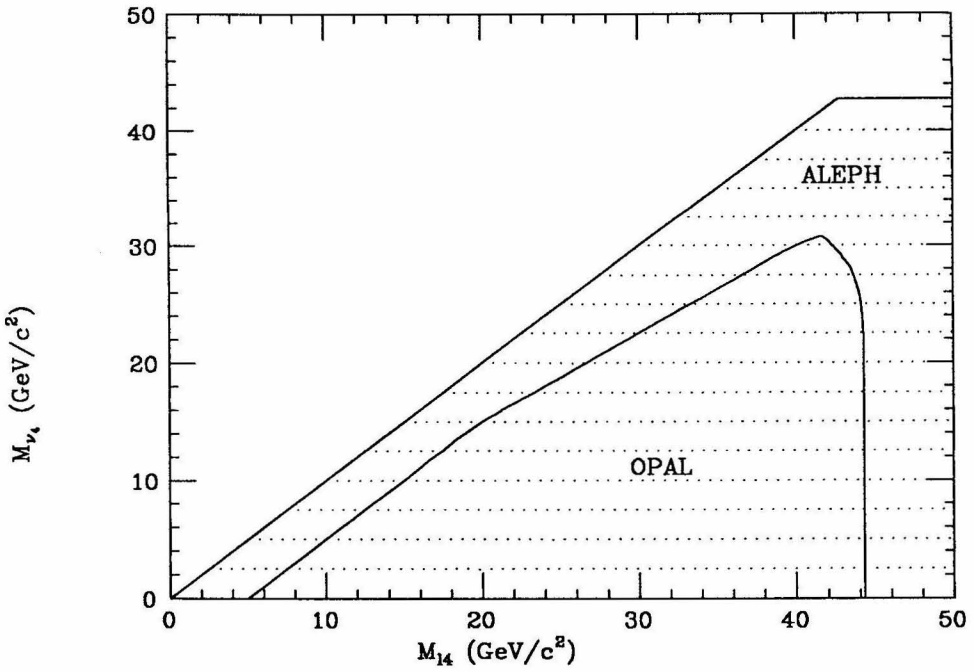

Figure 2.6. Mass limits on unstable fourth generation charged leptons from LEP

The results of searches by the MARK II,[28] ALEPH,[31] OPAL[36] and DELPHI[37] Collaborations for the top and b' quarks that assume they decay through one of channels discussed above are given in Table 2.4. These results basically exclude at the 95% confidence level the possible existence of a top or b' quark up to the kinematic limit of the experiments.

2.3.3 *Fourth generation stable charged leptons*

The above searches for fourth generation quarks and leptons do not address the scenario in which the fourth generation neutrino is more massive than the charged lepton. In this case, the Standard Model decay of the fourth generation charged lepton into a fourth generation neutrino through a coupling to the W boson is kinematically forbidden. Furthermore, the lepton number conservation of the Standard Model implies that such a fourth generation charged lepton would be stable. If the

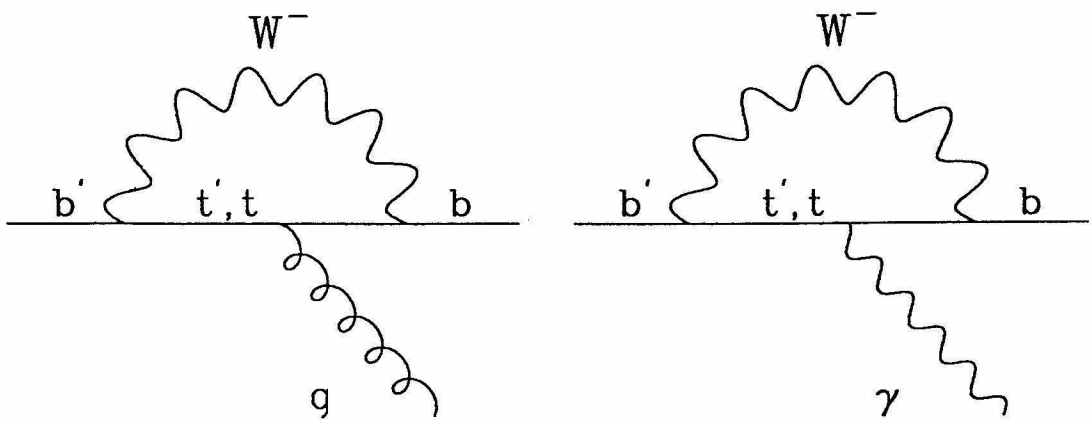

Figure 2.7. Flavor changing neutral current loop decays of the b' quark

Table 2.4. A summary of results from LEP and SLC of searches for the top and fourth generation charge -1/3 quark (b'). The 95% confidence level lower mass limits are given in GeV/c^2 assuming each of the possible decay modes discussed in the text.

Decay Mode	MARKII	ALEPH	OPAL	DELPHI
$t \to bW^*$	40.7	45.8	45.1	44.5
$b' \to cW^*$	44.7	46.2	45.4	45.0
$b' \to bg$	42.7	45.8	45.4	
$b' \to b\gamma$	45.4	45.8	46.2	
$t \to bH^+$	42.5	45.3	45.3	44.0
$b' \to cH^-$	45.2	45.4	45.5	44.5

mass of the charged lepton is less than half the Z boson mass it will be produced in Z decay as a particle-antiparticle pair and thus be a candidate for the new stable charged particle search presented in this thesis.

2.4 Extensions of the Standard Model

There are numerous theories which go beyond the framework of the Standard Model in an attempt to unify all known interactions between elementary particles. Many of them predict the existence of new particles in addition to those already well described by the Standard Model. In these theories, there are usually some restrictions preventing the rapid decay of such new particles into those experimentally observed so far. Therefore, the lightest of such new particles is expected to be stable. We discuss here two specific classes of theories in which the lightest of the new particles could be stable and charged, and for which the coupling to the Z boson is specified.

2.4.1 *Left-right symmetric theories*

A unique empirical aspect of the weak interactions is the non-conservation of parity. This fact is accommodated in the Standard Model by the (V−A) structure of the weak charged current interactions. In this theory it is assumed that the left-handed fermion states transform as doublets and that they couple to the $W^{\pm}$ boson while the right-handed states transform as singlets and do not couple to the charged current. This construction, however, provides no fundamental explanation as to why this chiral structure of the weak interaction given by the (V−A) current exists. This leaves open the question of whether the Standard Model is a special case of a more general theory containing a second class of fermions which couple to the W boson with (V+A) couplings. Such particles would have interactions that are mirror images of those of the known quarks and leptons. This fact leads to the name *mirror fermions.* The assumption of the existence of mirror fermions would then make the extended theory of the weak interactions left-right symmetric, which is a goal of most unification schemes. An extension of the Standard Model containing mirror fermions was first suggested by Pati and Salam[38] in 1975, and an excellent review of the physics of mirror fermions can be found in ref. 39 .

The mass terms of the mirror fermions in the extended theories arise, just like

those of the ordinary (V−A) fermions, through the Higgs mechanism. Therefore, there are no definite predictions on the masses of the mirror fermions. Since no mirror fermions have yet been discovered in accelerator experiments, the left-right symmetry of these theories must be broken at some scale above the masses of the known fermions.

2.4.1.1 *Stable charged mirror leptons*

It is possible for the lightest charged mirror lepton to be long-lived in a selected class of left-right symmetric theories. The lifetime of such a charged mirror lepton would be on the order of 10^{-8} sec., if its mass is in the range accessible to our stable particle search.[40] This long lifetime arises in these theories due to restrictions on the interactions between mirror and regular leptons that prevent the immediate decay of a mirror into a regular lepton.

In the simplest left-right symmetric theories, the left- and right-handed couplings of the mirror fermions are interchanged with respect to the Standard Model couplings for the regular leptons given by eqn. 2.18.

2.4.2 *Supersymmetry*

Another type of extension of the Standard Model is given by the introduction of a *supersymmetry* which interrelates fermions and bosons. An excellent review of the supersymmetric extensions of the Standard Model can be found in ref. 41. The supersymmetry is introduced through a self-conjugate operator Q_λ which can change the total angular momentum of a state by 1/2. This operator has the effect of turning bosons into fermions

$$Q_\lambda|boson\rangle = |fermion\rangle, \tag{2.33}$$

and fermions into bosons

$$Q_\lambda|fermion\rangle = |boson\rangle. \tag{2.34}$$

It also has the property that two successive transformations involve a space-time translation. Since the supersymmetry is assumed to be a local symmetry, different points in space time can transform in different ways resulting in an acceleration between points. This, in turn, is equivalent to gravity. Thus, supersymmetry may allow for the introduction of gravity into the theory of elementary particle physics.

The main consequence of supersymmetry is that there is a supersymmetric partner boson for every quark and lepton in the Standard Model and likewise, a fermionic partner exists for each of the gauge and Higgs bosons. A summary of these particles is given in Table 2.5.

Table 2.5. Spectrum of supersymmetric particles.

Standard Particle	Spin	Supersymmetric Particle	Spin
lepton $l_{L,R}$	$\frac{1}{2}$	slepton $\tilde{l}_{L,R}$	0
neutrino ν_L	$\frac{1}{2}$	sneutrino $\tilde{\nu}_L$	0
quark $q_{L,R}$	$\frac{1}{2}$	squark $\tilde{q}_{L,R}$	0
photon γ	1	photino $\tilde{\gamma}$	$\frac{1}{2}$
gluon g	1	gluino $\tilde{g}$	$\frac{1}{2}$
W	1	wino $\tilde{W}$	$\frac{1}{2}$
Z	1	zino $\tilde{Z}$	$\frac{1}{2}$
Higgs H	0	Higgsino $\tilde{H}$	$\frac{1}{2}$

If supersymmetry were an exact symmetry of nature, then the masses of the supersymmetric partner particles would be equal to the masses of the standard particles. In current experiments, no known particle can be the superpartner of any other known particle. This means that supersymmetry must, if it exists, be broken in such a way that the supersymmetric partners of the known particles would all have larger masses. Again, these masses are not predicted by the theory. The couplings, however, are specified and are the same as those in the Standard Model because su-

persymmetry operations do not change the weak isospin and hypercharge quantum numbers of particles. A knowledge of the couplings helps facilitate the search for such new particles with supersymmetric properties, i.e., bosonic leptons or fermionic force particles, since their production rates in experiments can then be calculated.

2.4.2.1 *Stable charged scalar leptons*

In supersymmetry, particles are assigned a quantum number known as R-parity defined by

$$R = (-)^{3B+L+2J}, \tag{2.35}$$

where B is the baryon number, L is the lepton number and J is the intrinsic spin angular momentum of the system of particles. The R-parity is equal to $+1$ for the known fundamental particles and is equal to -1 for the superpartners. In several versions of the theory, the R-parity is conserved and the supersymmetric particles are always produced in pairs and then decay into the lighter supersymmetric particles with the lightest being stable. Thus the charged scalar-lepton could be stable if it is the lightest supersymmetric particle.

2.5 Previous searches for stable charged particles

Direct searches for new heavy stable charged particles have been conducted in various experiments over the past fifty years. We will limit our discussion here to the accelerator experiments since, in these, the expected rate of production of the new particles discussed above can be determined.

2.5.1 *Searches in electron-positron collisions*

Each time a higher center-of-mass energy is achieved by an e^+e^- storage ring, an obligatory search for new stable charged particle production is made. Early searches in e^+e^- collisions were made at SPEAR[42] followed by searches at PEP and PETRA energies (see ref. 43 for a compilation of results) as well as searches at TRISTAN.[44,45]

Assuming that the new particles are produced as a particle-antiparticle pair, which are exclusive in the final state, the mass reach of a search is given by one-half of the center-of-mass collision energy. The mass reach of the searches performed at the above accelerators is illustrated in fig. 2.8 together with the mass reach of the SLC.

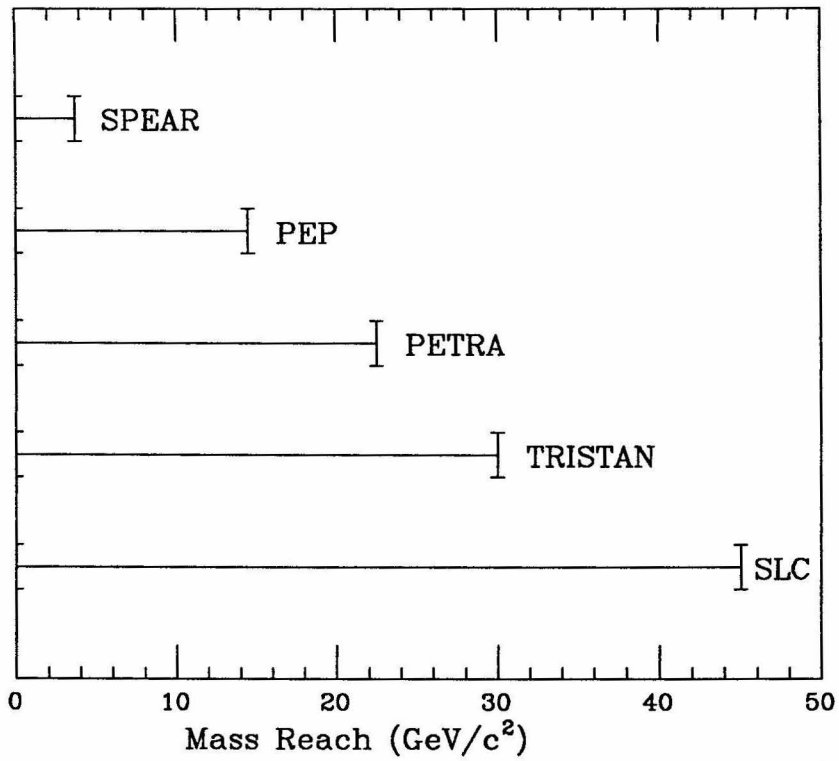

Figure 2.8. Mass reach of stable charged particle searches in e^+e^- collisions at various accelerators.

In experiments at SPEAR, PEP, PETRA and TRISTAN referenced above, searches were made for the pair production of stable fourth generation charged leptons and stable mirror fermions. No evidence for the existence of such particles was found. The best 95% confidence level lower limit on their mass was set at 28.2 GeV/c^2 by the TOPAZ Collaboration[45] at TRISTAN. The TOPAZ limit superseded the limit of 21.1 GeV/c^2 set by the JADE Collaboration[46] at PETRA. These limits are shown in fig. 2.9 as excluded regions of the plane formed by the mass of the fourth generation neutrino M_{ν_4} versus the mass of the charged lepton M_{l_4}. Also shown in the figure

is the search region which is kinematically accessible at SLC. In searches for stable charged scalar leptons, the best lower mass limit of 26.3 GeV/c^2 was also set by TOPAZ[45] which superseded the JADE[47] limit of 20.9 GeV/c^2.

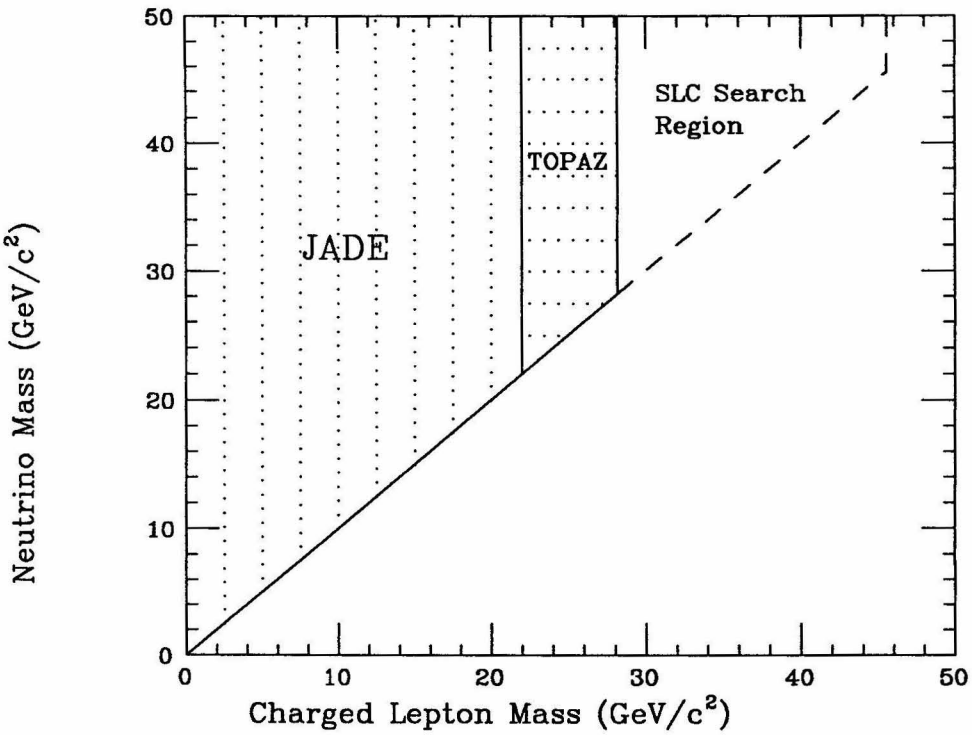

Figure 2.9. Existing mass limits on fourth generation stable charged leptons.

2.5.2 *Searches in proton-antiproton collisions*

A search for the production of heavy stable charged particles has been conducted in the 1.8 TeV center-of-mass energy proton-antiproton collisions at the Fermilab Tevatron Collider. No events consistent with the pair production of stable charged particles in the mass range 50-200 GeV/c^2 were found.[48] At the same time, the production cross-section for these events in $p\bar{p}$ collisions was limited to a level of about 1 nano-barn. This cross-section limit is, however, above the cross-section expected for the production of stable fourth generation charged leptons or supersymmetric scalar leptons.

2.6 Summary

At present, the Standard Model is tremendously successful. It provides a mathematical framework which describes all of the observed weak and electromagnetic interactions. The weakness of the theory lies in the fact that it requires substantial experimental input in order to complete its description. For example, the numbers and masses of the fermions are input to the theory. Also, the pure (V−A) form of the weak charged current interaction which describes the violation of parity conservation observed in the weak interactions does not arise from basic principles.

Among the many fundamental questions not answered by the Standard Model, two have important implications which can be addressed by the particle search of this thesis. They are: why do we observe only three families of quarks and leptons, and, why aren't the weak interactions left-right symmetric? These questions, together with a desire to include a description of the strong interactions and gravity, have prompted the construction of theories which incorporate a broader spectrum of phenomena. The predictions of such theories include a fourth generation of quarks and leptons within the Standard Model, right-handed weak interactions between mirror fermions, and a supersymmetry between fermions and bosons. The theories selected above all lead to the possibility of the existence of new stable charged particles in the form of fourth generation leptons, mirror leptons, or supersymmetric scalar leptons.

Past experimental searches have set lower limits on the possible masses of the new stable charged particle candidates listed above. The copious production of the Z boson at the SLC allows us to search for such new particles in the mass range above that previously accessible in e^+e^- collisions. Our search method involves selecting those Z decays with two charged particles in the final state which have momenta that are equal in magnitude but opposite in direction. The masses of such particles are determined from momentum, dE/dx, and time-of-flight measurements made by the MARK II detector. This general search is independent of the knowledge of the couplings of the new particles to the Z; however, the results can be interpreted in

terms of the above candidate particle types for which the couplings can be calculated. In particular, our search for a stable fourth generation charged lepton will complement the other searches for fourth generation quarks and leptons conducted so far at SLAC, CERN and Fermilab.

Chapter 3

Z production and Decay

The intermediate neutral vector boson Z can be produced as a real particle in e^+e^- collisions, via the interaction shown in fig. 2.2(c). We derive in this chapter the total cross-section for this process as well as the expressions giving the partial decay widths of the Z into various particle species.

3.1 Electron-positron annihilation

The Feynman diagrams for e^+e^- annihilation at SLC energies are shown in fig. 3.1. The Feynman rules for the electroweak couplings at each interaction vertex are given by eqns. 2.15 and 2.17. The matrix elements for the photon exchange and Z exchange processes shown in the figure are given by the product of the coupling at each vertex with a term to take into account the gauge boson acting as propagator. If we adopt the notation of C. Quigg[1], these matrix elements are given by

$$\begin{aligned}
\mathcal{M}(e^+e^- \to \gamma \to f\bar{f}) &= -ie^2\bar{u}(f,q_-)\gamma_\lambda Q_f v(f,q_+)\frac{g^{\lambda\nu}}{s}\bar{v}(e,p_+)\gamma_\nu u(e,p_-), \\
\mathcal{M}(e^+e^- \to Z \to f\bar{f}) &= \frac{i}{2}\left(\frac{G_F M_Z^2}{\sqrt{2}}\right)\bar{u}(f,q_-)\gamma_\lambda[R_f(1+\gamma_5)+L_f(1-\gamma_5)]v(f,q_+) \\
&\quad \times \frac{g^{\lambda\nu}}{s-M_Z^2}\bar{v}(e,p_+)\gamma_\nu[R_e(1+\gamma_5)+L_e(1-\gamma_5)]u(e,p_-),
\end{aligned} \tag{3.1}$$

where the propagator terms are $g^{\lambda\nu}/s$ for the photon and $g^{\lambda\nu}/(s-M_Z)$ for the Z , Q_f is the electric charge of the fermions, $g^{\lambda\nu}$ is the metric tensor, λ and ν are spinor

indices, s is the square of the center-of-mass energy of the e^+e^- collision, M_Z is the mass of the Z pole, and R and L are the right- and left-handed coupling constants given by eqn. 2.18. Here, u and v are the positive and negative energy Dirac spinors that represent the initial state electrons or final state fermions with four momenta p and q respectively. For this thesis, we consider the case of e^+e^- collisions at the SLC. In this case the mass of the electron is small as compared to $\sqrt{s}/2$ and can be neglected. The four momenta of the initial and final state fermions are then given by

$$\begin{aligned} p_+ &= (\frac{\sqrt{s}}{2}, 0, 0, \frac{\sqrt{s}}{2}), \\ p_- &= (\frac{\sqrt{s}}{2}, 0, 0, -\frac{\sqrt{s}}{2}), \\ q_+ &= (\frac{\sqrt{s}}{2}, \frac{\beta\sqrt{s}}{2}\sin\theta, 0, \frac{\beta\sqrt{s}}{2}\cos\theta), \\ q_- &= (\frac{\sqrt{s}}{2}, \frac{\beta\sqrt{s}}{2}\sin\theta, 0, -\frac{\beta\sqrt{s}}{2}\cos\theta), \end{aligned} \tag{3.2}$$

where θ is the polar angle with respect to the SLC beam line and β is the velocity of the final state fermion and is related to its mass M_f by

$$\beta = \sqrt{1 - 4\frac{M_f^2}{s^2}}. \tag{3.3}$$

For the general case of a two-body final state $a \equiv (1,2) \rightarrow (3,4) \equiv b$, the differential cross-section is given by

$$\frac{d\sigma}{d\Omega} = \frac{|\mathcal{M}_{ab}|^2}{64\pi^2 s}(\frac{\mathcal{S}_{34}}{\mathcal{S}_{12}}), \tag{3.4}$$

where

$$\mathcal{S}_{ij} = [s - (m_i + m_j)^2]^{1/2}[s - (m_i - m_j)^2]^{1/2}. \tag{3.5}$$

Neglecting again the mass of the electron in eqn. 3.5, eqn. 3.4 for the differential cross-section becomes

$$\frac{d\sigma}{d\Omega}(e^+e^- \rightarrow f\bar{f}) = \frac{|\mathcal{M}(e^+e^- \rightarrow \gamma \rightarrow f\bar{f}) + \mathcal{M}(e^+e^- \rightarrow Z \rightarrow f\bar{f})|^2}{64\pi^2 s}\beta. \tag{3.6}$$

A messy but straight-forward calculation, inserting eqn. 3.1 into eqn. 3.6and averaging over initial spins and summing over final spins, gives the spin-averaged cross-section

$$\begin{aligned}\frac{d\sigma}{d\Omega}(e^+e^- \to f\bar{f}) =& \frac{\alpha^2\beta Q_f^2}{4s}(1+\cos^2\theta+(1-\beta^2)\sin^2\theta) \\ &- \frac{\alpha\beta Q_f G_F M_Z^2(s-M_Z^2)}{16\pi\sqrt{2}[(s-m_Z^2)^2+M_Z^2\Gamma_Z^2]} \\ &\times [(R_e+L_e)(R_f+L_F)(1+\cos^2\theta+(1-\beta^2)\sin^2\theta) \\ &\quad + 2(R_e-L_e)(R_f-L_f)\beta\cos\theta] \\ &+ \frac{\beta G_F^2 M_Z^4 s}{256\pi^2\sqrt{2}[(s-m_Z^2)^2+M_Z^2\Gamma_Z^2]} \\ &\times [(R_e^2+L_e^2)(R_f^2+2L_fR_f+L_F^2)(1+\cos^2\theta+(1-\beta^2)\sin^2\theta) \\ &\quad + (R_e^2+L_e^2)(R_f^2-2L_fR_f+L_F^2)\beta^2(1+\cos^2\theta) \\ &4(R_e^2-L_e^2)(R_f^2-L_f^2)\beta\cos\theta],\end{aligned} \tag{3.7}$$

where the Z propagator has been replaced with the Breit-Wigner form appropriate for an unstable particle of total width Γ_Z. We make the following substitutions using the expressions for the right- and left-handed coupling constants given by eqn. 2.18

$$\begin{aligned}A_f &= (L_f - R_F) = 2T_{3f}, \\ V_f &= (L_f + R_f) = 2T_{3f} - 4Q_f \sin^2\theta_W,\end{aligned} \tag{3.8}$$

which define the vector V_f, and axial-vector A_f coupling constants. A form of the differential cross-section separating the contribution from γ and Z exchange, and the interference effect can be obtained by expressing the Fermi weak coupling constant G_F in terms of the mass of the Z boson and the weak mixing angle

$$G_F = \frac{\pi\alpha}{\sqrt{2}M_Z^2}\frac{1}{\sin^2\theta_W\cos^2\theta_W}. \tag{3.9}$$

It is given by[6]

$$\begin{aligned}\frac{d\sigma}{d\Omega}(e^+e^- \to f\bar{f}) = \\ \gamma: \quad & \frac{\alpha^2\beta}{4s}\Big[Q_f^2[1+\cos^2\theta+(1-\beta^2)\sin^2\theta] \\ \gamma - Z: \quad & -2Q_f\chi_1\{V_eV_f[1+\cos^2\theta+(1-\beta^2)\sin^2\theta]-2A_eA_f\beta\cos\theta\} \\ Z: \quad & +\chi_2\{V_f^2(A_e^2+V_e^2)[1+\cos^2\theta+(1-\beta^2)\sin^2\theta] \\ & +\beta^2A_f^2(A_e^2+V_e^2)[1+\cos^2\theta]-8\beta V_eV_fA_eA_f\cos\theta\}\Big],\end{aligned} \tag{3.10}$$

where

$$\chi_1 = \frac{1}{16\sin^2\theta_W\cos^2\theta_W}\frac{s(s-M_Z^2)}{(s-M_Z^2)^2+\Gamma_Z^2M_Z^2}, \tag{3.11}$$

and

$$\chi_2 = \frac{1}{256\sin^4\theta_W\cos^4\theta_W}\frac{s^2}{(s-M_Z^2)^2+\Gamma_Z^2M_Z^2}. \tag{3.12}$$

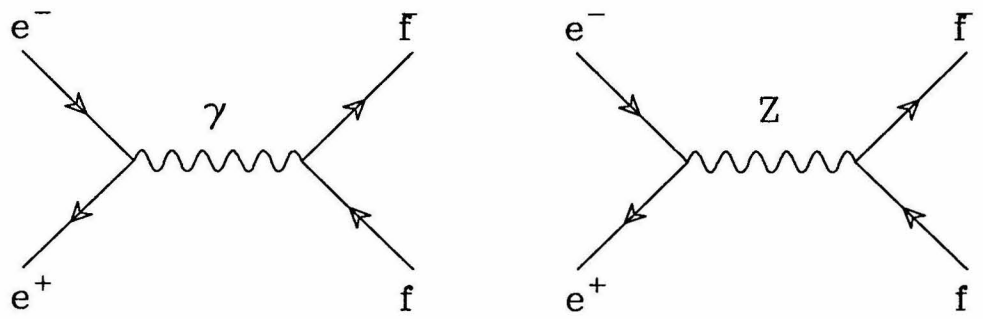

Figure 3.1. Lowest order diagrams contributing to $e^+e^- \to f\bar{f}$

The term labeled γ in eqn. 3.10 is the electromagnetic contribution due to photon exchange only. It dominates the total cross-section at low energies, and, due to its $1/s$ dependence, falls off rapidly as the center-of-mass energy of the collision increases.

The $\gamma - Z$ term accounts for the interference between the weak and electromagnetic diagrams shown in fig. 3.1. The interference term has a small but measurable effect on the total cross-section for energies above 20 GeV. Its relative contribution has a strong energy dependence with increasing $\sqrt{s}$, rapidly changing sign at the Z pole. The term labeled Z represents the effect of the Z exchange alone and its contribution can be seen as a large peak in the cross-section at $E_{\rm cm}$=M_Z, i.e., at 91 GeV/c^2. An integral form of this expression that accounts for all the fundamental fermions (including a factor of three for color each quark), and which is integrated over $\cos\theta$, is shown in fig. 3.2.

3.2 Z production cross-section

At the SLC, where the center-of-mass energy is approximately equal to the Z boson mass, the contribution to the total cross-section from the γ exchange and $\gamma - Z$ interference terms in eqn. 3.10 is at most 0.05%. If one is not concerned with the accuracy of the cross-section at this level, it is convenient to consider it as due to Z exchange alone. In this case, the total cross-section for fermion-antifermion production is given by the integral of the Z term in eqn. 3.10 over the solid angle:

$$\sigma_{f\bar{f}} = \frac{12\pi}{M_Z^2} \frac{s\Gamma_{ee}\Gamma_{ff}}{[(s - M_Z^2)^2 + M_Z^2\Gamma_Z^2]}. \tag{3.13}$$

The partial decay width Γ_{ff} into fermion-antifermion pairs is given by

$$\begin{aligned} \Gamma_{ff} &= \frac{\alpha M_Z}{48 \sin^2\theta_W \cos^2\theta_W} \beta[\frac{1}{2}(3 - \beta^2)V_f^2 + \beta^2 A_f^2] \\ &= \frac{G_F M_Z^3}{24\sqrt{2}\pi} \beta[\frac{1}{2}(3 - \beta^2)V_f^2 + \beta^2 A_f^2]. \end{aligned} \tag{3.14}$$

In the specific case of the partial width Γ_{ee} for the decay of the Z to e^+e^- , we have

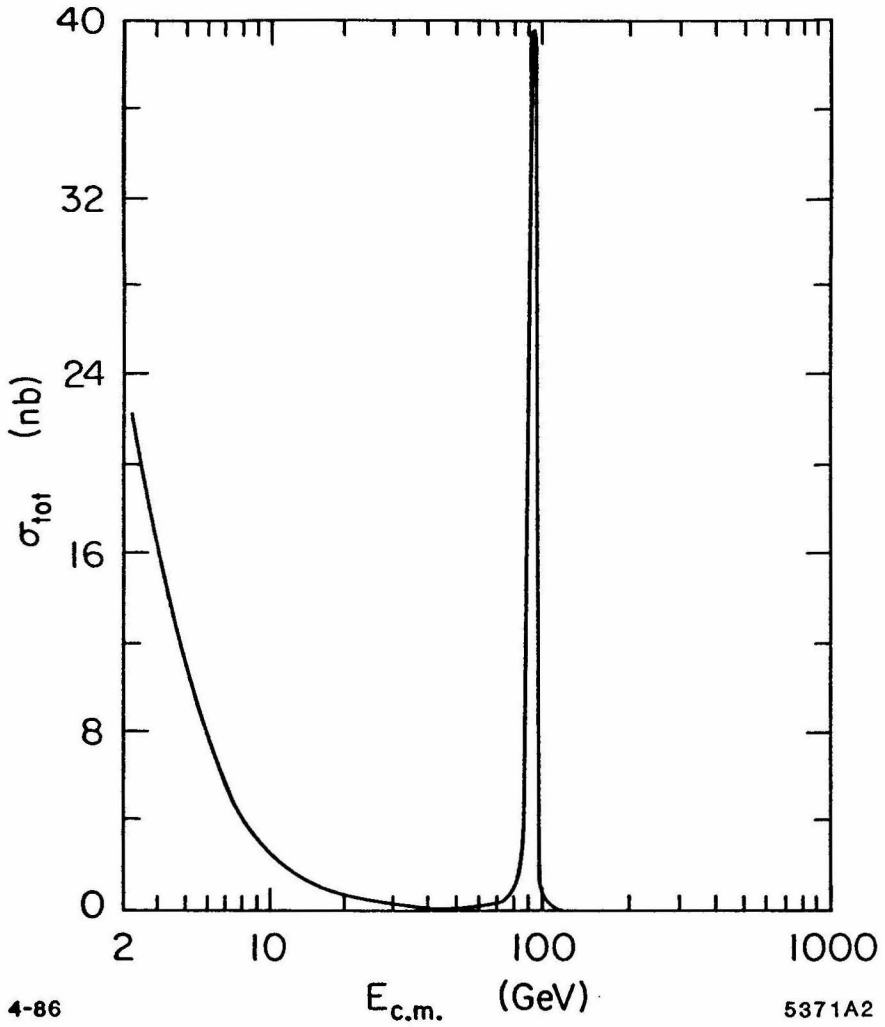

Figure 3.2. Total cross-section for $e^+e^- \to f\bar{f}$ as calculated in the Standard Model.

$\beta = 1$ and the above expression reduces to

$$\begin{aligned}\Gamma_{ee} &= \frac{\alpha M_Z}{48 \sin^2\theta_W \cos^2\theta_W}[V_f^2 + A_f^2] \\ &= \frac{G_F M_Z^3}{24\sqrt{2}\pi}[V_f^2 + A_f^2].\end{aligned} \tag{3.15}$$

3.3 Z decay to leptons

For comparative purposes, it is useful to calculate the numerical values for the partial decay widths of the Z into different particle types. We see from eqn. 3.14 that the partial widths for the Z decay into fermions depends on quantities that are not specified in the Standard Model must be derived from experimental measurements. For the values[19,6] M_Z=91.14 and $\sin^2\theta_W$=0.23 we arrive at the numerical values

$$\begin{aligned} \Gamma_{l^+l^-} &= 0.083 \text{ GeV}/c^2, \\ \Gamma_{\nu_l\bar{\nu}_l} &= 0.166 \text{ GeV}/c^2, \end{aligned} \tag{3.16}$$

where $l = e, \mu, \tau$ and where we have made the approximation $\beta = 1$. The total width for the decay of the Z into all leptons is then equal to

$$\Gamma_l = 3 \times (\Gamma_{l^+l^-} + \Gamma_{\nu_l\bar{\nu}_l}) = 0.75 \text{ GeV}/c^2. \tag{3.17}$$

3.4 Z decay to quarks

We can compute the partial decay widths of the Z into charge 1/3 and 2/3 quarks in the same way as for the decay into leptons described above:

$$\Gamma_{q\bar{q}} = \begin{cases} 0.285 \text{ GeV}/c^2, & \text{for } Q_f = \frac{2}{3}; \\ 0.367 \text{ GeV}/c^2, & \text{for } Q_f = \frac{1}{3}. \end{cases} \tag{3.18}$$

It should be noted that values of these partial widths contain a factor of three to account for the three distinct color states each of each quark flavor. The total width of the Z decay to quarks is then given by

$$\Gamma_h = \sum_{q=u,d,c,s,b} \Gamma_{q\bar{q}} = 1.67 \text{ GeV}/c^2. \tag{3.19}$$

In the decay of the Z boson to a quark-antiquark pair, the quarks do not leave the decay vertex as bare quarks but dress themselves into hadrons in a process called

fragmentation. In this process, additional quark-antiquark pairs are created by the color force field between the two original quarks. These additional quarks then combine among themselves and with the original quarks to form color neutral hadrons. To conserve the momentum of the original quarks, the hadrons form two opposing *jets* of particles in the final state.

The fragmentation process is not described at present by any of the fundamental principles of QCD. It is, however, successfully modeled by two different approaches: string fragmentation[49] and cluster fragmentation.[50] The process $Z \rightarrow q\bar{q}$ is modeled using the string fragmentation scheme by the LUND parton shower[51] and LUND matrix element[52] Monte Carlo simulations, while the Webber[53] and Caltech-II[54] simulations use the cluster fragmentation scheme. The comparison of these simulations with the SLC data can be found in refs. 55 and 56.

3.5 Z total width, visible width and peak cross-section

The total decay width Γ_Z for Z decay into fermion-antifermion pairs is given by the sum of the partial decay widths for Z decays into quarks and leptons

$$\Gamma_Z = \Gamma_l + \Gamma_h = 2.4 \text{ GeV}/c^2. \tag{3.20}$$

Since the final state neutrinos are not visible in the detectors used at e^+e^- colliders, it is useful to define the "visible" width for Z decay into detectable particles:

$$\Gamma_{vis} = \Gamma_Z - \sum_{l=e,\mu,\tau} \Gamma_{\nu_l \bar{\nu}_l} = 1.9 \text{ GeV}/c^2. \tag{3.21}$$

The total visible cross-section is written as:

$$\sigma_Z(E_{cm}) = \frac{12\pi}{M_Z^2} \frac{s\Gamma_{ee}\Gamma_{vis}}{[(s - M_Z^2)^2 + M_Z^2\Gamma_Z^2]}. \tag{3.22}$$

The cross-section at the Z peak, σ_0, is found by setting the center-of-mass energy $E_{cm} \equiv \sqrt{s} = M_Z$, which gives

$$\sigma_0 = \frac{12\pi}{M_Z^2} \frac{\Gamma_{ee}\Gamma_{vis}}{\Gamma_Z^2}. \tag{3.23}$$

For the value M_Z=91 GeV/c^2, we arrive at the numerical value σ_0=48 nb. About 87% (given by Γ_h/Γ_{vis}) of detectable Z decays have hadronic final states and the other 13% are shared equally between each of the 3 charged lepton-antilepton final states.

3.6 Radiative Corrections

The values of the Z total cross-section and decay width are affected by electroweak and QCD radiative processes. These effects, neglected so far, must be carefully taken into account in precise calculations of the expectations of the Standard Model before the above quantities can be compared with experimental measurements. The radiative processes to be considered are summarized in fig. 3.3. We will now discuss the effects of each of these processes on the Z boson production cross-section and decay width.

3.6.1 QCD radiative corrections

The QCD radiative processes occur only in the decay of the Z with quarks in the final state. They have been calculated to first order in the strong coupling constant α_s as described in ref. 57. Their effect can be expressed as a modification of the vector and axial-vector couplings in eqn. 3.14 as

$$\begin{aligned} \frac{1}{2}(3-\beta^2) &\rightarrow \frac{1}{2}(3-\beta^2)\{1+\frac{4}{3}\alpha_s[\frac{\pi}{2\beta} - \frac{3+\beta}{4}(\frac{\pi}{2}-\frac{3}{4\pi})]\}, \\ \beta^2 &\rightarrow \beta^2\{1+\frac{4}{3}\alpha_s[\frac{\pi}{2\beta} - (\frac{19}{10}-\frac{22}{5}\beta+\frac{7}{2}\beta^2)(\frac{\pi}{2}-\frac{3}{4\pi})]\}. \end{aligned} \tag{3.24}$$

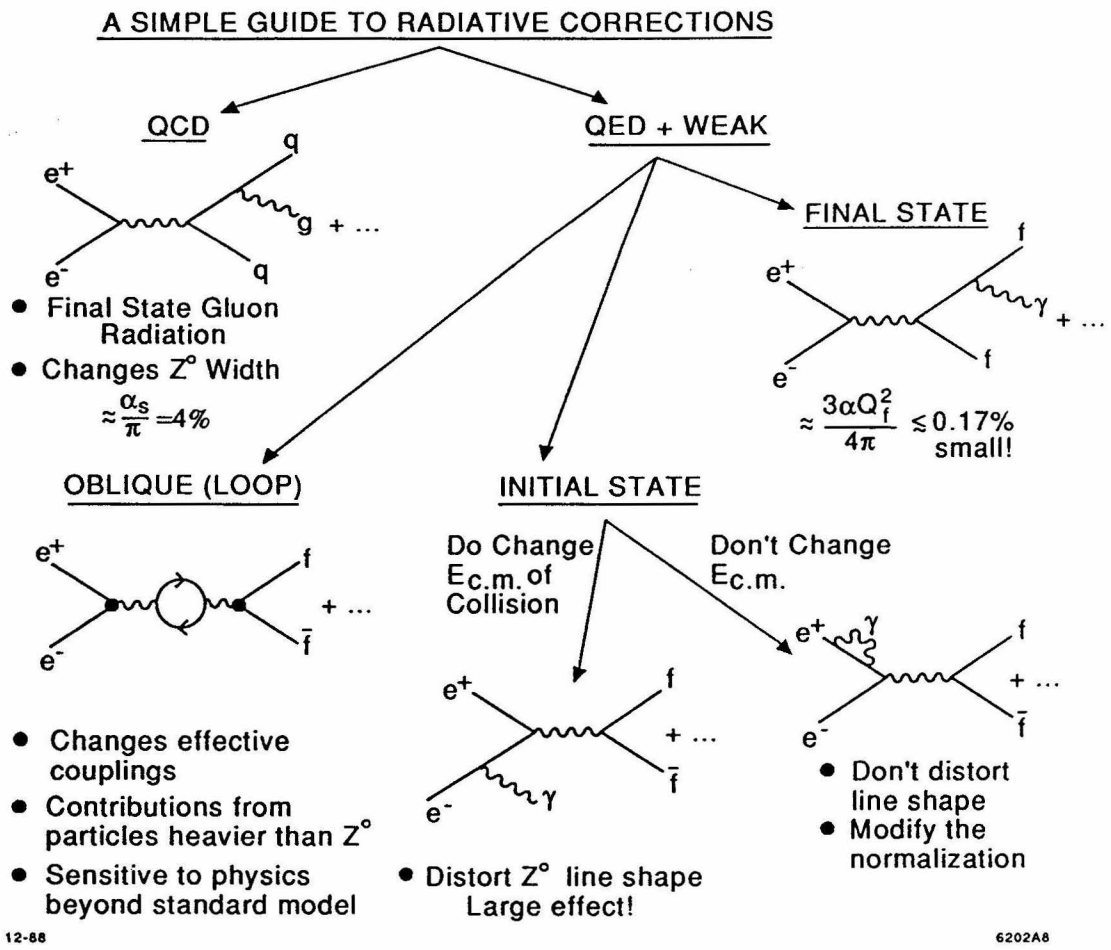

Figure 3.3. A simple guide to radiative corrections (taken from ref. 4).

For $\beta = 1$ and the current value[58] of $\alpha_s = 0.123$ these corrections change the partial decay widths by about 4%:

$$\Gamma_{qq} = \Gamma_{qq}(1 + \frac{\alpha_s}{\pi}) \simeq 1.04 \times \Gamma_{qq}. \tag{3.25}$$

3.6.2 *QED final state corrections*

QED final state radiation alters the partial widths into charged leptons and

quarks by[59]

$$\Gamma_{ff} = \Gamma_{ff}(1 + \frac{3\alpha Q_f}{4\pi}) \simeq \Gamma_{ff}(1 + 0.0017 Q_f). \tag{3.26}$$

These corrections are too small to be noticed in measurements at the SLC due to the size of the Z decay data sample. They are therefore neglected in this analysis.

3.6.3 QED initial state corrections

The QED initial state radiative processes shown in fig. 3.3 are very important. The main effect of a photon emission before the collision is to lower the center-of-mass energy of the e^+e^- annihilation which in turn changes the measured Z resonance shape. Calculations of this process are discussed extensively in ref. 59. The effect of initial state radiation on the resonance shape can be represented by a modified version of eqn. 3.13 given by Cahn[60] where the substitution

$$\Gamma_Z(s) = \frac{\sqrt{s}\Gamma_Z}{M_Z} \tag{3.27}$$

gives

$$\sigma_Z(E_{cm}) = \sigma_0 \frac{s\Gamma_Z^2}{(s - M_Z^2)^2 + s^2\Gamma_Z^2/M_Z^2}[1 + \delta(\sqrt{s})]. \tag{3.28}$$

Here, the function $\delta(s)$ gives the correction due to initial-state radiation. The difference between the uncorrected and corrected resonance line shape is shown in fig. 3.4. It is evident from the figure that the radiativly corrected cross-section is lower than the uncorrected case below the Z pole and higher above the pole. This is due to the fact that the initial state radiation lowers the center-of-mass energy of the collisions which effectively reduces the cross-section at energies below the Z pole and increases it for energies above the pole.

3.6.4 Loop corrections

Finally, we discuss the oblique corrections shown in fig. 3.3. These diagrams contain internal loops of fermions or bosons and change the effective couplings of the

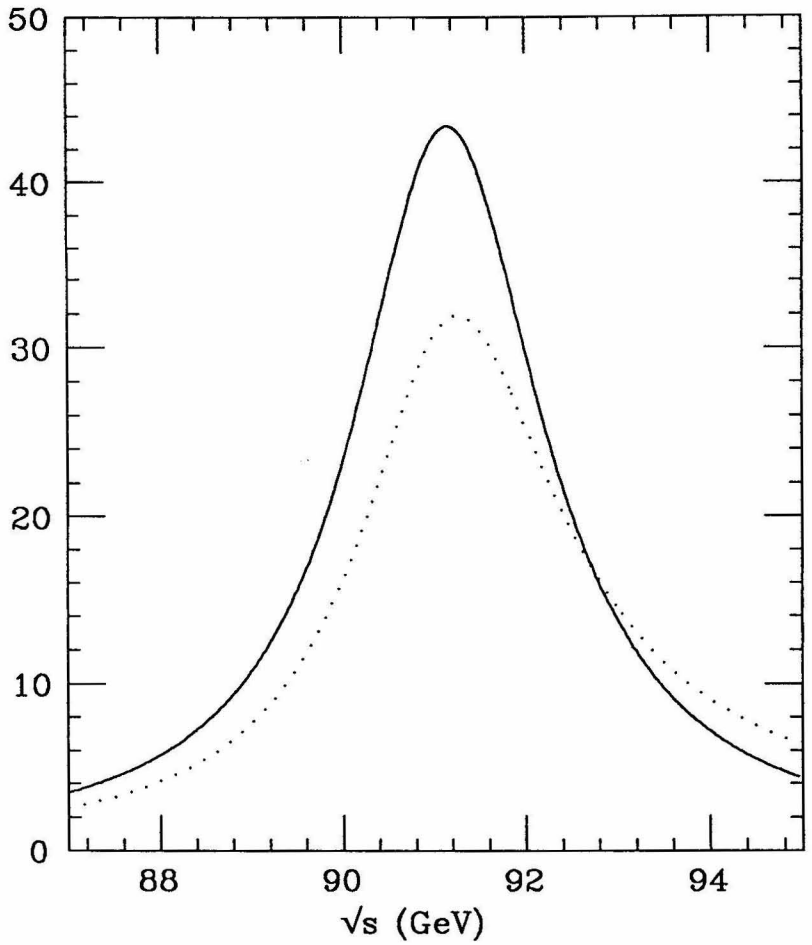

Figure 3.4. The effect of initial state radiative corrections on the Z resonance line shape. The solid curve is without corrections and the dotted curve is with corrections.

fundamental fermions to the Z. The contribution from the loop corrections is largest for the heaviest mass objects traveling on the loop and, therefore, these corrections are sensitive to the masses of the top quark and Higgs boson as well as any other new heavy particle. If the parameters of the Standard Model are specified as α, G_F and M_Z, then the electro-weak mixing angle θ_W defined by $\sin^2\theta_W$ is defined as[61]

$$\sin 2\theta_W = \left[\frac{4\pi\alpha}{\sqrt{2}G_F M_Z^2(1-\Delta r)}\right]^{1/2}. \tag{3.29}$$

Here, the effects of the loop corrections are represented by Δr. For a top mass and

a Higgs mass of 100 GeV/c^2 each, the value of Δr is 0.006. This correction enters the partial widths (eqn. 3.14) through the vector coupling constant V_f (eqn. 3.8).

3.7 Measurement of the Z mass and width at the SLC

The rate R_Z of Z boson production at the SLC can be written in terms of the total visible cross-section $\sigma_Z(E_{cm})$, given by eqn. 3.28, and the luminosity $\mathcal{L}$ of the e^+e^- collisions as

$$R_Z = \mathcal{L} \cdot \sigma_Z(E_{cm}). \tag{3.30}$$

Integration over time gives the number of Z's produced in a given time interval:

$$N_Z = \int \mathcal{L}dt \cdot \sigma_Z(E_{cm}). \tag{3.31}$$

If this equation is rearranged into the form

$$\sigma_Z(E_{cm}) = \frac{N_Z}{\int \mathcal{L}dt}, \tag{3.32}$$

it is evident that the cross-section at a fixed center-of-mass energy can be determined from a measurement of the number of events produced and the integrated luminosity.

A measurement of $\sigma_Z(E_{cm})$ was performed[19]at several center-of-mass energies with the MARK II detector at the SLC. The cross-section obtained from this energy scan has already been shown in fig. 2.4 . The number of Z bosons produced was determined at each energy point from the number of events detected in the MARK II after correcting for the detection efficiency. A total of 480 Z decays were detected over the entire energy scan. The integrated luminosity at each scan point was determined from a measurement of the number of Bhabha scattering events detected by the MARK II, N_B, and the calculated cross-section for the Bhabha elastic scattering process σ_B as

$$\int \mathcal{L}dt = \frac{N_B}{\sigma_B}. \tag{3.33}$$

The solid line in fig. 2.4 indicates a fit of eqn. 3.28 for the total visible cross-section including radiative corrections to the data with M_Z, Γ_Z and σ_0 taken as free parameters. The best fit is given by the values $M_Z = 91.14 \pm 0.12$ GeV/c^2, $\Gamma_Z = 2.42^{+0.45}_{-0.35}$ GeV and $\sigma_0 = 45 \pm 4$ nb. The solid line is unchanged for a second fit where Γ_Z and σ_0 are fixed to their Standard Model values with M_Z and the number of massless neutrino generations allowed to vary. This fit also results in the same value of the Z mass $M_Z = 91.14 \pm 0.12$ GeV/c^2 and gives the number of massless neutrino generations as $N_\nu = 2.8 \pm 0.6$. This corresponds to an upper limit of 3.9 massless neutrino generations at the 95% confidence level. The dashed curve in fig. 2.4 is the result of a fit where only M_Z is allowed to vary. This fit also gives an identical answer for the mass of the Z: $M_Z = 91.14 \pm 0.12$.

3.8 Mirror fermion production

The only modification needed to extend the cross-section given by eqn. 3.7 to mirror fermion production in Z decay is that the left- and right-handed couplings given by eqn. 2.18 must be interchanged with respect to the Standard Model couplings:

$$\begin{aligned} L_{mirror} &= -2Q_f \sin^2\theta_W, \\ R_{mirror} &= 2T_3 - 2Q_f \sin^2\theta_W. \end{aligned} \tag{3.34}$$

This gives the necessary change of sign of the axial-vector coupling constant for mirror fermions with respect to that for the standard leptons:

$$\begin{aligned} A_{mirror} &= (L_f - R_F) = -2T_{3f} = -A_f, \\ V_{mirror} &= (L_f + R_f) = 2T_{3f} - 4Q_f \sin^2\theta_W = V_f. \end{aligned} \tag{3.35}$$

The coupling constants appear in quadrature in the expression for the partial width for Z decay to fermions given by eqn. 3.14. Therefore, the total production rate of mirror fermions in Z decays is the same as that of ordinary fermions.

3.9 Supersymmetric scalar lepton production

The Z partial decay width to supersymmetric scalar leptons is different than that for decays to standard fermions. Since the supersymmetric partners have the same weak isospin and hypercharge quantum numbers as their regular partners, they must have the same couplings to the Z . Therefore, the difference in their partial widths arises from spin effects only. For the scalar leptons, the phase space near the threshold behaves[62] as β^3, and the corresponding angular distribution is proportional to $\sin^2\theta$. The rate of scalar lepton production in Z decay is then given by

$$\Gamma\left(Z \to \tilde{l}_{\mathrm{L}}^{+}\tilde{l}_{\mathrm{L}}^{-} + \tilde{l}_{\mathrm{R}}^{+}\tilde{l}_{\mathrm{R}}^{-}\right) = \frac{1}{2}\beta^3\Gamma\left(Z \to e^{+}e^{-}\right). \tag{3.36}$$

Here, it is assumed that the left- and right-handed scalar leptons, $\tilde{l}_{\mathrm{L}}$ and $\tilde{l}_{\mathrm{R}}$, are degenerate in mass.

Chapter 4

Experimental Apparatus

It has long been recognized that a conventionally designed electron-positron storage ring with beam energies of more than a few hundred GeV would be prohibitively large and expensive to build. This is due to the fact that the rate of synchrotron radiation energy loss suffered by the electrons and positrons in the ring bending magnets increases proportional to the fourth power of the beam energy and inversely proportional to the square of the radius of curvature of the ring.[63] Thus, to achieve higher beam energies and also keep the beam energy losses at currently manageable levels, the radii of any new storage rings must be increased beyond those of existing rings. For example, the collision energies on the order of 100 GeV at the Large Electron Positron storage ring (LEP) at CERN in Geneva required a ring design with a radius of 4.3 km corresponding to a 27 km circumference. The cost to actually build LEP was about one billion dollars. Planned future improvements in the ability to restore the beam energy lost to synchrotron radiation should allow the collision energy at LEP to reach 200 GeV, but it is clear that an alternative to the conventional storage ring is needed if we wish to explore even higher energies in e^+e^- collisions.

The linear collider concept solves the beam energy loss problem of storage rings by achieving e^+e^- collisions without the use of strong bending magnets. The idea here is to point two linear accelerators, one for electrons and one for positrons, head to head and allow the accelerated beams to come into collision.

The SLAC Linear Collider (SLC) was designed and built to test the principles of linear collider operation. It is not truly a linear collider as described above. Rather, it is an adaptation of the existing SLAC linac which now serves as the first operating linear single pass electron-positron collider. The SLC was proposed[64] in 1980 to provide e^+e^- collisions of sufficient energy and intensity so as to copiously produce the intermediate neutral vector Z boson (at that time, the Z boson resonance was postulated to be just below 100 GeV). Thus, in addition to its function as a testing ground for linear collider technology, the SLC was designed to play a second role as a forefront high energy physics research facility. Because of this second role, a detector was needed at the e^+e^- collision point of the SLC to exploit the exciting Z physics that would be made available.

The MARK II, a large general purpose particle detector, was chosen to be the first detector at the SLC. This decision was based on the previous successful operation of the MARK II at SPEAR in 1978 and 1979 and at PEP beginning in 1980. In order to insure its continued successful operation at the SLC, several of the MARK II detector subsystems were upgraded. The upgrade was needed to better equip the MARK II for handling the higher expected energies of particles produced in Z decays as compared to the energies of particles produced in the e^+e^- collisions at PEP or SPEAR.

The details of the MARK II detector, including the various upgrades, will be discussed below following a section on the details of the SLC. The upgraded detector was thoroughly checked in a test run at PEP before being moved to the SLC. Performance numbers obtained in that test run, and also obtained from the SLC data, will be presented whenever possible.

4.1 The SLAC Linear Collider

A schematic layout of the SLAC Linear Collider (SLC) is shown in fig. 4.1. In summary, it simultaneously accelerates separate bunches (often referred to as beams) of electrons and positrons to an energy of up to 50 GeV in a 2 mile long (10,000

feet) linear accelerator (linac). The beams are then split by a large dipole magnet and transported through separate collider arcs to their respective final focus systems. There, the beams are focused to a small transverse size and brought into collision before being extracted to beam dumps where the beam energies are measured. We will now fill in some of the details of SLC operation.

The following discussion refers to the layout of the SLC shown in fig. 4.1. SLC operation begins with the production of two electron bunches by a thermionic gun located at the e^- source. In the e^- booster, the bunches are compressed to a 2 mm length and are accelerated to an energy of 0.2 GeV. The electrons are joined by a bunch of positrons at the start of sector 1 and the three bunches are then accelerated to 1.2 GeV. At the end of sector 1, the beams are magnetically separated and transported into two separate storage rings called damping rings. Here, the beams transverse emittances and energy spreads are damped to the specified levels of $\gamma\epsilon = 4.0 \times 10^{-5}$ m-rad and $\Delta E/E = 1\%$. The damping is achieved through the replacement, in RF cavities, of the beam energy lost to synchrotron radiation.

After a time interval of 8.3 ms (or longer if the SLC repetition rate is below 120 Hz), the positron beam is magnetically kicked from its damping ring into a transport line where the bunch lengthening due to the damping is removed before it is injected into the 50 GeV accelerator linac. The electron bunches are likewise extracted, compressed and injected into the linac at 60 ns intervals following the positrons. Once the bunches have reached an energy of 33 GeV at the 2/3 point of the linac, the second electron bunch is kicked onto a positron production target. The resulting positrons are bunched, accelerated to 0.2 GeV and transported to the start of the accelerator where they join the next two electron bunches. The remaining electron and positron bunches are further accelerated to their full energies of up to 51 GeV.

After the electron and positron bunches have reached their full energies at the end of the accelerator, they are magnetically separated and transported though arc

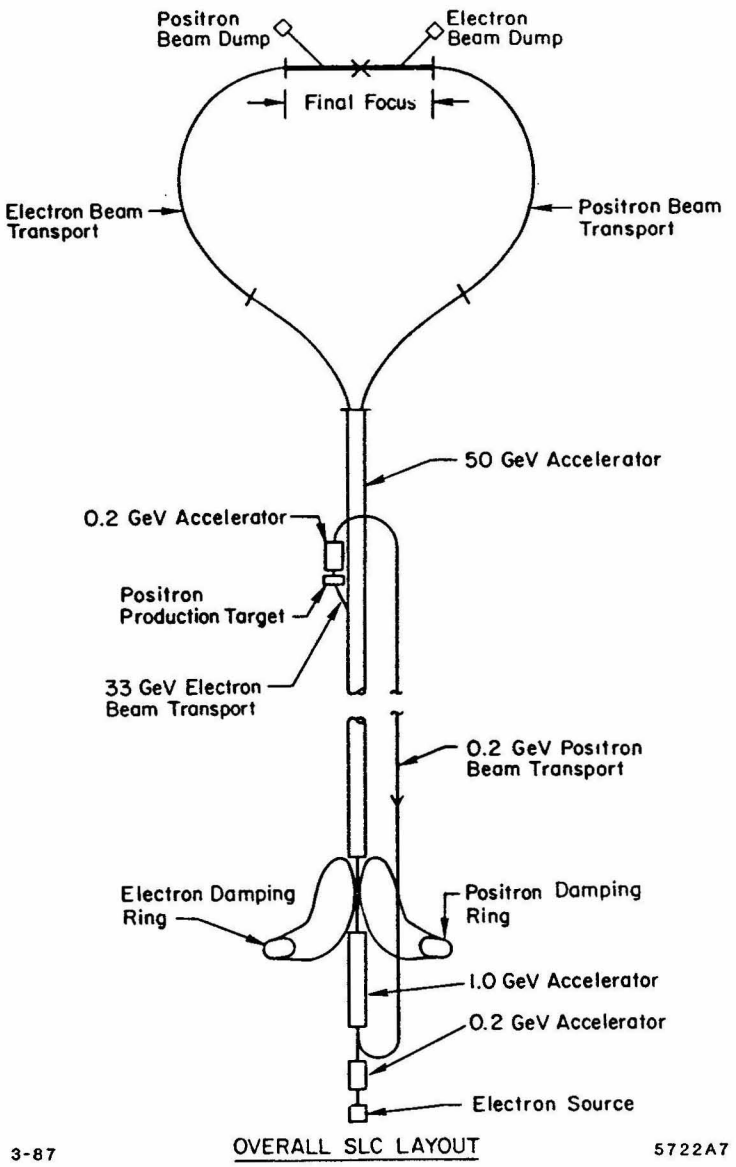

Figure 4.1. Schematic layout of the SLAC Linear Collider.

shaped beam transport lines to their respective final focus systems. The synchrotron radiation energy loss of the beams in the arcs is on the order of 2%. In the final focus

systems, the beams are transformed into dispersion-free round beams and brought into collision at the interaction point marked by an "×" in fig. 4.1. After they pass through one another, the beams are extracted into dumps where their energy is measured using precision spectrometers. The achieved energy resolution of the spectrometers is 35 GeV. The energy spectrometers will be discussed in more detail in the following section on the MARK II detector.

4.1.1 *Luminosity of the SLC*

The luminosity of the SLC can be determined from the frequency of beam interactions, f, the number of particles in the electron and positron bunches, N_- and N_+, and the rms transverse beam sizes at the interaction point, σ_x and σ_y, as

$$\mathcal{L} = \frac{f N_+ N_-}{4\pi\sigma_x\sigma_y}. \tag{4.1}$$

Typical values for these parameters during the running were $f = 60$ Hz, $N_+ = 1\times10^{10}$ per bunch, $N_- = 1.5\times10^{10}$ per bunch and $\sigma_x = \sigma_y = 4$ μm, yielding a luminosity of 4.5×10^{27} cm^{-2}sec^{-1}. At the peak radiativly corrected cross-section, this luminosity corresponds to a production rate of about 0.5 Z per hour.

4.2 The MARK II Detector

The MARK II detector is an upgraded version of the device previously used successfully at the PEP and SPEAR storage rings. Newly constructed components include the central drift chamber, the time-of-flight system, the solenoid coil, the endcap electromagnetic calorimeters and the luminosity monitors. A cut-away view of the MARK II detector is shown in fig. 4.2 and a side view is shown in fig. 4.3. It is currently installed at the SLC so that the Z bosons are produced at rest in the center of the detector volume. Particles from Z decay which are emitted perpendicular to the beam line would transverse the beampipe, the central drift chamber, a time-of-flight counter, the coil of the solenoid magnet, the liquid argon calorimeter and finally the

muon detection system. The following sections describe these components as well as the endcap calorimeters and small angle monitors with the exception of the time-of-flight system to which the next chapter is devoted. The following sections are based on a more detailed account of the upgraded detector found in ref. 65.

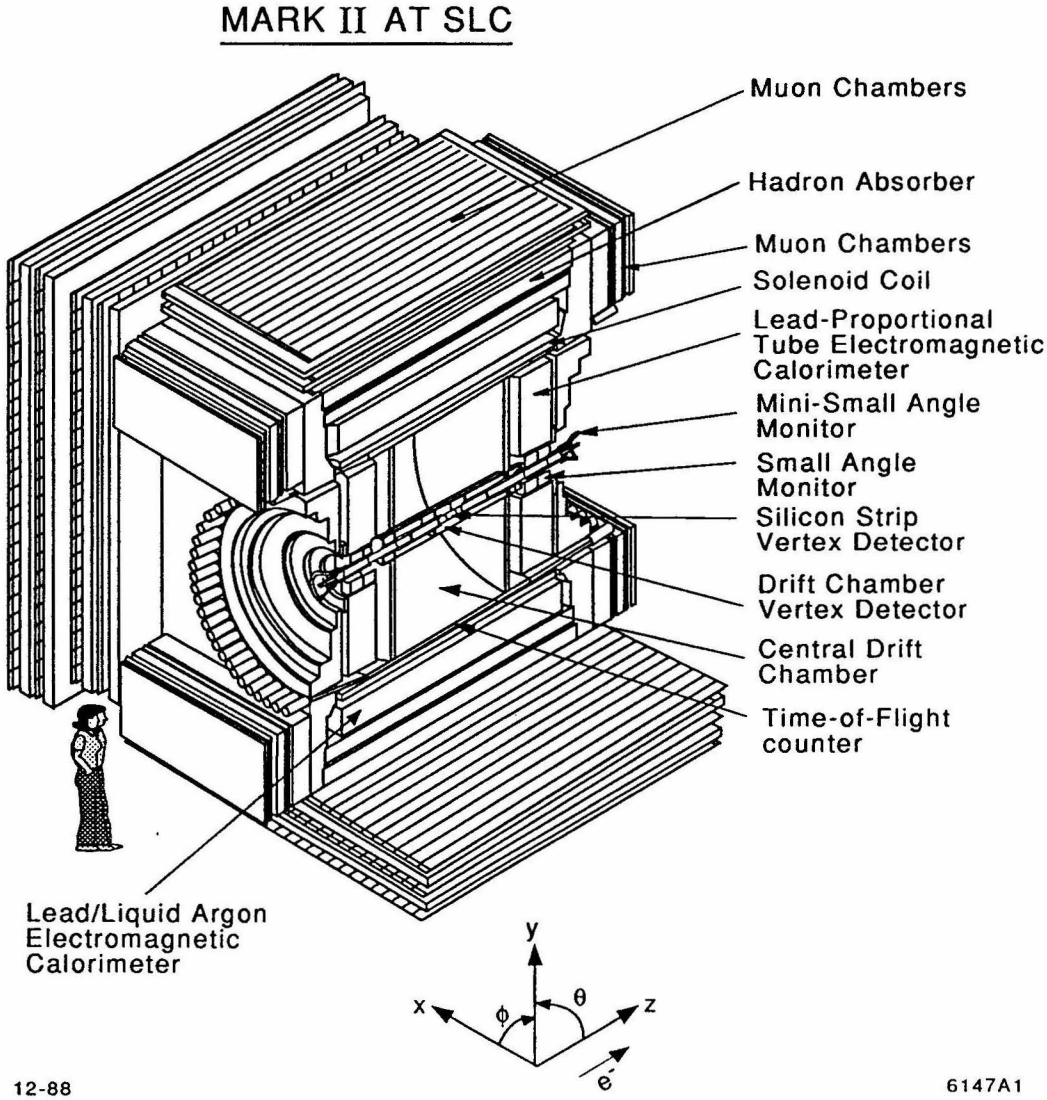

Figure 4.2. MARK II detector cut-away view showing major detector components.

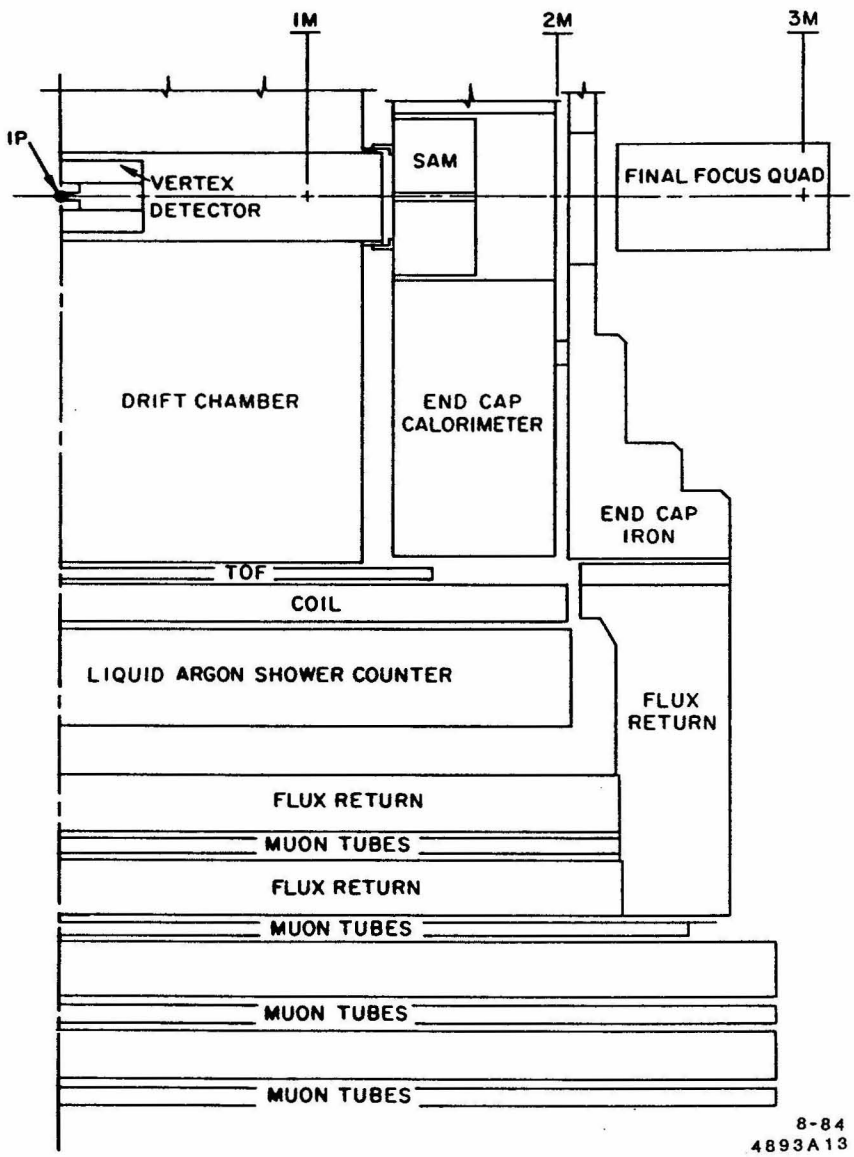

Figure 4.3. MARK II detector side view showing major detector components.

4.2.1 The central drift chamber

A new central drift chamber was built to provide state of the art charged particle tracking with good momentum resolution. A dE/dx system to measure the ionization energy loss of charged particles traversing the chamber was also provided.

For charged particle tracking, the central drift chamber has 12 concentric layers of 6 sense-wire jet chamber cells extending in radius from 19.2 to 151.9 cm. The geometry of a single cell is shown in fig. 4.4. The sense wires (30 μm diameter gold plated tungsten) are staggered $\pm 380\mu$m from the cell axis to provide local left-right ambiguity resolution. The electric field is controlled primarily by the voltage on a row of 19 field wires at each edge of the cell. There are also guard and potential wires interspersed with the sense wires which help to adjust the electric field and gains on the sense wires. The voltage on a field wire is typically -4.5 kV, the potential wires and guard wires are kept at -1.5 kV and -200 V respectively, and the sense wires are grounded. The chamber gas is a mixture of 89% Ar, 10% CO_2 and 1% CH_4 and is at a pressure slightly above 1 atmosphere. The above voltages result in a gas gain of 2×10^4 with an electric drift field of 900 V/cm. The typical drift velocity is 52 μm/ns.

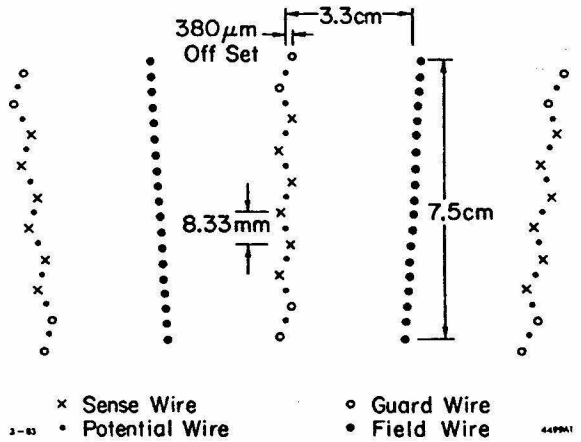

Figure 4.4. Upgrade drift chamber jet cell geometry

The signals collected on the sense wires are amplified in two stages before being digitized. They are split in the second stage forming separate signals, one for timing and one for pulse shape. The timing signals are digitized by TDCs with 2 ns bin width. The pulse shape signals are digitized by 100 MHz Flash-ADC's with 6-bit resolution.

Tracks can be reconstructed based on hit wires found by the TDCs. Track segments are first formed within cells and are later matched to form tracks through the chamber. The track-finding efficiency has been measured at PEP and estimated for SLC from Monte Carlo programs. Figure 4.5 shows the efficiency as a function of $\cos\theta$ where θ is the polar angle of the track with respect to the beam line as defined in fig. 4.2. From the figure we see that the efficiency for isolated tracks in Bhabha events at PEP is approximately 99% for angles up to $|\cos\theta| > 0.70$.

The chamber is enclosed in a 4.75 kG solenoidal magnetic field. A momentum resolution of $\sigma(p)/p^2 = 0.0031\ (\mathrm{GeV}/c)^{-1}$ has been achieved for isolated tracks constrained to originate at the beam interaction point during the test run at PEP. An additional contribution of $1.4\%p$ is added to account for multiple scattering, making the final resolution $\sigma_p/p = [(0.0031p)^2 + (0.014)^2]^{1/2}$. This resolution is confirmed at the SLC using $\mu^+\mu^-$ pair events and is discussed in more detail in Appendix A. The position resolution for tracks in the chamber is $\approx 170\mu$m.

The dE/dx measurement is made based on the charge collected on the sense-wires. The charge is derived from the Flash-ADC digitization of the amplified signal from each sense wire. The resolution achieved for minimum ionizing tracks at the SLC is 8.5% of the measured value. The dE/dx system performance at the SLC is discussed in more detail in Appendix A.

4.2.2 The solenoid coil

The MARK II solenoid is a conventional cylindrical water cooled aluminum coil. It is 405 cm long and has inner and outer radii of 156 and 171 cm, respectively, which

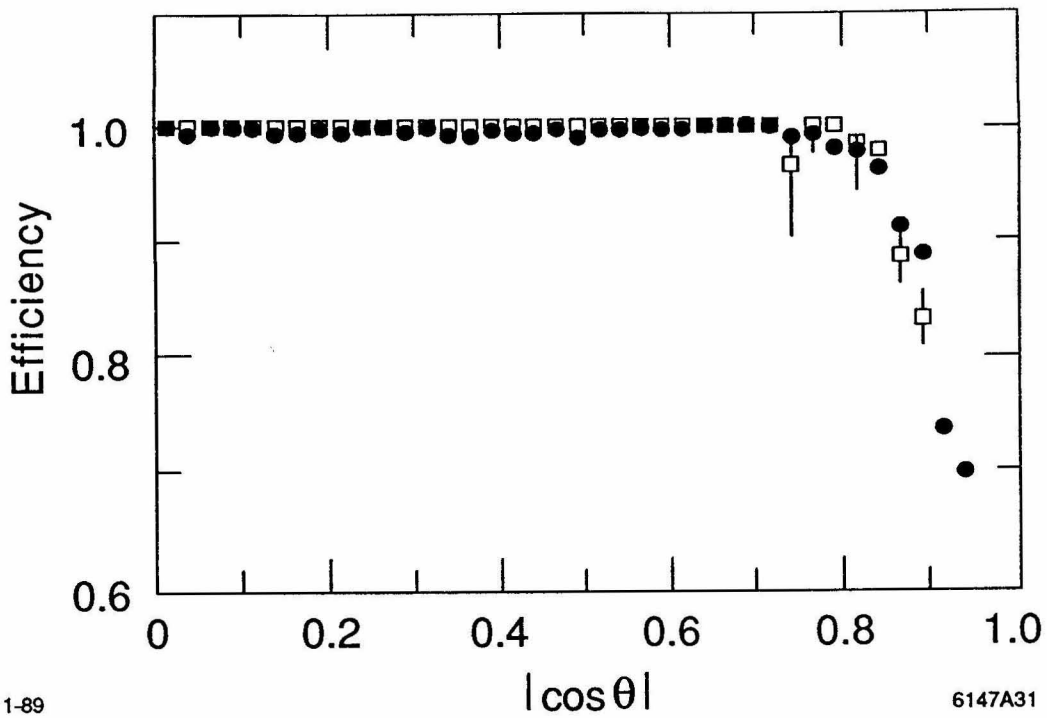

Figure 4.5. Tracking efficiency for the central drift chamber as a function of $|\cos\theta|$ where θ is the polar angle of the track with respect to the beam line as defined in fig. 4.2. The dots are for Bhabha scattering events from a sample of PEP data; the boxes are for hadronic events from a Monte Carlo study at SLC energies. Error bars are shown only for the Monte Carlo events.

is 1.3 radiation lengths. It produces a field of 4.75 kg using a current of 7325 A and dissipates 1.8 MW of power. Within the tracking volume, the field is uniform to within 3% and the absolute error on the field strength measurement is less than 0.1%.

4.2.3 The liquid argon barrel calorimeter

The central electromagnetic calorimeter of the MARK II is a lead/liquid argon sampling device with strip readout geometry. The calorimeter system consists of eight independent liquid argon cryostats enclosed in a common vacuum vessel arranged in an octagonal barrel outside of the solenoid coil. The modules each measure 3.8 m

along z and are 1.5 m wide and 0.21 m thick. They are located 1.8 m from the beam line and provide azimuthal coverage out to $|\cos\theta| = 0.68$, except for 3° gaps between each pair of modules. The total solid angle coverage of the barrel is 63.5%.

Each liquid argon module consists of alternating layers of 2 mm lead strips and lead sheets with 3 mm liquid argon gaps between as shown in fig. 4.6. the total material amounts to 14.4 radiation lengths at normal incidence. Altogether, 1.86 radiation lengths of material precede the lead stack. The lead sheets are kept at ground while the lead strips are kept at a potential of about +3.5kV and are instrumented to collect the ionization electrons created in the argon. The lead strip layers are oriented either perpendicular to the beam to measure the polar coordinate θ (labeled "T"), parallel to the beam to measure ϕ (labeled "F"), and at 45° relative to the other two orientations (labeled "U"). The layers are ganged together as shown in fig. 4.7 to reduce the total number of readout channels. The energy resolution of the system for 14.5 GeV Bhabha electrons at PEP was measured to be $\sigma(E)/E = 13.3\%/\sqrt{E} \oplus 3.3\%$, where E is measured in GeV.

4.2.4 The endcap calorimeter

The endcap calorimeters (ECCs) were added in the upgrade and increase the electromagnetic coverage of the detector to 86% of the full solid angle. They fully cover the angular region $0.71 < |\cos\theta| < 0.96$ and provide partial coverage down to $|\cos\theta| < 0.67$ which overlaps the coverage of the liquid argon barrel calorimeter. Each ECC consists of 36 layers, alternating 0.28 cm thick lead sheets with layers of proportional tubes. The total thickness of each ECC corresponds to 18 radiation lengths (X_0).

The 191 proportional tubes in each layer are glued together to form an annular plane with inner and outer radii of 40 cm and 146 cm. The first twenty tube planes are oriented alternately in four different directions: vertically, horizontally, canted −45°, and canted +45°. The remaining 16 layers alternate between horizontal and

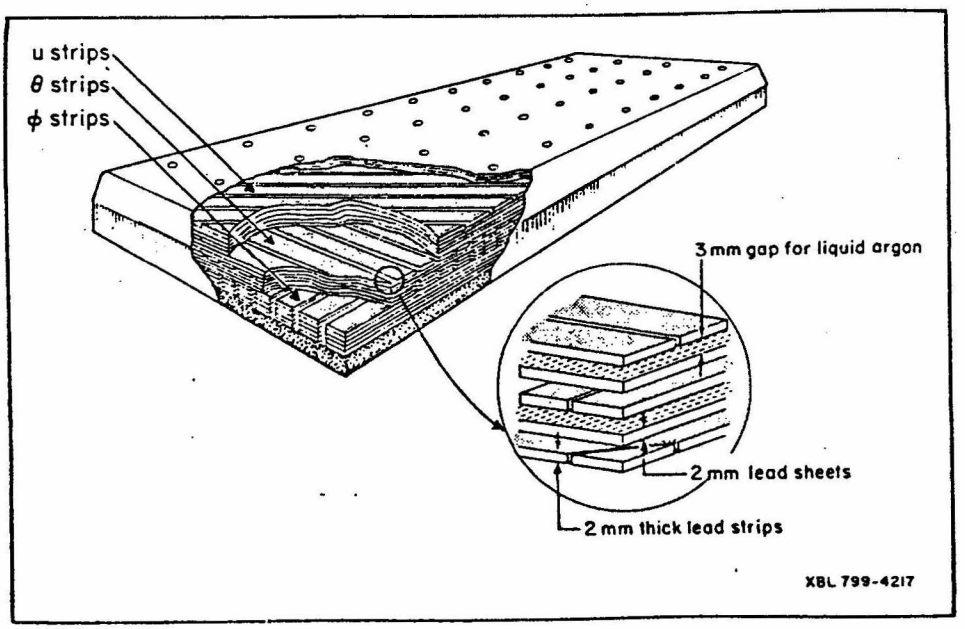

Figure 4.6. Liquid argon calorimeter module construction.

vertical layers. The gas used in the proportional tubes is the same as that used in the drift chamber and is kept just above atmospheric pressure.

A study of Bhabha scattering events in the ECCs at PEP gave an energy resolution of 22% / $\sqrt{E}$ (E in GeV). A minimum-ionizing particle traversing an ECC deposits energy equivalent to a 380 MeV photon. The readout electronics are quiet and sensitive enough to allow this track to be reconstructed in the presence of low backgrounds.

4.2.5 *The muon system*

The MARK II muon system is made up of layers of hadron absorber and proportional tubes mounted on four sides around the central detector. Each wall of the muon system consists of four alternating layers of iron and proportional tubes. The solid angle coverage is 45 % at the outermost layer, and the total number of nuclear interaction lengths (λ) is 7.3. The tubes in the innermost layer are oriented perpendicular to the beam to measure the polar coordinate of the track, while the tubes

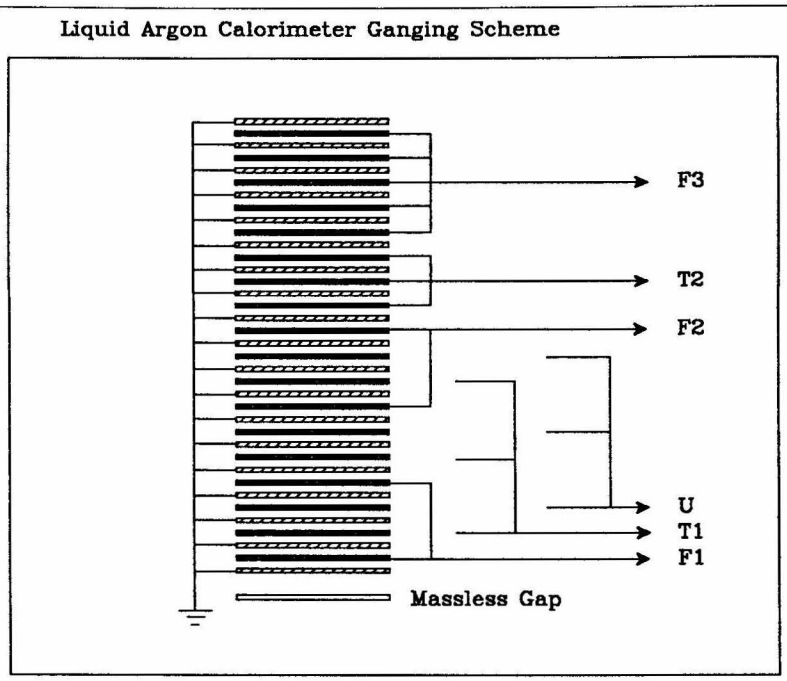

Figure 4.7. Ganging scheme for the layers in the liquid argon barrel calorimeter.

in the outer three layers are oriented parallel to the beam direction to measure the azimuthal coordinate.

Each muon layer consists of extruded aluminum modules made up of eight triangular tubes as illustrated in fig. 4.8. The wire spacing of 2.5 cm was chosen to approximately match the expected multiple-scattering deviation for a particle passing through each layer of absorber. Each tube contains a 45 μm gold plated tungsten wire held at a voltage of 2.0 kV. The gas used in the tubes is a mixture of 95% Ar and 5% CO_2 and is kept at a pressure slightly above atmospheric.

The muon system provides an identification efficiency of typically 85% for incident tracks with momentum greater than 1.8 GeV/c. Below this momentum, all charged particles are expected to range out before the fourth layer, due to dE/dx losses. Chamber inefficiencies vary between 1% and 2 % per plane.

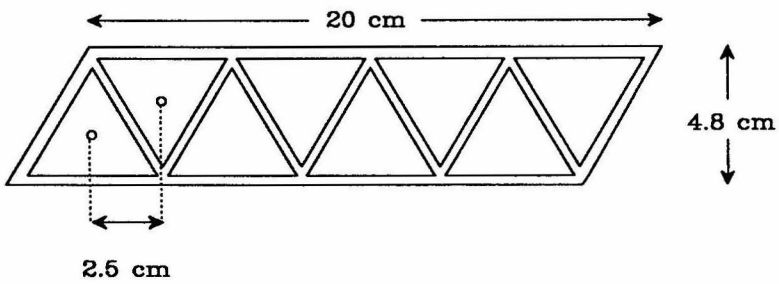

Figure 4.8. Cross-section of a muon tube module.

4.2.6 *Luminosity monitors*

The MARK II has two independent small angle detectors, the Small-Angle Monitor (SAM) and the Mini-Small-Angle Monitor (Mini-SAM). These devices are designed to detect small-angle Bhabha e^+e^- elastic scattering events in order to measure the luminosity of the SLC. The two SAMs cover the angular region between $50 < \theta < 160$ mr at both ends of the detector. Each SAM consists of nine layers of drift tubes for tracking and a six-layer lead-proportional-tube sandwich for measuring the electron energy and position. The expected Bhabha scattering event rate in the SAM is about 4/3 the expected Z boson decay event rate in the MARK II.

The Mini-SAMs cover the angular range between $15.2 < \theta < 25.0$ mr at one end of the detector and $16.2 < \theta < 24.5$ mr at the other. Each Mini-SAM is a 15 radiation length thick tungsten-scintillator sandwich divided into four azimuthal quadrants. The event rate in the Mini-SAM due to Bhabha scattering is approximately 7 times that of the Z event rate in the MARK II.

4.2.7 *The extraction line spectrometers*

The SLC beam energies are measured by a two identical spectrometer systems. The spectrometers are located in the e^+ and e^- beam dumps 150 m downstream on either side of the IP. In fig. 4.9 is shown a conceptual design of the e^- extraction line spectrometer system. Here the e^- beam passes through a series of three dipole

magnets. The first magnet bends the beam horizontally, causing it to emit a horizontal swath of synchrotron light. The second magnet serves as the spectrometer by creating a vertical bend in the beam direction on the order of 18 mr. The third magnet, like the first, bends the beam horizontally, resulting in the emission of another swath of synchrotron light. Phosphorescent screen synchrotron light monitors located a distance x ($\approx$ 15m) downstream from the spectrometer magnet measure the distance d between the swaths ($\approx$ 27cm) and thus the vertical bend angle $\theta \approx d/x$. This same angle can also be expressed in terms of the strength of the magnet ($\int B \cdot dl$) in kG-m and the beam momentum p in GeV/c:

$$\theta = \frac{(\int B \cdot dl)(0.29978)}{p}. \tag{4.2}$$

Substituting $\theta = d/x$ into eqn. 4.2 and rearranging gives

$$p = \frac{(\int B \cdot dl)(0.29978)x}{d}. \tag{4.3}$$

Thus we see that the beam momentum or, equivalently for electrons at SLC energies, the beam energy can be found using this system.

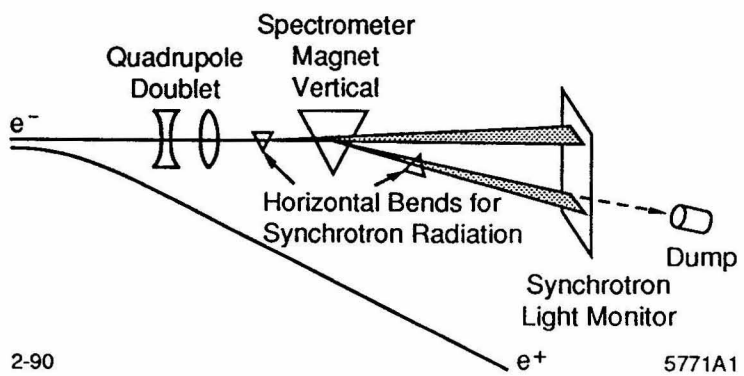

Figure 4.9. Conceptual design of the extraction line spectrometer.

The absolute accuracy of the energy measurement is dependent on the accuracy of the measurements of the magnetic field strength ($\int B \cdot dl$) , the distance x between the spectrometer magnet and the phosphor screens, and the distance d between the swaths. An overall systematic error of 35 MeV on the determination of the absolute center-of-mass energy of the colliding e^+e^- beams is achieved with this system at the SLC.

4.2.8 The trigger

The readout of the MARK II data acquisition system is triggered by either a charged track trigger, a calorimeter energy trigger, or a luminosity monitor trigger. Each trigger system is independent of the others. The maximum beam crossing rate at the SLC is 120 Hz which allows sufficient time to run the trigger logic on every beam crossing. The detector is also triggered on random beam crossings to provide a history of background conditions during the run.

4.2.8.1 Charged particle trigger

The charged particle trigger uses hardware designed to look for tracks in the pattern of hit cells in the drift chamber. No timing or information about the z-coordinate is used. A drift chamber cell is considered "hit" when at least four of the six sense wires have TDC signals. Tracks are formed by hardware modules which search for patterns of hits falling within a specific range of radii of curvature along the first 10 drift chamber layers. At least 8 cells must be hit for the pattern to be considered a track. In order to have the possibility of hitting at least 8 layers, the tracks must be within the angular range $|\cos\theta| < 0.75$. The minimum radii of curvature used correspond to a cutoff of 150 MeV/c in track momentum transverse to the beam line.

The MARK II data acquisition system is triggered if two or more tracks are found. Tracks found within $\sim 10°$ of each other are counted as a single track. The

charged track trigger efficiency is found using a trigger emulation which is run on Monte Carlo simulations of SLC events. The charged track trigger efficiency is found to be 96% for $\mu^+\mu^-$ pairs that hit the TOF system ($|\cos\theta| < 0.7$) and 97% for hadronic Z decays.

4.2.8.2 *Calorimeter energy trigger*

The calorimeter energy trigger uses groups of eight adjacent calorimeter channels (strips in the liquid argon calorimeter; proportional tubes in the endcap) which are summed at the detector. These signals are digitized by ADCs and hits are defined based on a software threshold. Trigger algorithms in a SLAC Scanner Processor (a fancy type of FASTBUS micro-computer) are then used to find "towers" (clusters of energy which point to the e^+e^- interaction point) by using the hits to index a table of precalculated patterns. To reduce noise from other sources, only the energies of hits contributing to towers are included in the trigger energy sum.

The MARK II data acquisition system is triggered for energy sums of greater than 3.3 GeV in the barrel, or greater than 2.2 GeV in the endcap electromagnetic calorimeters. The calorimeter energy sum trigger efficiency is found using a trigger emulation which is run on Monte Carlo simulations of SLC events. The energy trigger efficiency is found to be 95% for hadronic Z decays.

4.2.8.3 *Luminosity trigger*

The luminosity trigger uses information from the SAM and Mini-SAM. A SAM trigger requires 4 GeV in half a module, or 7 GeV in a whole module in both the north and south SAMs. A Mini-SAM trigger requires 20 GeV of energy to be deposited in both the north and south Mini-SAMs.

Chapter 5

The Time-of-Flight System

The time-of-flight (TOF) system is used to provide charged particle identification including the detection of cosmic rays. The time-of-flight of charged particles is measured by detecting signals generated in scintillator slabs located between the central drift chamber and the magnet coil.

5.1 General description of the counters

The TOF system consists of 48 counters forming a barrel of inner radius 152.4 cm, which is outside and coaxial with the central drift chamber. Each counter is 300 cm long and has a trapezoidal cross-section with a smaller width of 19.8 cm. The counters are 4.5 cm thick except for 2 counters bordering $\phi = 0°$ and 2 counters bordering $\phi = 180°$ that are 3.8 cm thick. The addition of 8 structural ribs along the drift chamber body (which are equally spaced in ϕ starting at $\phi = 0°$) required cutting 1.6 cm from the width of the 16 adjacent counters. The counters are cast from a plastic scintillator based on cross-linked polystyrene SCSN-38[66] which was chosen for its high resistance to crazing due to mechanical stress. The mounting system was designed to provide stress-free support. Both ends of the counters are coupled to light guides made from UV light-transmitting acrylic. These guides narrow the width of the counters from the average of 20 cm to 5.3 cm over a length of 43 cm and then extend 84 cm further to bring the light outside the flux return iron. The dimensions of a single TOF counter with light guides is shown in fig. 5.1 An Amperex XP2222

12-stage photomultiplier tube is attached to the end of each light guide with optical coupling provided by a soft Sylguard "cookie" (Sylguard 184 resin and curing agent mixed with Dow Corning 200 Electronic Fluid with the viscosity of 20 cent. stokes.). The phototubes are shielded from stray magnetic fields by concentric cylinders of mu-metal and soft iron. CAMAC controlled LeCroy 4032A high voltage supplies power the voltage dividers in the phototube base. The voltage dividers, shown in fig. 5.2, have been designed to minimize phototube transit time jitter.[67]

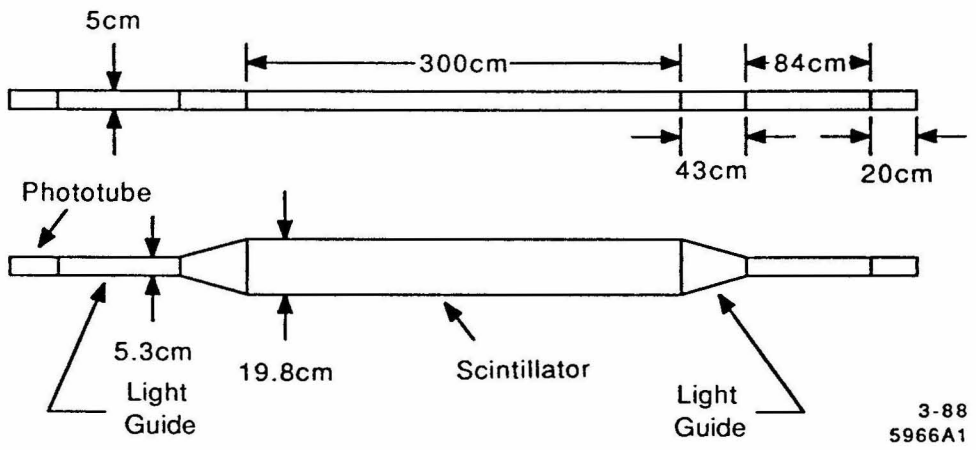

Figure 5.1. Dimensions of a typical TOF counter with light guides and phototubes.

5.2 The electronics

The electronics of the TOF data acquisition system are those used by the pre-upgrade Mark II at PEP.[68] Each phototube channel consists of two independently discriminated Time-to-Amplitude Converters (TACs) and a pulse height integrator as shown in fig. 5.3. The channels are grouped by fours in CAMAC modules called DISCOs (short for discriminator). The data from the four channels are multiplexed onto an analog output as shown in fig. 5.4. The control of the multiplexer is via the

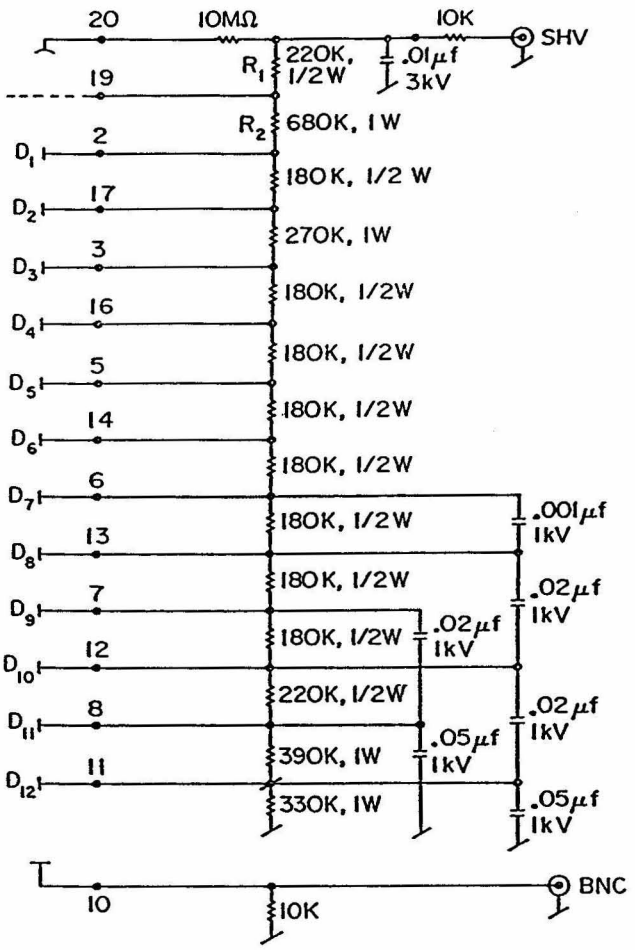

Figure 5.2. The phototube voltage divider used in the MARK II TOF system at SLC. The 12 phototube dynodes are labeled D_i. The numbers just to the left of the dynodes are the XP2222 pinouts.

CAMAC dataway. The voltage thresholds of the timing channel comparators are also received via the dataway. They were set at 180 mV and 400 mV during both the PEP and SLC running. These thresholds correspond to roughly two and four times the expected voltage from a single photoelectron.

The analog times and pulse integrals are collected from the DISCOs via an analog

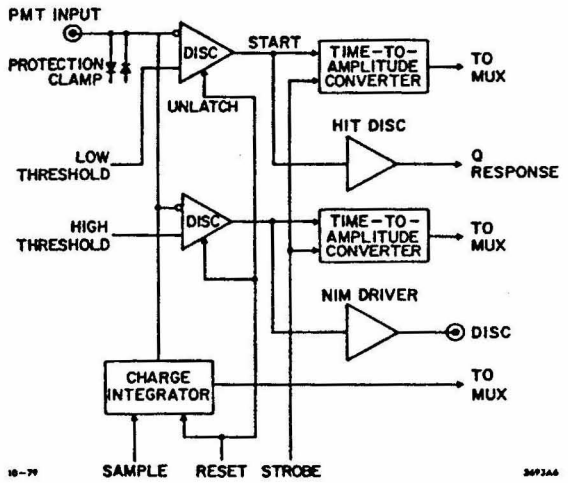

Figure 5.3. A single TOF electronics channel.

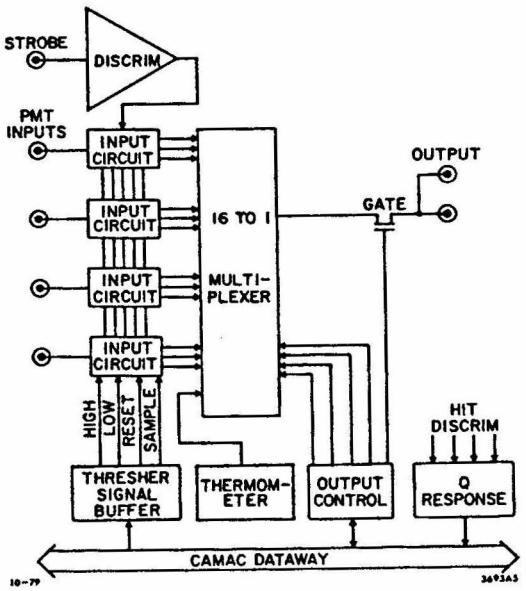

Figure 5.4. The TOF CAMAC DISCO module.

bus, and digitized by a 12 bit ADC incorporated in a 16 bit microprocessor (BADC).[69] The BADC is programmed to perform pedestal subtractions, linear gain corrections, and threshold cuts to the raw digitization of the times and pulse integrals.

The TOF data acquisition electronics are divided into two separate CAMAC

crates. One crate contains all the electronics for the 48 phototubes on the north side of the detector, and another holds the electronics for the south phototubes. Each crate is controlled by a separate BADC.

The timing acceptance window of the TOF timing channels is 60 ns. It is set up in such a way as to provide a maximum time-of-flight of 38.0 ns for a particle originating from the e^+e^- interaction point and traveling to the center of a counter in z. The corresponding time for a particle traveling to the end of a counter in z is 29.4 ns since it takes the light an extra time of $L/2 \cdot 1/v_p$ to reach the far phototube where L=3.0 m is the length of the scintillator and $v_p \simeq 0.17 m/ns$ is the velocity of light in the scintillator. If we assume the production of a stable particle-antiparticle pair at a center-of-mass energy of 93.0 GeV, then we can calculate the expected TOF values for the particles. These values are shown in fig. 5.5 as a function of produced particle mass assuming that the particles travel to either the center or end of a TOF counter in z. From the figure we see that the electronics timing acceptance is long enough for the possible observation of pair produced particles up to nearly half the center-of-mass energy. The timing acceptance before the beam crossing is used to detect cosmic rays which enter the detector before the beam crossing and exit it after the beam crossing. The cosmic rays are rejected in the data analysis based on their characteristic 10 ns flight time from the top to the bottom of the detector.

The TOF timing is started by the signal from a beam pickoff electrode. At the SLC, the electrode is 15 cm long by 2 cm wide and is grounded to the beampipe on the end opposite its feedthrough. It is mounted at a radius of 5 cm from the beam line. The bipolar beam pickoff signal is fed into a SLAC designed constant fraction discriminator module called a One Flavor Box. The One Flavor Box's output time reference pulse is triggered at the zero crossing of the beam pickoff signal. The short term timing jitter of the One Flavor Box is measured to be 30 ps. Its long term timing stability is unknown.

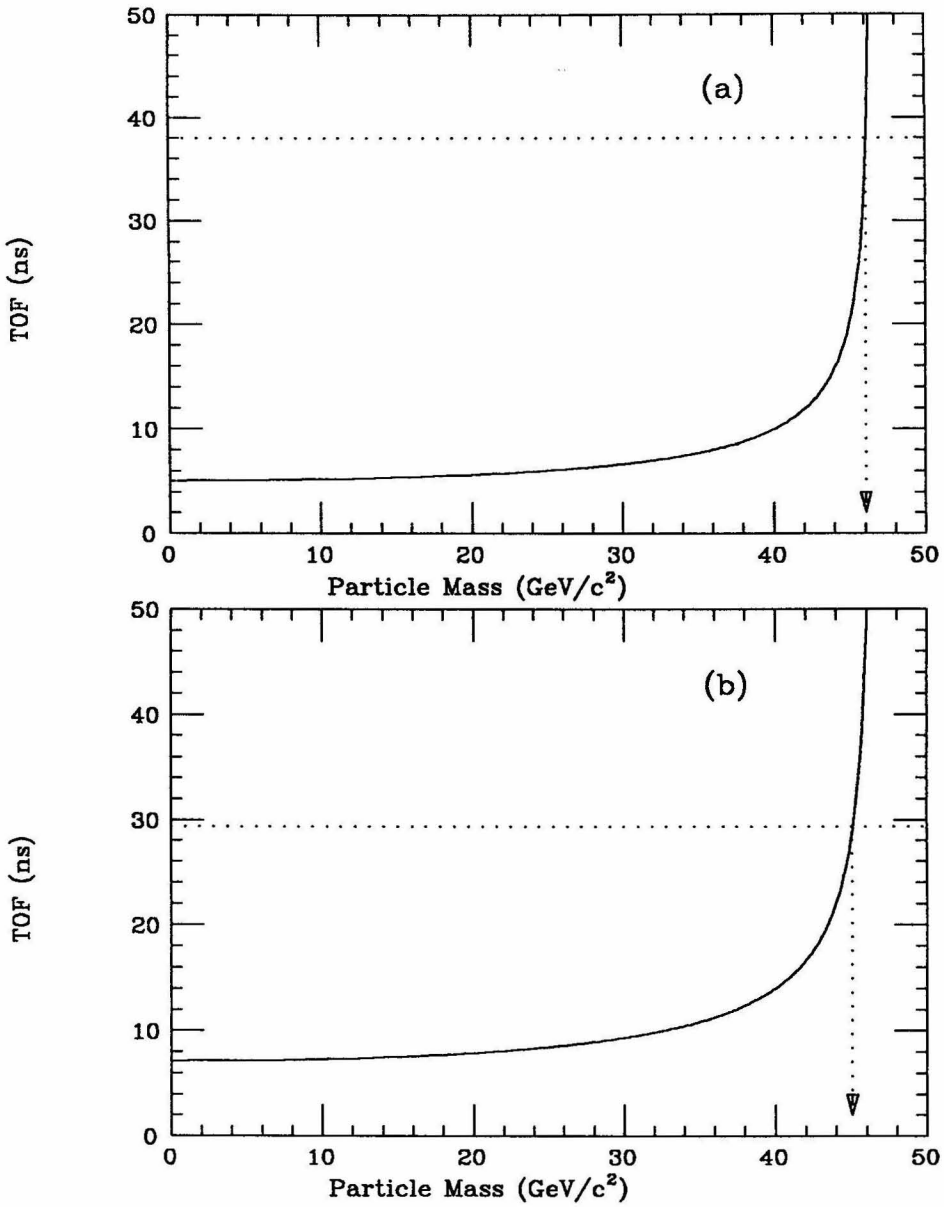

Figure 5.5. The time-of-flight for stable particles at the SLC. Both plots assume the production of a stable particle-antiparticle pair at a center-of-mass energy of 93.0 GeV. Plot (a) gives the calculated TOF as a function of the mass of produced particles traveling to the center of a TOF counter in z. Plot (b) gives the calculated TOF to the end of a counter. The horizontal dotted lines in the plots give the electronics acceptance of 38.0 ns in case (a), and 29.4 ns in case (b). The arrows translate the electronics acceptance into the corresponding mass acceptance of 46 GeV/c^2 in case (a), and 45.5 GeV/c^2 in case (b).

5.3 The calibration systems

There are two independent calibration systems. The calibration of the electronics is carried out using a variable amplitude pulser and delay cables of known length. Calibration constants are computed using a second order fit of channel response to input pulses. These constants provide an accuracy of $\sigma = 60$ ps over a 35 ns interval for the TACs and $\sigma = 70$ pC over a 1700 pC range for the pulse height integrators.

The laser calibration system, illustrated in fig. 5.6, monitors the response of the counters and associated electronics to short light pulses which simulate the effect of the passage of charged particles through the scintillator. A pulsed nitrogen laser illuminates an optical fiber attached to each counter at 90 cm from each end. A CAMAC controlled mirror allows for the illumination of one fiber at a time in a counter, and a set of neutral density filters allows for variation of input light intensity. The timing reference is provided by a photodiode exposed to the laser light; the photodiode also measures the intensity of each pulse. The system provides enough redundant information to monitor the gains of the phototubes, the propagation delays through the scintillator, light guides, cables and electronics, and the attenuation length of the scintillator.

5.4 Data analysis

The measured times from each phototube are corrected for the time that the light takes to propagate through the scintillator and for channel-to-channel propagation delays through the phototube. A time walk correction[70] proportional to the inverse square root of the pulse integral of the phototube signal is also applied. It has been observed that the phototube output signal current saturates at high light levels in the scintillator. Therefore, the measured pulse integral of the signal must be corrected to account for the saturation effect. The functional form of the correction is the same

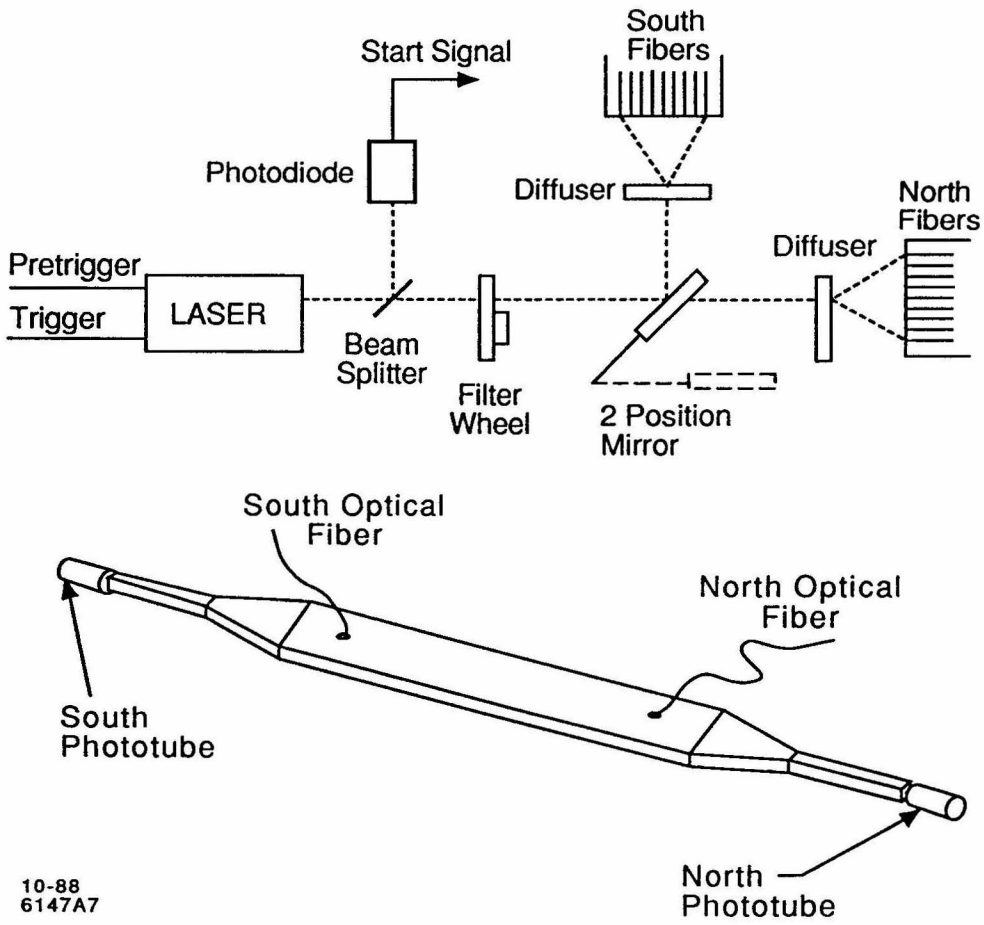

Figure 5.6. TOF laser calibration system

for each phototube

$$Q_{measured} = \frac{B}{2}\left[1 - \exp\left(\frac{-2Q_{actual}}{B}\right)\right] \tag{5.1}$$

where $Q_{measured}$ is the value of the pulse integral and $B = 6577$ is a constant determined using the laser calibration system.

The formula for the corrected phototube time is given by

$$t_i = t_{measured} - \frac{d}{v_p} - t_{delay} - \frac{k}{\sqrt{Q_{actual}}} \tag{5.2}$$

where d is the distance from the end of the scintillator to the track, v_p is the velocity of light in the scintillator ($\simeq$ 0.17 m/ns), and t_{delay} is a measured constant. The time walk constant k is determined for each phototube using the data from the test run at PEP and ranges between 30 and 60. There is not enough data at SLC to check that k has not changed since PEP for any of the phototubes. Studies with SLC data show that the overall TOF resolution does not improve by more than 30 ps for global shifts in k. The error on the resolution determined at SLC is also about 30 ps which tells us that the k values determined at PEP are still valid at the SLC.

A final time of flight t is obtained by taking the weighted average of the times from both phototubes based on their resolutions σ. It is given as

$$t = \frac{\sigma_1^2 t_1 + \sigma_2^2 t_2}{\sigma_1^2 + \sigma_2^2} \tag{5.3}$$

where the resolutions are given by $\sigma_1 = A + Bd_1$ and $\sigma_2 = A + Bd_2$ and d is the distance from the end of the scintillator to the track. The constants A and B are determined from a linear approximation to the distance dependence of the single phototube resolution seen in the data. At PEP the constants were found to be A = 191.55 ps and B = 91.95 ps/m. The ratio of B/A at PEP is 0.4800/m. At the SLC, the values A = 300 ps and B = 144 ps/m retain the value of the ratio B/A found at PEP and describe the data as shown in fig. 5.7. Studies of the SLC data showed that the overall TOF resolution was not improved by more than about 30 ps for changes in the value of the ratio B/A.

Particle mass identification is determined from the velocity $\beta = L/(ct)$, where the path length L from the interaction point is determined from the central drift chamber information and t is the time-of-flight. The squared mass of the particle is

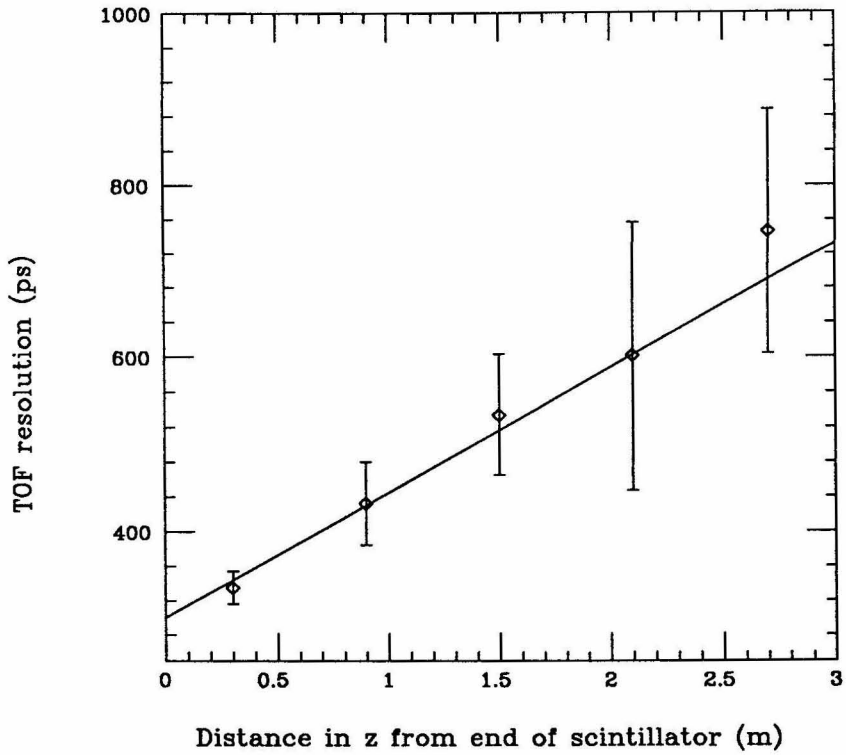

Figure 5.7. The single phototube resolution as a function of the distance d of the charged particle tracks from the end of the scintillator. The error bars indicate the error in the determination of the TOF resolution at that point. The function $f(d) = 300 + 144d$ is drawn as a line through the points.

then given by $m^2 = p^2 \left[1/\beta^2 - 1\right]$ where p is the particle momentum as measured by the drift chamber.

5.5 Performance at PEP

In fig. 5.8 is shown the difference between the time measured by the TOF system and expected time of arrival of electrons from the Bhabha scattering process $e^+e^- \rightarrow e^+e^-$ measured during the PEP test run. The achieved single counter resolution varied from 180 to 250 ps and averaged over all counters and all data runs was 221 ps. This gives the π/K/p separation shown in fig. 5.9.

5.6 Performance at SLC

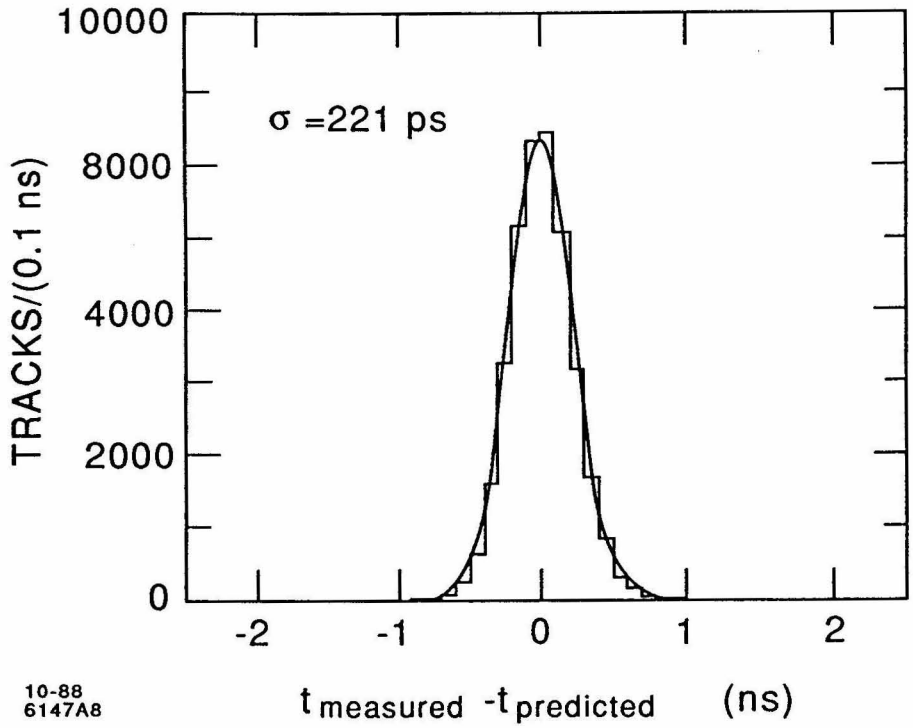

Figure 5.8. TOF resolution for Bhabha scattering events at PEP.

The TOF measurement errors at the SLC are non-Gaussian, as significant accelerator backgrounds contribute to early measured times. This analysis uses a parameterization of the TOF measurement error distribution with the function

$$f(t) \propto \begin{cases} \exp\left(-\frac{1}{2}\left(\frac{\mu-t}{\sigma}\right)^2\right) & t \geq t' \quad ; \\ \exp\left(-\frac{b^2}{2}\right)\left(\frac{a}{b}\right)^a \left(\frac{\sigma}{\mu-t+\sigma(\frac{a}{b}-b)}\right)^a & t < t' \quad , \end{cases} \tag{5.4}$$

where $t = TOF_{\text{measured}} - TOF_{\text{expected}}$, $t' = \mu - b\sigma$ and the parameters $\mu = -11$ ps, $\sigma = 426$ ps, $a = 17.3$ and $b = 0.83$ are determined from the data. This function, constructed so as to be smooth and continuous, is a Gaussian distribution with an extended tail at early times. A fit of this function that includes both high momentum tracks ($\beta \simeq 1$) and minimum ionizing pions identified by the momentum, and dE/dx

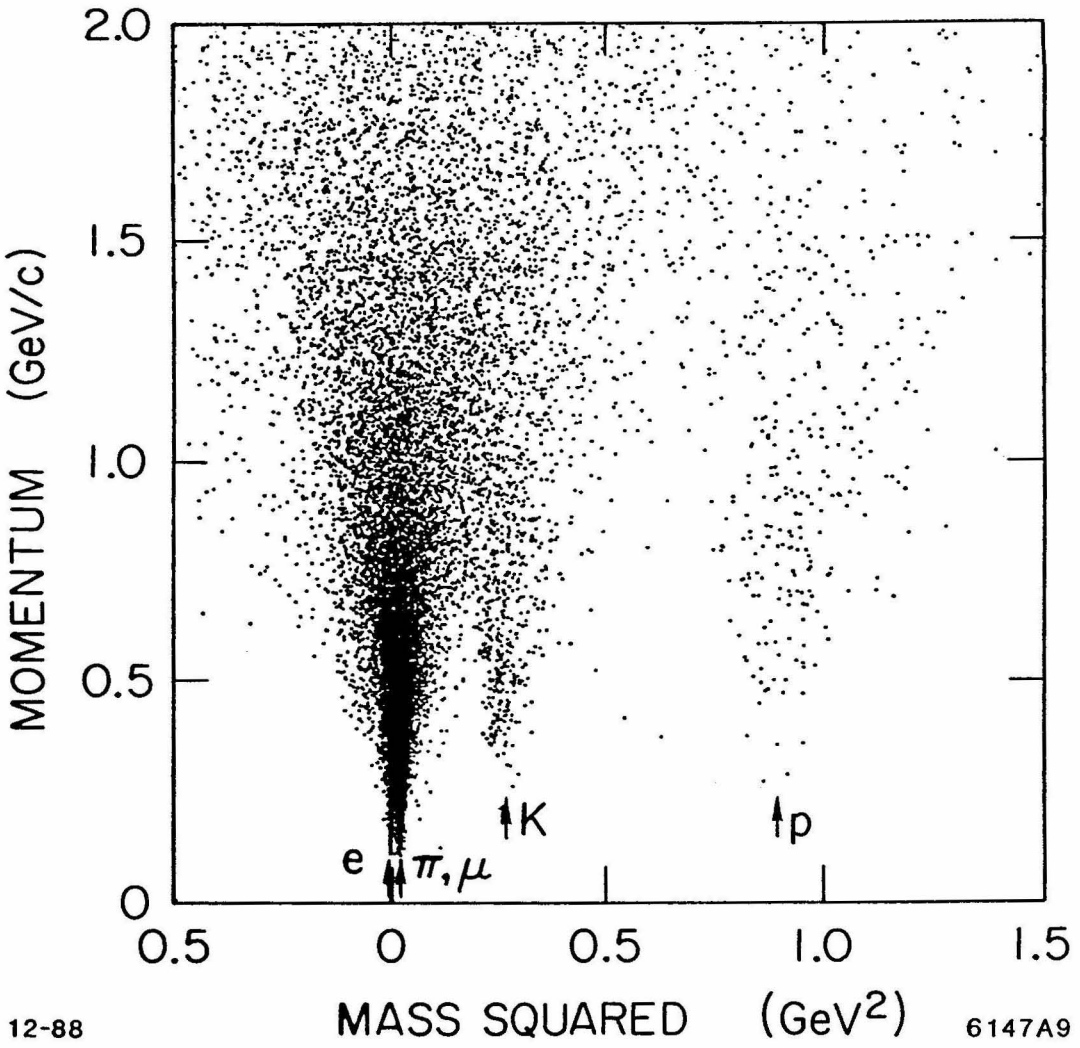

Figure 5.9. TOF particle identification showing pion/kaon/proton separation. The data are from PEP.

measurements is shown in fig. 5.10. The dE/dx values for the data shown in the figure are shown in fig. 5.11. As a cross check, the resulting function is used to generate the Monte Carlo TOF times for electron and muon pairs and, as shown in fig. 5.12, they agree with the data. Fits were also made for the single phototube resolutions for the north and south ends of the system. The parameters found for the north phototubes

as a group are: $\mu = -3$ ps, $\sigma = 520$ ps, $a = 10.0$ and $b = 0.813$, and for the south tubes the parameters are: $\mu = -12$ ps, $\sigma = 493$ ps, $a = 12.0$ and $b = 0.775$. The fits are shown in fig. 5.13. The timing offset between the two sides, given by the difference in their values of μ, is 9 ps. This small offset, together with the comparable general features of timing distributions, shows that there are no major timing differences between the north and south crates of TOF timing electronics.

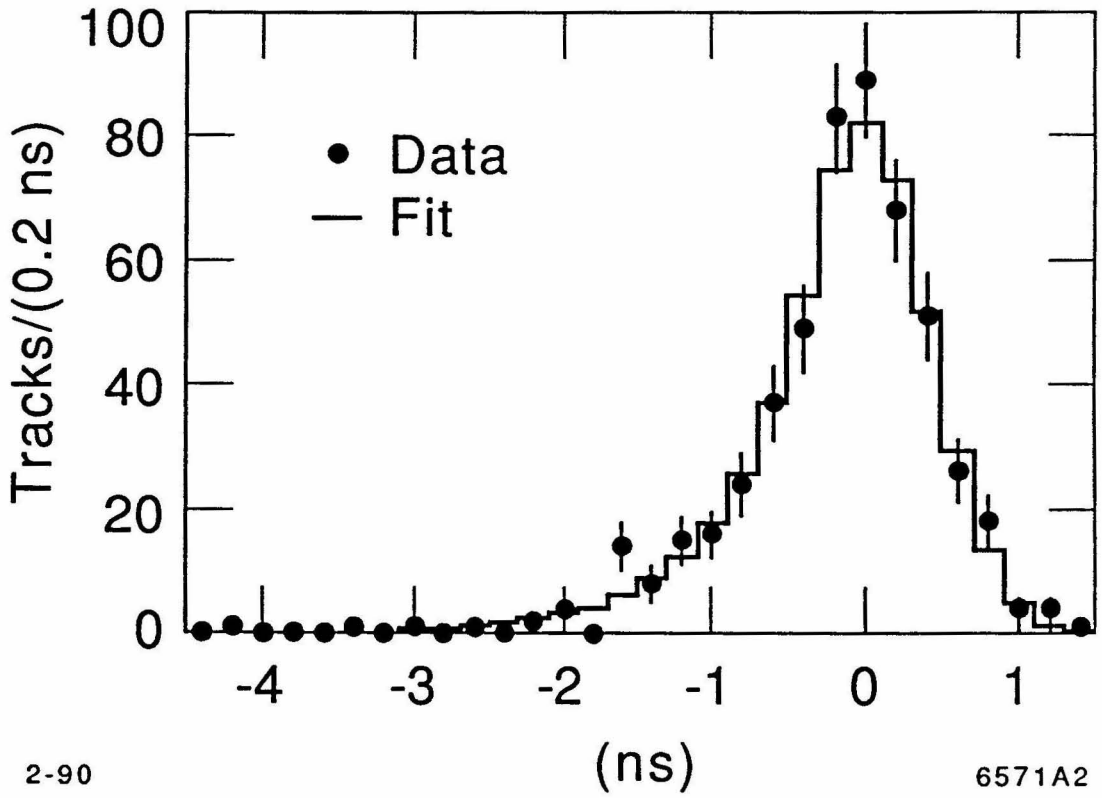

Figure 5.10. Fits of the function $f(t)$ to the error in the TOF measurement for minimum ionizing pions and $\beta \simeq 1$ tracks from the SLC data.

The efficiency of the TOF system was determined from all single tracks from Z decays at SLC which hit the active region of the counters. In fig. 5.14 is shown the dependence of this efficiency on the track position along the counter. Averaging over

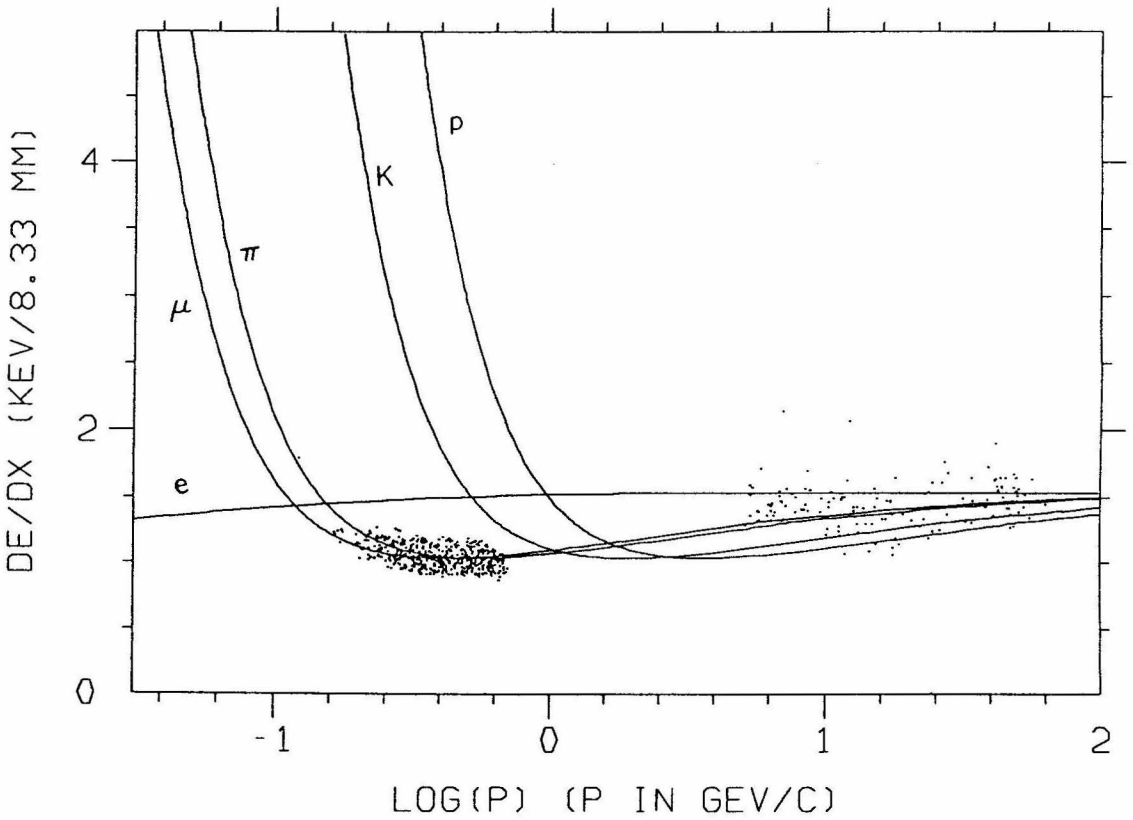

Figure 5.11. The dE/dx values for the minimum ionizing pions and $\beta \simeq 1$ tracks from the SLC data used to determine the parameters of eqn. 5.4 and as shown in fig. 5.10.

the position dependence yields an efficiency of 89.5% for both phototubes to fire and an efficiency of 96.8% for at least one tube to fire if a counter is hit by a charged track. These average efficiencies are dependent on the amount of light left in the counters. They drop by about 1% if they are determined from minimum ionizing pion tracks

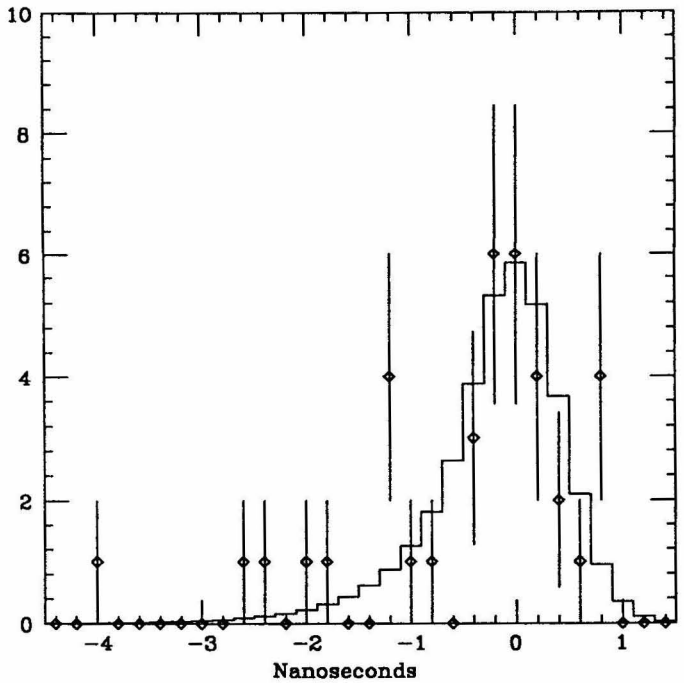

Figure 5.12. TOF resolution for e^+e^- and $\mu^+\mu^-$ pairs at the SLC. The data are shown as points and the Monte Carlo simulation is shown as a histogram.

only. The average efficiencies rise by about 3% if only tracks on the relativistic rise in dE/dx are used.

The observed TOF resolution is worse at SLC than at PEP. This can be explained by a combination of the following factors: First, the TOF resolution at PEP was determined from Bhabha scattering events, whereas, at SLC it is dominated by contributions from minimum ionizing pions which have lower light yield in the scintillator and thus are affected by the photoelectron statistics in the phototubes. Next, the addition of the background signals to the phototube signals can cause the timing threshold to be exceeded too early. The addition of background also invalidates our pulse height correction which was developed in a clean environment. To minimize these background effects at the SLC, the gain of the photomultipliers was lowered while the timing start threshold voltage remained constant. This is known to degrade the timing resolution. Finally, because the beam pickoff system used at PEP

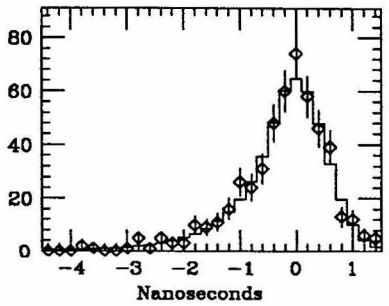

North Phototubes

DATA POINTS	FIT HISTOGRAM	
WTS 509	CHIS	18.45
UND 1	N	64.630
OVE 11	μ	−0.003
MIN−5.8742	σ	0.520
MAX 7.5549	a	10.009
AV −.249	b	0.813
RMS .82253		

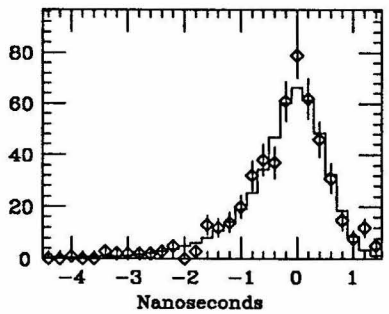

South Phototubes

DATA POINTS	FIT HISTOGRAM	
WTS 508	CHIS	26.86
UND 2	N	66.159
OVE 11	μ	0.012
MIN−7.6092	σ	0.493
MAX 9.3962	a	12.009
AV −.23178	b	0.775
RMS .82938		

Figure 5.13. Fits of the function $f(t)$ to the error in the TOF measurement for minimum ionizing pions and $\beta \simeq 1$ tracks from the SLC data for the north and south phototubes alone.

was designed for the stable beam intensity conditions of a storage ring we had to install a more robust system at the SLC. The absolute contribution of this system to the TOF measurement error is not known.

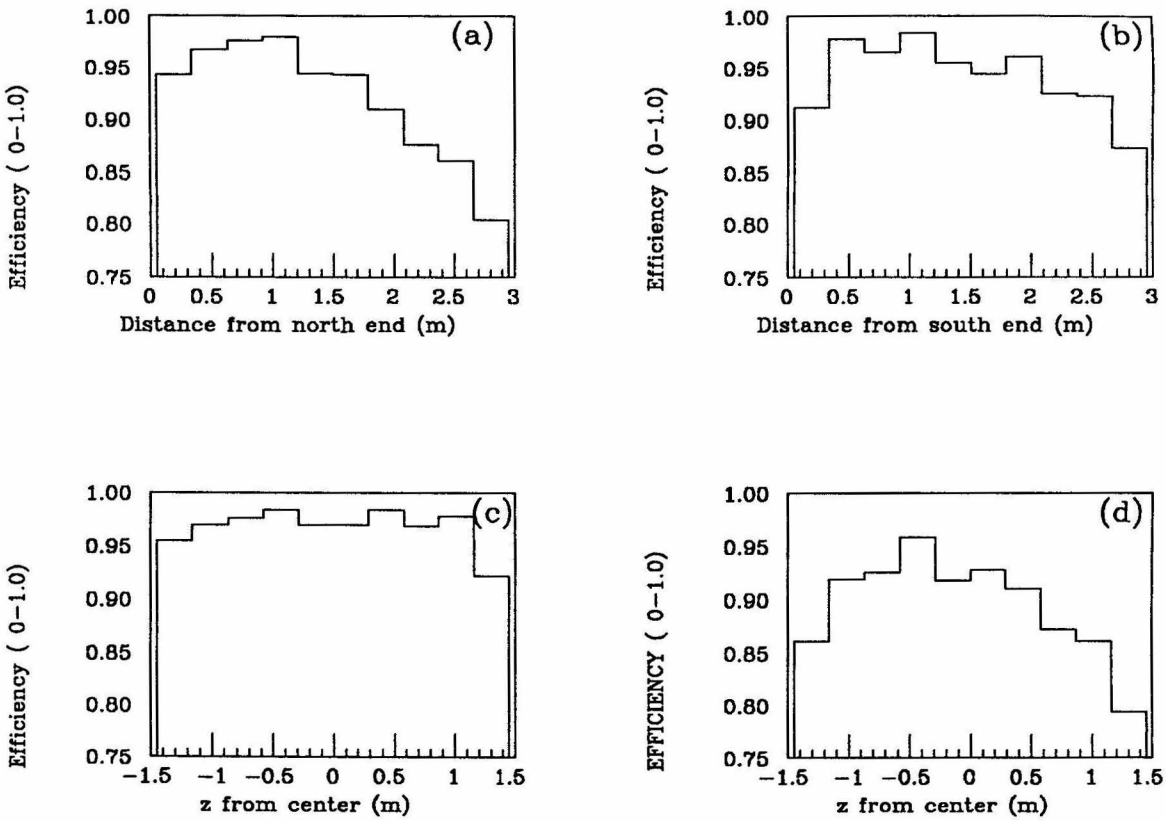

Figure 5.14. The TOF efficiency at SLC. In plot (a) is shown the efficiency of the north tubes as a function of track distance from the end of the counter. The same distribution for the south phototubes is shown in plot (b). In plot (c) is shown the efficiency for at least one of the phototubes on a hit counter to fire and in plot (d) is shown the efficiency for both tubes to fire.

6.1 The data sample

The data sample from which candidate events will be selected consists of some 5.7 million MARK II triggers written to tape during the e^+e^- colliding beam run at the SLC from May 20, 1989 through October 16, 1989. This data sample corresponds to an integrated luminosity of 19.7 nb^{-1}. The data were collected at several center-of-mass energies in the range $89.2 \leq E_{cm} \leq 93.0$ GeV as listed in Table 6.1 and constitute an energy scan of the Z boson resonance.

Table 6.1. Integrated luminosity at each energy scan point for the 1989 data run.

Energy Scan Point (GeV)	Luminosity (nb^{-1})
89.2	0.68
90.0	0.76
90.4	2.61
90.7	1.21
91.1	4.08
91.4	4.12
91.5	1.23
92.2	3.59
92.6	0.40
93.0	1.00
Totals	19.7

In a data sample of this size collected at the energies listed in Table 6.1 we would expect, accounting for detector acceptance and radiative corrections, on the order of 500 Z boson decays, 800 SAM Bhabha and 4500 Mini-SAM Bhabha scattering events. These numbers clearly do not begin to account for the 5.7 million triggers recorded during the run. Rather, the large number of triggers result from several background processes which trigger the MARK II.

6.1.1 The data acquisition trigger

The MARK II data acquisition system is triggered by two or more charged tracks with $|\cos\theta| < 0.75$, or by an electromagnetic shower with localized energy deposition greater than 3.3 GeV in the barrel, or greater than 2.2 GeV in the endcap electromagnetic calorimeters, or by a SAM or Mini-SAM luminosity trigger. The details of these trigger systems can be found in Chapter 4.2.8. We will now discuss the general characteristics of both signal and background events in terms of these trigger requirements. We limit the following discussion to the charged track and energy triggers.

6.1.2 Characteristics of events of interest

We are interested in selecting from the data two specific Z boson decay final states. These final states have quite different topologies. We will first describe the characteristics of stable charged particle pair production events that are the candidate events in our new particle search. We will then describe the characteristics of the hadronic events to be selected for the normalization of the data sample size.

6.1.2.1 Stable charged particle pair production events

Stable charged particles can be produced at the SLC in the decay of a Z boson at rest at the e^+e^- interaction point to a particle-antiparticle pair with equal mass. Since momentum and energy are conserved in the decay, we know that the final state particles must travel in opposite directions with equal velocity. Here we are assuming the term "stable" to mean that the particle lifetimes are long enough for them to travel through the central drift chamber, TOF, and calorimeter systems of the MARK II detector. This corresponds to lifetimes on the order of 10^{-10} seconds for particles which are produced in pairs in Z decay with masses around 1 GeV/c^2, and 10^{-8} seconds for 40 GeV/c^2 particle masses. A $\mu^+\mu^-$ event which is typical of the stable charged pair production topology is shown in fig. 6.1.

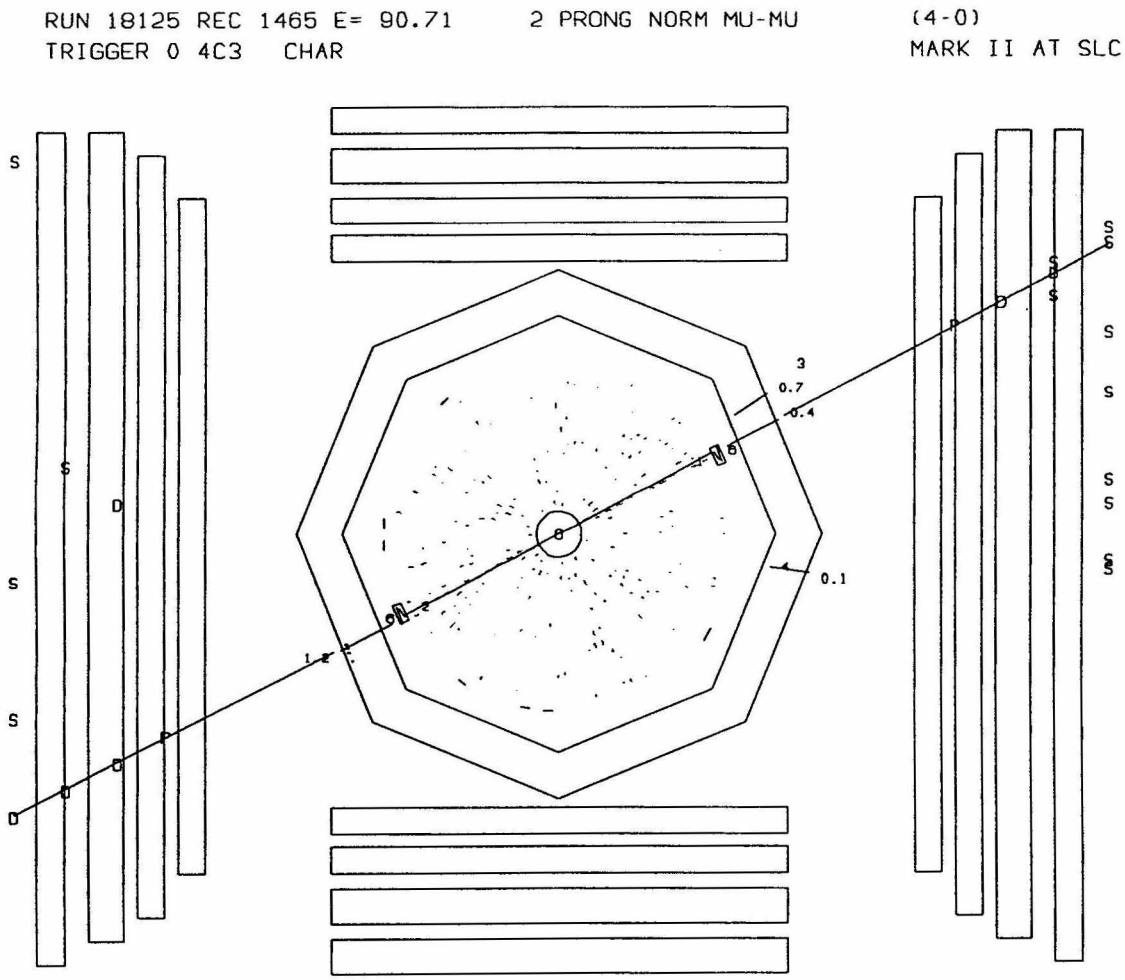

Figure 6.1. A typical $\mu^+\mu^-$ event recorded by the MARK II detector at SLC.

In this analysis we will only consider candidate stable charged pair production events in which the particles are tracked by the drift chamber and hit the time-of-flight scintillators. This limits the tracks in candidate events to the angular range $|\cos\theta| < 0.70$. The trigger efficiency for the candidate is then theoretically 100%. However, due to problems with the trigger hardware, the trigger efficiency is actually

96% for these events.

6.1.2.2 Hadronic events

The most probable decay of the Z boson is to a quark-antiquark pair. The Z's in our experiment are produced at rest at the e^+e^- interaction point and thus the quarks have equal and opposite momenta. As they start to leave the production point, they undergo the fragmentation process, forming jets of hadrons as described in Chapter 4. Some of these hadrons are long-lived and travel through a significant portion of the detector volume. Others decay into photons or decay, sometimes semi-leptonically, producing neutral and charged leptons and other hadrons. The mean charged particle multiplicity in hadronic events is expected to be over 20 at SLC energies. This expectation is based on Monte Carlo models which were developed using data from lower energy accelerators and extrapolated[56] to SLC energies. A typical hadronic event is shown in fig. 6.2.

Monte Carlo simulations indicate that 99.8% of hadronic Z decays will satisfy at least one of either the charged particle or calorimeter energy triggers. This number includes the effects introduced by problems with the trigger hardware.

6.1.3 Backgrounds

The dominant backgrounds which trigger the detector are related to the SLC accelerator beams, but some cosmic ray and two photon interaction events are also found in the data.

6.1.3.1 Beam halo interactions

One background source which can satisfy the trigger requirements comes from particles in the tail or halo of the beams, i.e., particles with slightly different momentum than the beam which nevertheless are transmitted through the magnets. The halo particles can interact with the accelerator structure in the final focus area and send secondary particles, mostly muons, into the detector. These secondary particles

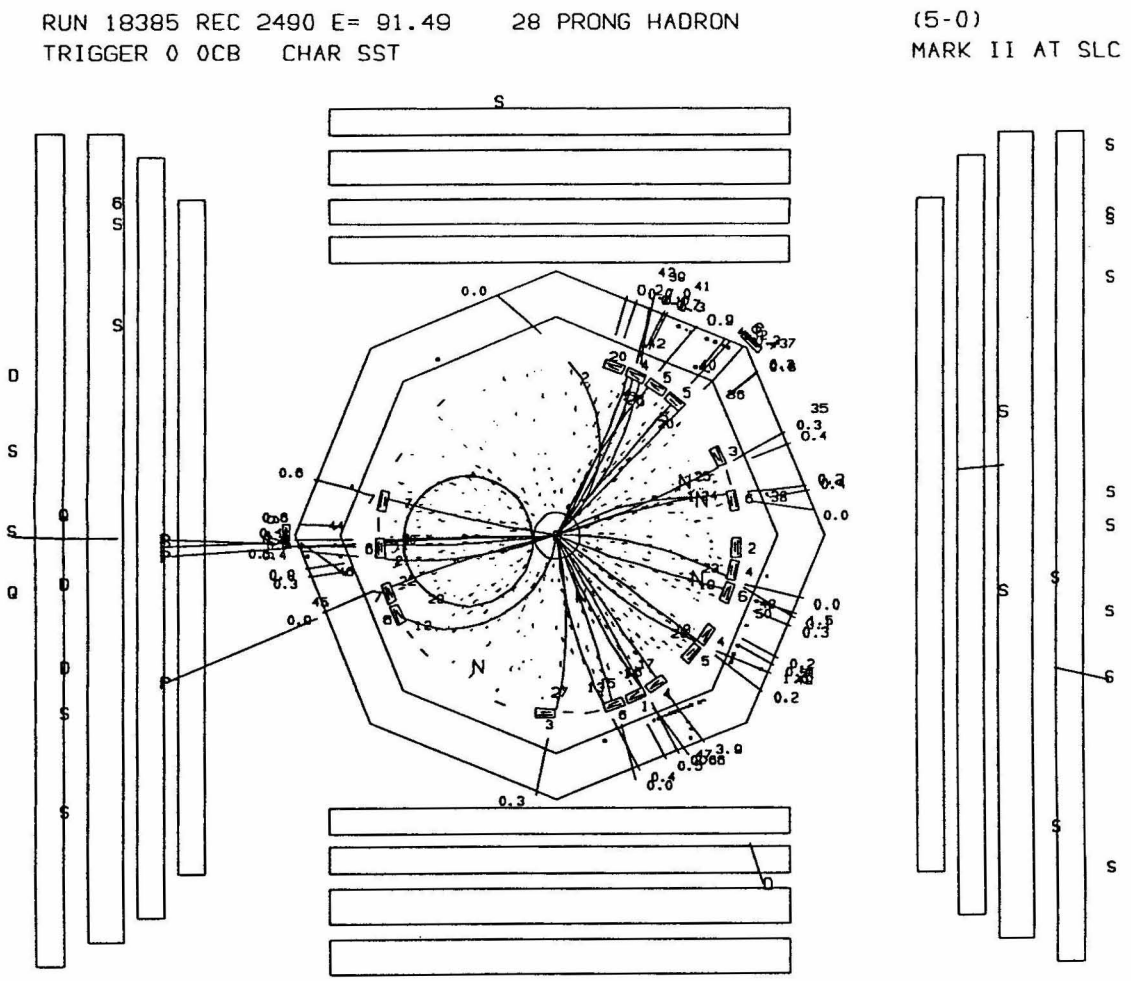

Figure 6.2. A typical hadronic event recorded by the MARK II detector at SLC.

can generate tracks and deposit energy in the detector and thus satisfy one or more of the trigger requirements. The tracks of the secondary particles do not originate at the e^+e^- interaction point as do tracks from Z decays. Rather, they traverse the detector from end to end in z.

This source of background triggers was extensively studied during the course

of the run and measures to reduce its impact on the experiment were implemented. One such measure involved collimating the beams more thoroughly upstream of the final focus and detector areas to reduce the number of halo particles which interact with the accelerator structure. The other involved the installation of toroidal spoiler magnets in the final focus area which were able to deflect the secondary muons away from the MARK II detector.

6.1.3.2 *Synchrotron radiation*

A second accelerator related background arises from synchrotron radiation which is generated as the beams pass through the magnets of the final focus system and are steered into collision. This radiation is able to ionize the drift chamber gas and simulate hits on the sense wires. If enough such simulated hits are generated, it becomes possible for the trigger hardware to form tracks through them and satisfy the charged trigger criteria. When these tracks are reconstructed in the offline analysis they are found to originate at arbitrary points along the beam line rather than from the e^+e^- interaction point as in Z decay. This background source was very sensitive to the details of the beam steering through the magnets and was continuously minimized during the run by tweaking the beam orbit and focusing parameters of the final focus system in order to find a relatively quiet operating point.

6.1.3.3 *Beam-gas interactions*

Finally, interactions of beam particles with the residual gas inside the beampipe produce secondary particles which can travel through the detector as tracks and can deposit energy in the calorimeters. Unlike Z decay events, the beam-gas interactions originate with equal probability at any point in z along the beam line. Also, the secondary particles from beam-gas interactions tend to travel in the same direction as the incoming beam particle so that they and their energy appears in only one of the forward or backward hemispheres of the detector.

6.1.3.4 Two photon interactions

The two photon interactions, shown in fig. 6.3, can trigger the detector and serve as background to hadronic or stable charged particle pair production events. The cross-sections for these events can be calculated and have been used in Monte Carlo simulations[71] of these processes at SLC energies. The simulations show that two photon events tend to deposit little energy in the detector as the initial state electron and positron which carry most of the energy tend to be scattered at small angles and are lost down the beam pipe. In addition, the fermion-antifermion pairs produced in the two photon interactions tend to deposit energy in either the forward or backward direction in z but not both as is usually the case in Z decays.

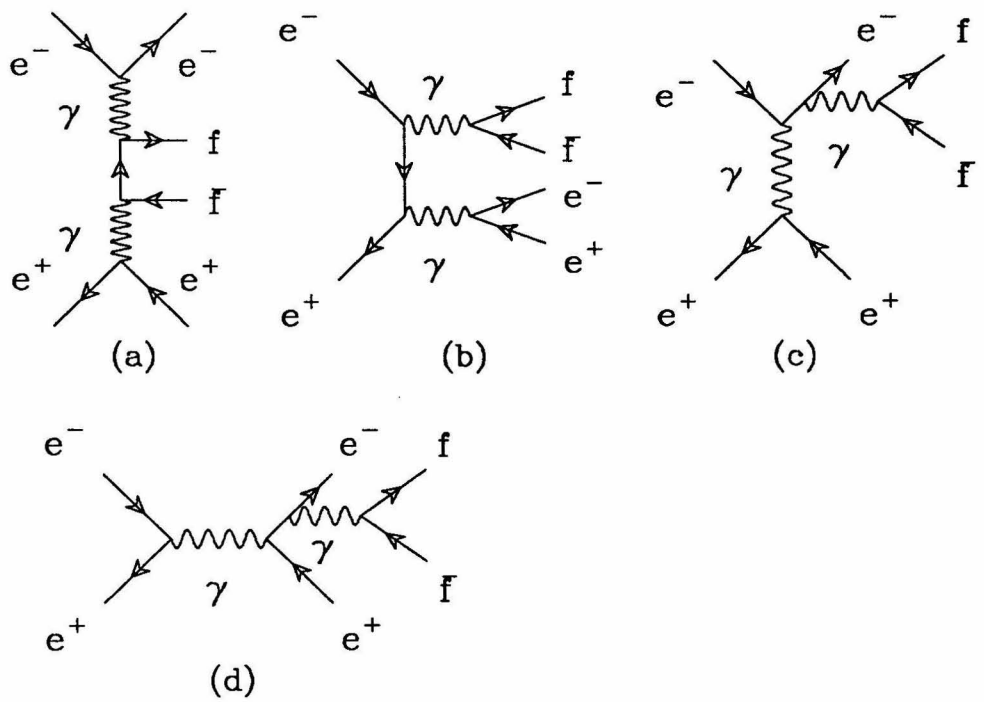

Figure 6.3. Two photon event classes, (a) multi-peripheral, (b) conversion, (c) bremsstrahlung and (d) annihilation.

6.1.3.5 Cosmic rays

Cosmic ray muons which pass through the detector in time with an SLC beam

crossing can simulate two colinear tracks. To satisfy the charged particle trigger, a cosmic ray must pass through only 8 of the 10 innermost layers of the drift chamber both on the way into and out of the detector. Therefore, the cosmic rays are only constrained to pass through a cylindrical volume centered at the e^+e^- interaction point of $|z| < 2.3$ m (the length of the drift chamber) and $r = \sqrt{x^2 + y^2} < 40$ cm, which is the approximate distance from the IP to the third drift chamber layer. This allows them to be distinguished from Z decays in which the tracks originate much closer to the e^+e^- interactions point.

Cosmic rays can also be identified if one or both of the TOF times recorded as the cosmic ray enters and leaves the drift chamber is earlier than is possible for a particle with velocity $\beta = 1$ produced in Z decay. Also the difference in the TOF times for cosmic rays is expected to be on the order of 10 ns which is the time it takes a $\beta = 1$ particle to traverse the drift chamber. This allows us to distinguish cosmic rays from stable particle pair events in which the particles both travel to the TOF scintillators in equal times.

6.1.4 *Initial data reduction procedure*

The idea behind the initial data reduction is to remove as many background events as possible from our 5.7 million total event sample without removing any of the Z decay events of interest. The procedure consists of removing triggered events which do not satisfy at least one of the following criteria: 3 or more tracks reconstructed in the drift chamber originating near the e^+e^- interaction point (IP), 2 tracks from a common vertex near the IP, a shower in one of the calorimeters of greater than 12% of the center-of-mass energy or two back-to-back showers of at least $6\%E_{\rm cm}$ each. In addition, all events with only a luminosity trigger are removed.

Following the above procedure reduces the data sample from 5.7 million to 20,576 events by removing most of the cosmic ray, beam-gas and accelerator related background events in which the tracks do not originate at the IP. Clearly this sample

still contains more events than the 500 or so Z decays expected. Therefore, we must develop further criteria if we want to select out events due to Z decays. For the case of the pair production of stable charged particles in Z decay, this will require searching for events with two tracks in the detector which originate at the e^+e^- interaction point, which are back-to-back and which have equal masses and momenta. This selection will be developed in detail later in section 6.3 after we first discuss the hadronic event selection procedure.

6.2 Hadronic event selection procedure

We now discuss the procedure used to select hadronic events from other Z decays and the background remaining in our reduced data sample. This procedure consists of applying to each event a series of tests which are easily passed by hadronic events but which are failed by other Z decays and by background events. We will show that keeping only those events which pass all the tests leaves us with a pure sample of hadronic Z decay events.

6.2.1 Requirements on reconstructed tracks

Because of their expected high charged particle multiplicity, it is possible to require that hadronic event candidates have at least three well measured tracks coming from the interaction point. The tracks have to fulfill several criteria before they are considered in the above selection. These criteria are:

- The charged tracks are required to emerge with transverse momenta greater than 110 MeV/c.
- The tracks are required to have $|\cos\theta| < 0.92$.
- The tracks are required to come from the e^+e^- interaction point defined by a cylindrical volume of radius $r = \sqrt{x^2 + y^2} = 1$ cm and half-length $|z| = 3$ cm parallel to the beam line.

The minimum momentum requirement is imposed since below 110 GeV/c, a track will be bent so strongly in the magnetic field as to not pass through all 12 cell layers

of the drift chamber. The requirement on the polar angle θ of the track just defines the active volume of the drift chamber. The requirement on the distance of closest approach of the tracks to the e^+e^- interaction point in r and z is included to reduce the probability of accepting beam-gas or cosmic ray events which do not usually originate at the e^+e^- interaction point. This requirement is loose enough to take into account the uncertainty in the location of the e^+e^- interaction point* and also the 170 μm position resolution of the drift chamber track reconstruction. Shown in fig. 6.4 (a) and (b) are the distances of closest approach r and z for all tracks found in the 20,576 events of the reduced data sample. Also shown in fig. 6.4(c) and (d) are the same distributions for Z decays to e^+e^- and $\mu^+\mu^-$ events selected from the data different procedures to be described later. The data in plots (c) and (d) are included to show that the requirements on r and z are loose enough to include tracks known to come from Z decays. We can infer from fig. 6.4(c) and (d) that the peaks in plots (a) and (b) are due to tracks from Z decays.

6.2.2 *Visible energy requirement*

Next, a requirement is imposed on the distribution of visible energy in the event. This requirement is designed to eliminate two photon and beam-gas events, which usually have small amounts of visible energy compared to the center-of-mass energy and also tend to have all their visible energy in only one hemisphere of the detector. We will now define the term visible energy and show that requiring it to be at least 0.05% of the center-of-mass energy in each of the forward and backward hemispheres of the detector is sufficient to remove all two photon and beam-gas background events in the data while retaining 95% of the hadronic events.

The visible energy is defined to be the sum of both the charged particle momenta and the energy deposited in the barrel and endcap electromagnetic calorimeters by

* Typical SLC beam sizes during the run were $\sigma_r \approx 4.0\mu$m and $\sigma_z \approx 1.0$ mm. The uncertainty in the e^+e^- interaction point determined from SLC accelerator tests is 200 μm in r and 1 mm in z.

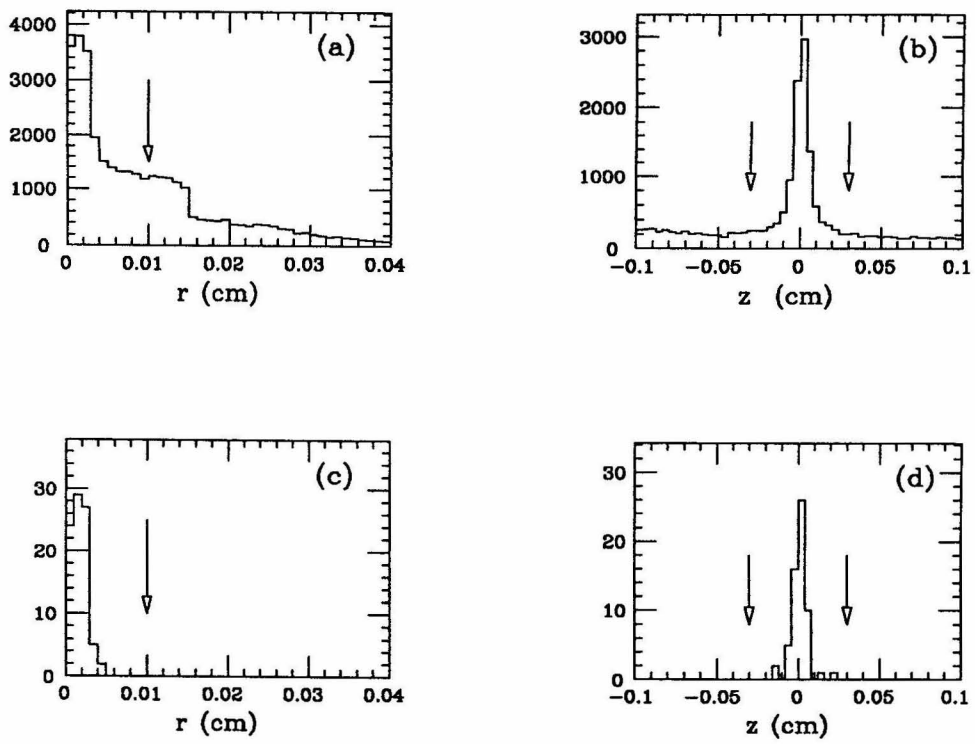

Figure 6.4. Distance of closest approach for tracks in r and z. The cuts described in the text are shown as arrows in the figure. In figure (a) is plotted the distribution of r for all tracks from the reduced data sample reported in the text while in figure (b) the distribution of z for all tracks is plotted. In figures (c) and (d) are shown the same distributions for Z decays to e^+e^- and $\mu^+\mu^-$ pairs found in the same data set.

either charged particles or photons. For an electromagnetic shower to contribute to the visible energy as a photon, we require that it be at least 1 GeV. This is to reduce the possibility that the shower was caused by electronic noise or by low energy accelerator backgrounds. The distribution of the energy of showers due to these sources is shown in fig. 6.5. The data in the plot were obtained from 10,881

events sampled on random e^+e^- beam crossings throughout the period of the data collection run, i.e., at arbitrary beam crossings, the data acquisition is started whether or not there is a valid trigger. Typically, none of the charged track, total energy, or luminosity triggers are satisfied in these random events. The signals readout for the detector subsystems on random events are taken to be representative of the electronic noise or low energy accelerator backgrounds signals present at every beam crossing. As shown in fig. 6.5, the number of showers in the random events drops off dramatically above 1 GeV, which is taken as the minimum energy for a shower to be included in the visible energy sum.

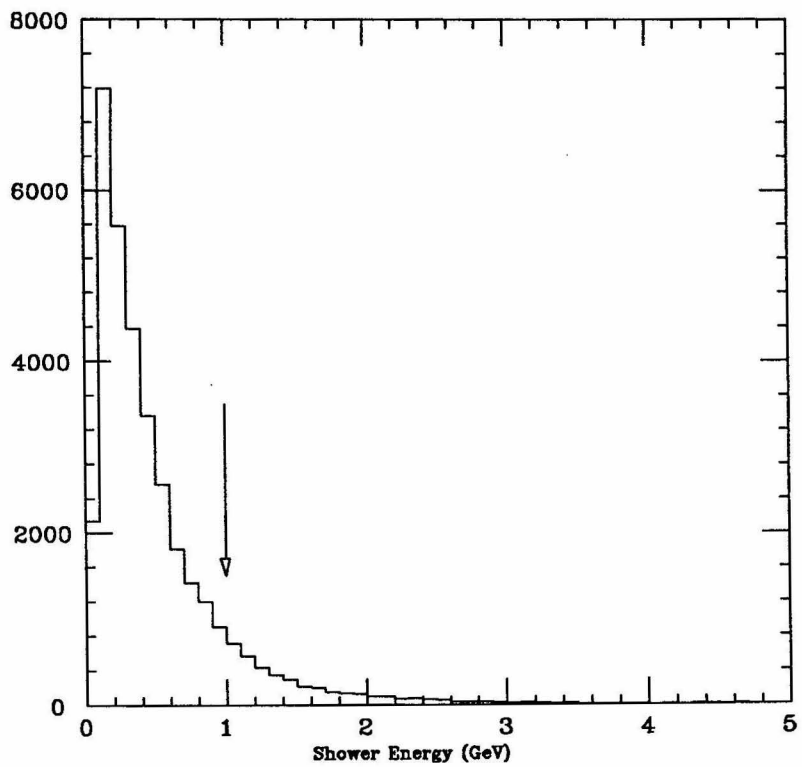

Figure 6.5. The calorimeter energy in 10,881 events sampled at random e^+e^- beam crossings throughout the data run. The data in this plot represents the noise in the calorimeters due to the electronics and also beam related backgrounds. The cut at 1 GeV on the energy required for showers to contribute to the visible energy sums in hadronic events is shown by an arrow.

Shown in fig. 6.6 is the distribution of visible energy in the forward hemisphere, $E_{forward}$, versus the energy in the backward hemisphere, $E_{backward}$ in units of $E_{\rm cm}$ for a Monte Carlo simulation[71] of two photon events representing 100 times the integrated luminosity of our data sample. Two events are seen to pass the cuts at $0.05E_{\rm cm}$ in each hemisphere which implies that we would expect a negligible 0.06 two photon events in our data sample to pass this cut. In fig. 6.7 is shown the minimum of the visible energy in either the forward or the backward hemispheres for the same sample of two photon events. It is clear from this figure that we can not lower the value of the visible energy requirement without introducing a sizable background from this source.

The the requirement on visible energy also eliminates background from beam-gas interactions. This background was studied by looking at events which pass the hadronic selection but with the requirement on the distance of closest approach of tracks in z changed to $3 < |z| < 50$ cm to insure that no hadronic Z decays are selected. No events were selected from our data in this case. This corresponds to an upper limit of 3.0 events at the 95% confidence level. Since the volume of this search region is 15 times as large as that when $|z| < 3$, we expect at the 95% confidence level fewer than 0.2 events in our hadronic event sample due to beam-gas interactions.

The effect of the visible energy requirement on a sample of Monte Carlo simulated hadronic events is illustrated in fig. 6.8. The size of the Monte Carlo data sample shown in the figure corresponds to the number of hadronic events expected in our data sample. A high 95% of the simulated events pass the limits on visible energy shown as lines in the figure. In fig. 6.9 is shown the minimum of the visible energy in either the forward or backward detector hemispheres for these same events. This plot better illustrates that the efficiency for hadronic events to pass the visible energy limit, unlike that for two photon events, is relatively insensitive to small changes in the limit value.

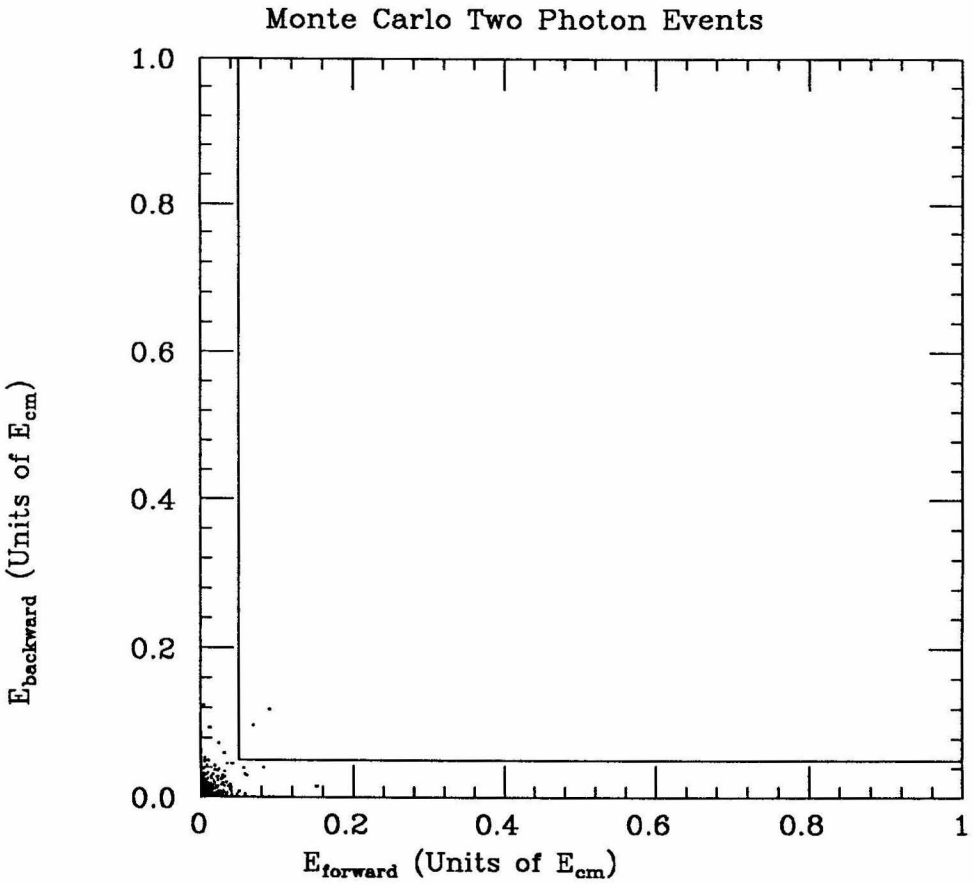

Figure 6.6. The distribution of visible energy in the forward versus the backward hemispheres of the detector for a sample of Monte Carlo simulated two photon events. The cuts at $0.05E_{\rm cm}$on the visible energy in each of the hemispheres are drawn as lines in the plot.

6.2.3 Efficiency of the selection procedure

The efficiency of the hadronic event selection, including trigger, was found from the Monte Carlo simulations to be $\epsilon_h = 0.953 \pm 0.006$. Differences in Monte Carlo models and the parameters of the simulation contribute an error of ± 0.004 to this uncertainty. The models used in this study were the Lund Shower model,[51] the Lund Matrix Element model,[52] and the Webber model.[53] Uncertainties in the energy scale in the electromagnetic calorimeters and in the charged track reconstruction efficiency

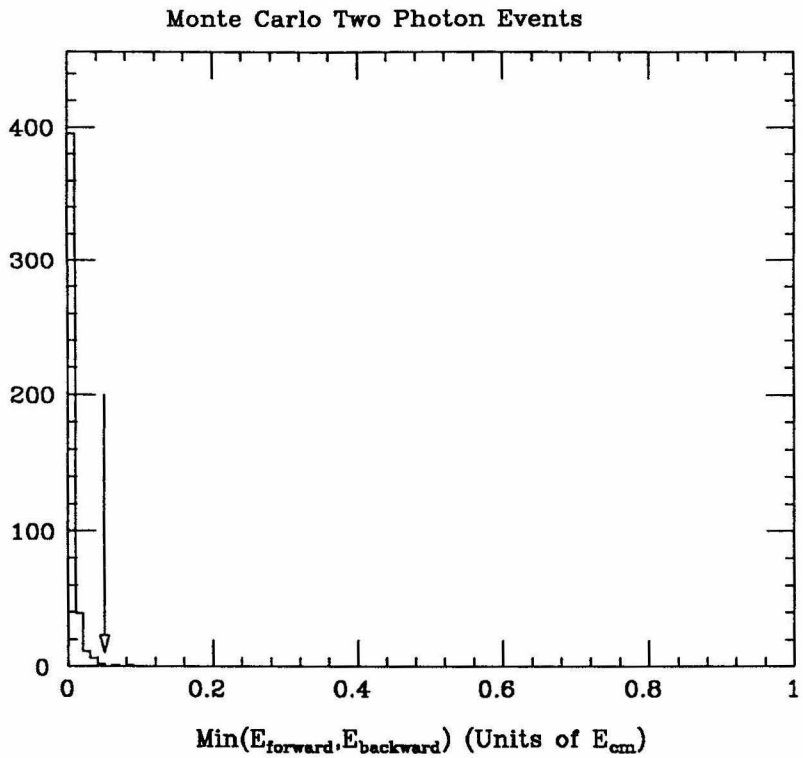

Figure 6.7. Minimum of the forward or backward visible energy for a Monte Carlo simulation of two photon events. The cut at 0.05 $E_{\rm cm}$ is shown by an arrow.

at large angles account for the remaining error in ϵ_h. Backgrounds from the beam are included in the Monte Carlo detector simulation by combining data from random beam crossings with Monte Carlo events. They are found to have little effect on the hadronic event selection efficiency.

The efficiency for simulated stable pair production events to pass the hadronic event selection has also been studied and a negligible 0.02 events from this source are expected in the hadronic sample. This low efficiency is due to the requirement that there be three tracks in hadronic events.

6.2.4 *Rejection of $\tau^+\tau^-$ events*

If we apply the above hadronic event selection cuts to a sample of Monte Carlo simulated $\tau^+\tau^-$ events produced at SLC energies we find that roughly 20% are ac-

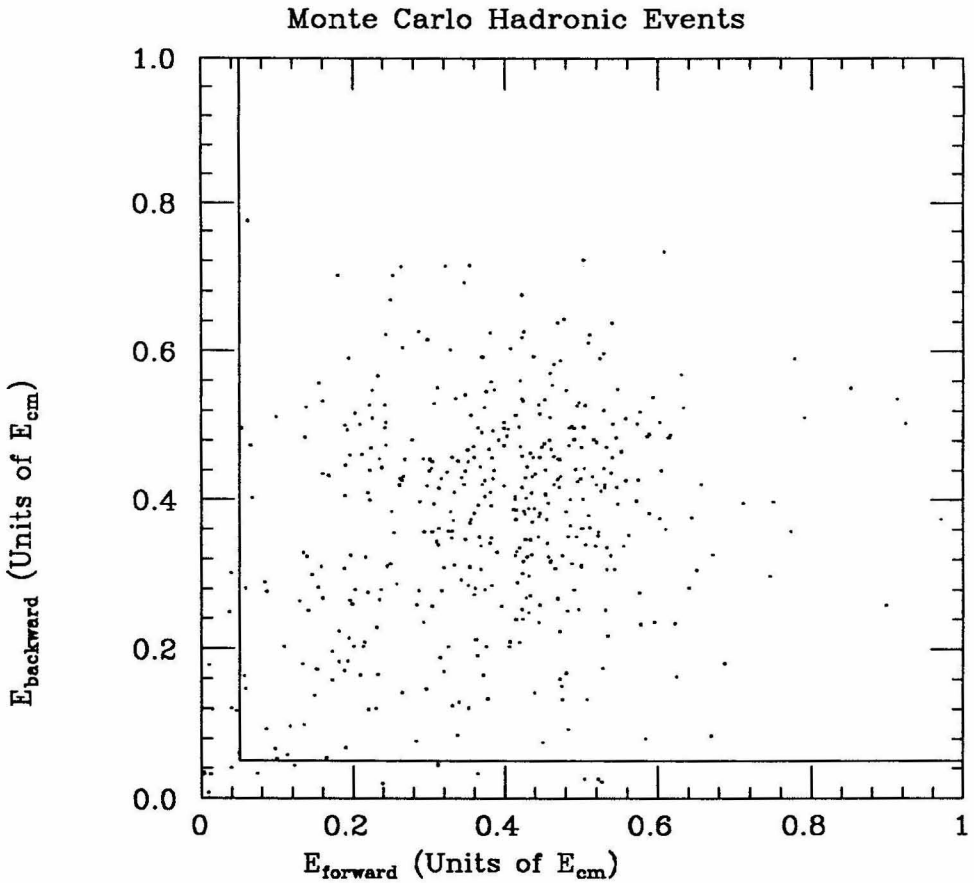

Figure 6.8. The distribution of visible energy in the forward versus the backward hemispheres of the detector for a sample of Monte Carlo simulated hadronic events. The cuts at $0.05E_{\rm cm}$ on the visible energy in each of the forward and backward hemispheres are drawn as lines in the plot.

cepted. Events passing the above hadronic selection criteria are classified $\tau^+\tau^-$ candidates if they satisfy the following two criteria:

- There are less than or equal to 6 charged tracks in the event passing the above requirements for well reconstructed tracks.
- A $\tau^+\tau^-$ candidate is required to have the thrust $T > 0.95$ with $|\cos\theta_{thrust}| < 0.65$ where θ_{thrust} is the polar angle of the thrust axis with respect to the beam line.

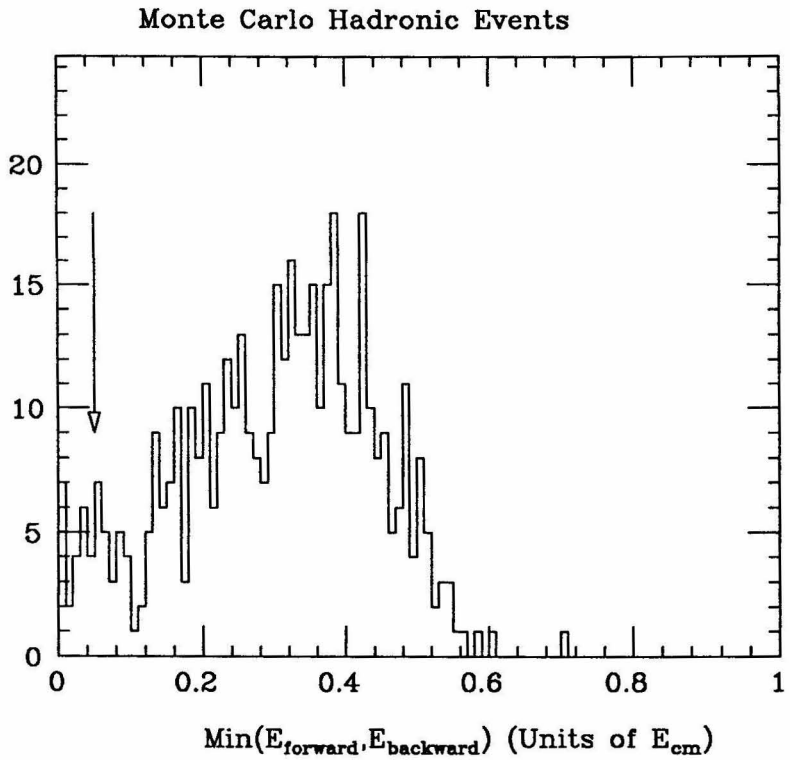

Figure 6.9. Minimum of the forward or backward visible energy for a Monte Carlo simulation of hadronic events. The cut at 0.05 $E_{\rm cm}$ is shown by an arrow.

Here, the thrust T is defined as

$$T = \max\left(\frac{\sum |p_{\parallel i}|}{\sum |p_i|}\right), \tag{6.1}$$

where $p_{\parallel i}$ is the longitudinal momentum of particle i relative to the thrust axis, which is chosen such as to maximize $\sum |p_{\parallel i}|$.

The selected events from the data that also pass the $\tau^+\tau^-$ candidate requirements are given their final classification based on a hand scan and the $\tau^+\tau^-$ events are removed. Twelve events from our data which pass the hadronic selecting cuts are also classified as $\tau^+\tau^-$ candidates and removed.

6.2.5 *Number of hadronic events found in the data*

A total of 455 hadronic events are found in the data after the $\tau^+\tau^-$ events are

removed. This events will serve as a normalization when we determine the number of charged leptons expected in our data as a function of lepton mass.

6.3 New stable charged particle event selection procedure

We now present the criteria designed to separate Z decays to pairs of stable charged particles from the other Z decay and background events in our reduced data sample. Since we will eventually be interested in finding candidate events containing new stable charged particle production, we would like to eliminate known stable particle pair production events as well. Therefore, we have designed the following set of requirements to eliminate e^+e^- events and also $\tau^+\tau^-$ events with both τ's decaying to one prong, which can resemble stable pair production events. Unfortunately, there is no simple way to remove $\mu^+\mu^-$ events without also reducing the efficiency for selecting new heavy stable charged pair production events.

6.3.1 *Efficiency of the selection due to solid angle coverage*

We will solve the problem of not being able to remove $\mu^+\mu^-$ pairs in our candidate event selection in the next chapter in which we develop a technique based on TOF, dE/dx, and momentum measurements to identify the masses of the particles in the selected events. This mass identification will then allow us to distinguish $\mu^+\mu^-$ events from new heavy pair events. Thus, we must require here that the particles in the selected stable pair events traverse the central drift chamber and hit the TOF scintillators. This defines the solid angle acceptance of the selection. The expected acceptance for stable pairs, if we approximate their angular distribution by $1+\cos^2\theta$, would be just under 60% defined by the active solid angle coverage of the TOF system.

6.3.2 *Summary of the candidate event selection requirements*

The following five criteria must all be met for an event to be selected as a candidate stable charged particle-antiparticle production event:

1) The event must contain only two charged tracks emanating from a cylindrical volume of radius 1 cm and half-length 3 cm around the beam line, centered at the e^+e^- interaction point (IP).
2) The two tracks must be back-to-back with $|\cos\theta_{acol}| > 0.99$, where θ_{acol} is the acollinearity angle between the tracks.
3) Both tracks must have momentum greater than 5 GeV/c with the magnitudes being equal to each other within 3σ.
4) At least one track must hit the active region of the TOF system and must have a time not more than 1.25 nanoseconds earlier than expected for a velocity of $\beta = 1$.
5) Each track must deposit less than 20 GeV in the calorimeters.

6.3.3 Efficiency of the requirements

The efficiency of the selection requirements applied in the order listed to Monte Carlo simulations * of Z decays to e^+e^-, $\mu^+\mu^-$, $\tau^+\tau^-$ and heavy stable charged forth generation lepton pairs ($l_4^+l_4^-$) are listed in Table 6.2. An emulation of the trigger is also applied and the resulting trigger efficiency is listed in the table. The trigger emulation is run after requirement 4) is applied, as this defines the solid angle coverage of our selection through the coverage of the TOF system.

The resultant efficiency for stable charged lepton pair events to pass the requirements is found to be 57% as listed in the table. This number is consistent with the 60% efficiency due to solid angle coverage alone multiplied by a 96% trigger efficiency and a 99% efficiency for the cut on the acolinearity angle between the two tracks. It is evident from the numbers in the table that e^+e^- and $\tau^+\tau^-$ events are selected with low efficiency when compared to $\mu^+\mu^-$ and $l_4^+l_4^-$ events, which are selected with the same efficiency.

---

* Details of the Monte Carlo generators are included in Appendix A.

Table 6.2. Efficiencies for the selection of candidate events for different Z decay final states.

Event types $\rightarrow$	e^+e^-	$\mu^+\mu^-$	$\tau^+\tau^-$	$l_4^+l_4^-$
Requirement 1): Two charged tracks must emanate from the IP	0.84	0.84	0.59	0.85
Requirement 2): Tracks must be back-to-back with $\mid \cos\theta_{acol} \mid > 0.99$	0.95	0.99	0.89	0.99
Requirement 3): Tracks must have equal momenta > 5 GeV/c^2	0.93	1.00	0.26	1.00
Requirement 4): At least one track must hit the active TOF system	0.70	0.70	0.43	0.70
Trigger emulation	1.00	0.96	0.92	0.96
Requirement 5): Shower energy must be < 20 GeV/c^2 for each track	0.03	1.00	0.73	1.00
Total efficiency	0.02	0.57	0.04	0.57

6.3.4 Detailed discussion of the selection requirements

We will now discuss in greater detail the selection requirements and the resulting efficiencies listed in Table 6.2. The details of the Monte Carlo simulated events used in this discussion are presented in Appendix A.

The first requirement is that the candidate stable charged pair events must have two reconstructed charged tracks emanating from a cylindrical volume of radius 1 cm and half-length 3 cm around the beam line, centered at the interaction point.† A

† The choice of values for the radius and half-length limits have already been

limit of $|\cos\theta| < 0.92$ for each track is implied due to the drift chamber solid angle coverage (which is later be superseded by the lesser coverage of the TOF system). This solid angle limit is the reason that the efficiency for $\mu^+\mu^-$ pairs is 84%.

Requirement 2) requires the tracks to be back-to-back with $\cos\theta_{\rm acol} > 0.99$, where $\theta_{\rm acol}$ is the acollinearity angle between the tracks defined as

$$\cos\theta_{\rm acol} = -\frac{p_{1x}p_{2x} + p_{1y}p_{2y} + p_{1z}p_{2z}}{\| \mathbf{p}_1 \| \| \mathbf{p}_2 \|}, \tag{6.2}$$

where the tracks measured momentum is given by $\mathbf{p} = (p_x, p_y, p_z)$. In other words, the "kink angle" between the two tracks must be less than 8.1 degrees. Shown in fig. 6.10 is the distribution of $\cos\theta_{acol}$ for a sample of 3,000 Monte Carlo simulated $l_4^+ l_4^-$ events (in this case, a 20 GeV/c^2 particle mass was used for the leptons in the simulation), which was first reduced by requiring that the events pass requirement 1). As listed in Table 6.2 and illustrated in fig. 6.10, 2) introduces only a slight inefficiency for stable pair events (including $\mu^+\mu^-$ events) due to the kinks caused by initial and final state radiation.

Requirement 3) is actually a series of two limits on the particle momenta that are designed to reduce the background from $\tau^+\tau^-$ pairs with both τ's decaying to one prong. The first requirement is that each track has a momentum greater than 5 GeV/c. This removes the tail of the $\tau \rightarrow$ one prong momentum distribution as illustrated in fig. 6.11 for a sample of 3,000 Monte Carlo simulated $\tau^+\tau^-$ events, which was first reduced by requiring that the events pass 1) and 2).

This requirement does not seriously limit our acceptance of heavy stable charged particles. Since we are assuming pair production from Z decay we have for each particle with mass M and momentum p that $[p^2 + M^2]^{\frac{1}{2}} = E_{cm}/2$. Taking $p = 5$ GeV/c in this expression shows that the minimum momentum requirement only leaves us insensitive to masses which are greater than about $0.994E_{\rm cm}/2$. This is not a

discussed earlier in this chapter in the section on hadronic event selection. See fig. 6.4.

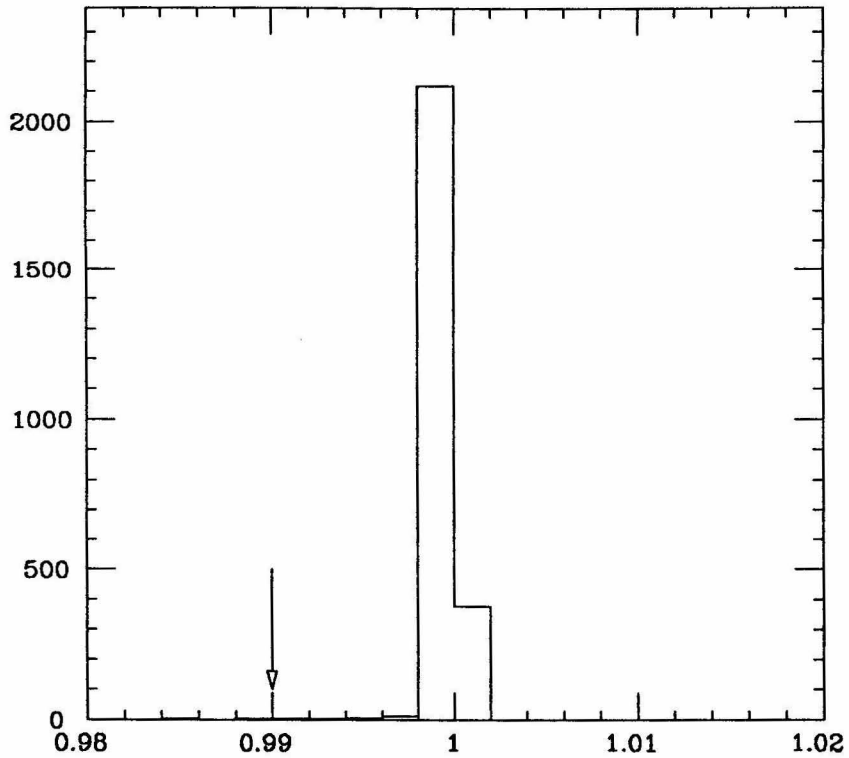

Figure 6.10. Distribution of $|\cos\theta_{acol}|$ for stable charged lepton pairs. The cut at 0.99 is shown by an arrow.

problem since, due to the size of our data sample, less than one event is expected to have been produced during our data run in this high mass range above 44.5 GeV/c^2.

The second requirement in 3) is based on our expectation that, for stable pair production, both particles have equal momenta. Here we consider the normalized momentum difference

$$\frac{\Delta p}{\sigma_{\Delta p}} = \frac{p_1 - p_2}{\sqrt{\sigma_{p_1}^2 + \sigma_{p_2}^2}}, \tag{6.3}$$

between the two tracks in the event. As will be shown in Appendix A, the measurement error on the momentum p follows, to a good approximation, the Gaussian distribution (the error on $1/p$ is truly Gaussian). Thus, for stable pairs where $p_1 = p_2$, we would expect the normalized momentum difference to approximate a Gaussian distribution of unit width. If it were exactly a Gaussian distribution, then a limit

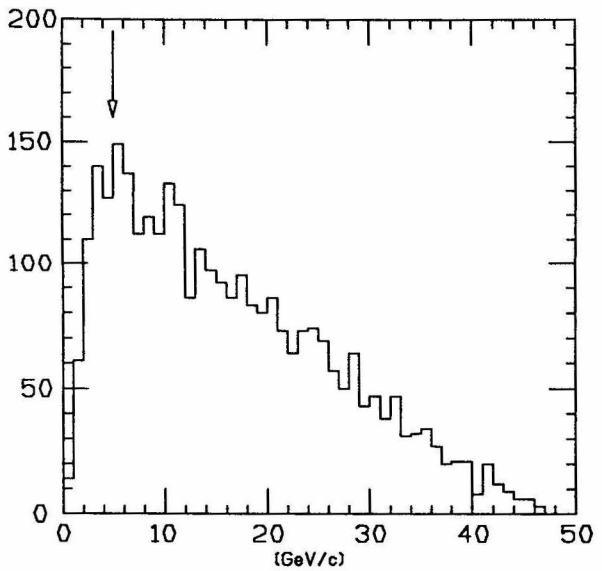

Figure 6.11. Momentum distribution of each track in a Monte Carlo simulation of two prong $\tau^+\tau^-$ events with back-to-back tracks. The cut at 5 GeV/c is shown by an arrow.

requiring that $|\Delta p/\sigma_{\Delta p}| \leq 3$ would pass 99.46% of all stable pair events. We observe $\simeq$ 99% efficiency for this requirement for Monte Carlo simulations of heavy stable charged lepton events.

The limit at ± 3 in the normalized momentum removes a significant percentage of $\tau^+\tau^-$ events which first pass 1) and 2). In fig. 6.12 is shown the distribution of the normalized momentum difference for the two prongs from $\tau^+\tau^-$ decays for a sample of 3,000 Monte Carlo simulated events, which was first reduced by requiring that each event pass requirements 1) and 2). We see from fig. 6.12 that applying a cut at $|\Delta p/\sigma_{\Delta p}| \leq 3$ removes about 72% of the 2 prong $\tau^+\tau^-$ events. As listed in Table 6.2, applying both the 5 GeV/c requirement and the limit at ± 3 on the normalized momentum difference removes about 74% of the remaining $\tau^+\tau^-$ events while having a small effect on stable pair events.

Since the mass determination for selected events that will be developed in the next chapter is based in part on TOF measurements, 4) requires that at least one track must hit the active region of the TOF system. It also requires that the same

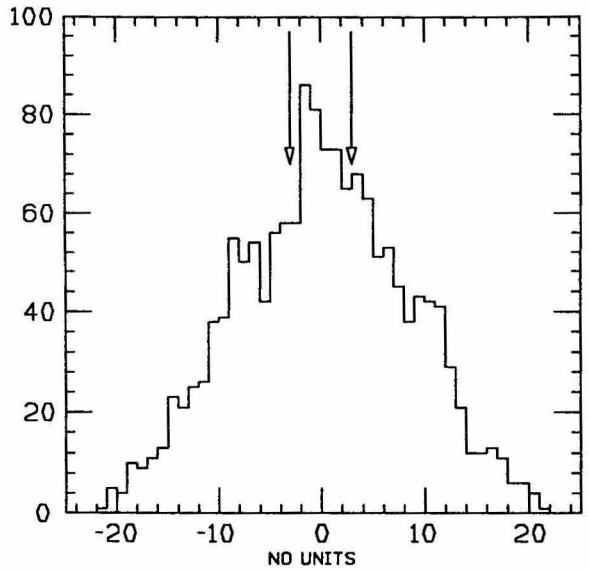

Figure 6.12. Distribution of the normalized momentum difference for tracks in a Monte Carlo simulation of two prong $\tau^+\tau^-$ events with back-to-back tracks. The cuts at ± 3 are shown by arrows.

track have a time not more than 1.25 ns earlier than that expected for a $\beta = 1$ particle. This limit on early times insures that the TOF measurement is not used if it has been corrupted by SLC machine backgrounds. The early time requirement introduces a slight inefficiency that can be inferred from the distribution of expected TOF times shown in fig. 5.10. As shown in the figure, about 6% of tracks would fail the cut on early times. Studies of the TOF data show that the backgrounds which cause the early times are not uniform throughout the system, making it unlikely that both tracks in an event, if they are back-to-back, would fail this requirement. Therefore, by requiring that only one track have a good TOF time, we virtually eliminate the effect that this source of background has on the overall event selection efficiency.

The TOF requirement implies that at least one track must have $|\cos\theta| < 0.70$ due to the solid angle coverage of the TOF system. The efficiency listed in Table 6.2 for events to pass this requirement is due mostly to this solid angle coverage. As noted earlier in the text, we would expect around 60% of stable charged pair production events to be accepted by the limit imposed by the TOF solid angle coverage. The

70% figure listed in the table for the efficiency of these types of events to pass the cut is due to the reduction of the solid angle acceptance by requirement 1). Taking the product of the efficiencies for requirements 1) and 4) gives an efficiency close to 60%.

Finally, stable particles with masses greater than the muon mass are not expected to produce electromagnetic showers. Therefore, 5) requires for each track an energy deposition of less than 20 GeV in the calorimeters. This limit almost eliminates the background from e^+e^- events as shown in fig. 6.13 and reduces it somewhat, as shown in fig. 6.14, for $\tau^+\tau^-$ pairs with subsequent $\tau \rightarrow e\nu\bar{\nu}$ decays. The slight inefficiency in the removal of e^+e^- pairs by this cut is due to the 3° cracks in ϕ between the eight the liquid argon modules. The requirement has no effect on new heavy stable charged particles since the maximum expected ionization energy lost in the liquid argon shown in fig. 6.15 is well below the 20 GeV level. *

6.3.5 Number of candidate events expected in the data

In order to determine if there is a signal in our data for new stable charged particle production, we first need to estimate the expected number of events due to the different production assumptions of the of the Standard Model and its extensions. We begin with the case of a fourth generation stable charged lepton. The result will also apply to the case of mirror leptons and is easily modified to the case of supersymmetric scalar leptons.

Based on the assumptions of the Standard Model, the expected number of charged lepton pairs produced with a mass M, $N_l(M)$, can be normalized to the number of hadronic decays, n_h, by the ratio of the expected partial decay widths of

---

* The original purpose of 5) was to remove e^+e^- events exclusively. It is clear from figures 6.13, 6.14, 6.15 and 6.5 that its value could have been set lower to remove more $\tau^+\tau^-$ events. Due to the limited size of our Z decay data sample, however, lowering the value of this limit has no effect on the final results of this thesis.

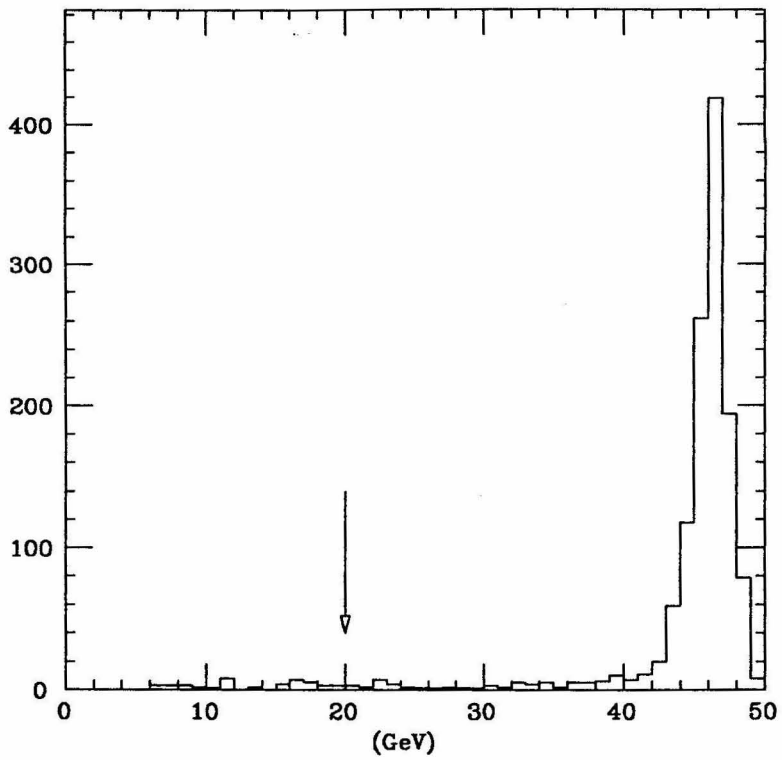

Figure 6.13. The minimum of the electron or positron energy in the liquid argon calorimeter for the remaining events from a sample of 3,000 Monte Carlo simulated e^+e^- pairs after the first 4 cuts of the stable charged pair selection have been applied. The cut at 20 GeV is shown by an arrow.

the Z as

$$N_l(M) = \frac{1}{\epsilon_h} \sum_{i=1}^{n_h} \frac{\Gamma_{ll}(M, E_{cm})}{\Gamma_h(E_{cm})}, \tag{6.4}$$

where the center-of-mass energy $E_{\rm cm}$ measured by the extraction line energy spectrometer (section 4.2.7) for hadronic event i is used in computing the dependence of the Z partial decay widths on the velocity $\beta = [1 - 4M^2/E_{\rm cm}^2]^{1/2}$ of the final state leptons or quarks. Here, Γ_h is the partial width of the Z decay into hadrons as given by eqn. 3.19 and Γ_{ll} is the leptonic width as given by eqn. 3.14. In eqn. 6.4 for the number of expected events, the number of hadronic events n_h is corrected for detection efficiency by the factor $1/\epsilon_h$.

The partial width of the Z decay into charged leptons can be written in terms

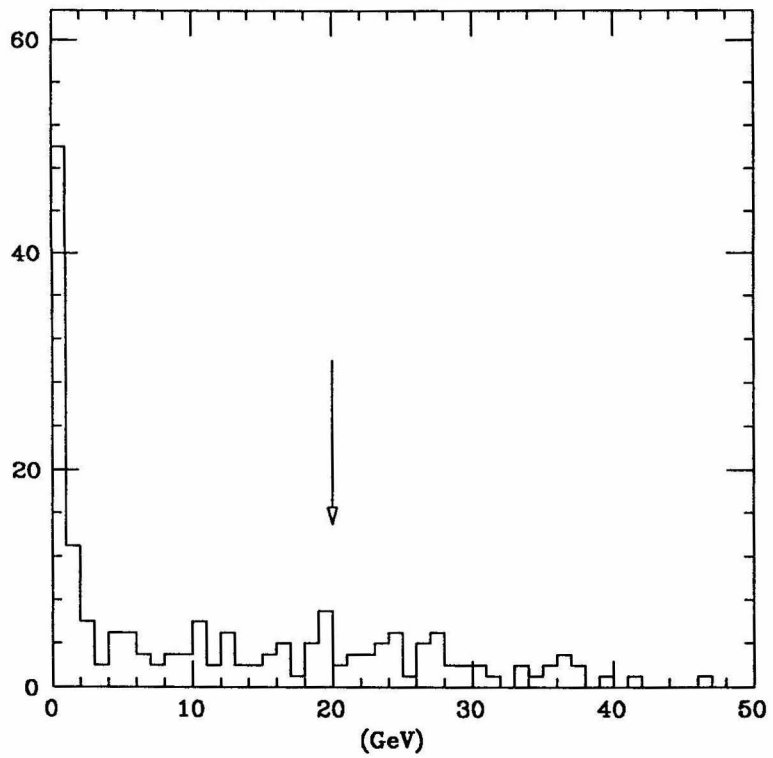

Figure 6.14. The minimum of the energy in the liquid argon barrel calorimeter deposited by either of the two tracks in the remaining events from a sample of 3,000 Monte Carlo simulated $\tau^+\tau^-$ pairs after the first 4 cuts of the stable charged pair selection have been applied. The cut at 20 GeV is shown by an arrow.

of the width for Z decay to e^+e^- , Γ_{ee} given by eqn. 3.15:

$$\Gamma_{ll}(M, E_{cm}) = \frac{\beta\left(\frac{1}{2}(3-\beta^2)V_l^2 + \beta^2 A_l^2\right)}{V_l^2 + A_l^2}\Gamma_{ee}. \tag{6.5}$$

The partial hadronic and leptonic widths of the Z and the coupling constants V_f and A_f, as given by eqn. 3.8, are obtained from the Standard Model with $\sin^2\theta$ as determined from eqn. 3.29 using the values[19] M_Z=91.14 GeV/c^2, M_{top}=100 GeV/c^2, and M_{Higgs}=100 GeV/c^2. The QCD radiative corrections are also applied using the value[58] α_s=0.123 in eqn. 3.24. The dependence of the expected number of events on these parameters is small. For example, a 0.8% reduction in N_l is obtained if the values M_{top}=200 GeV/c^2, M_{Higgs}=1 TeV/c^2 and α_s = 0.140 are used, with

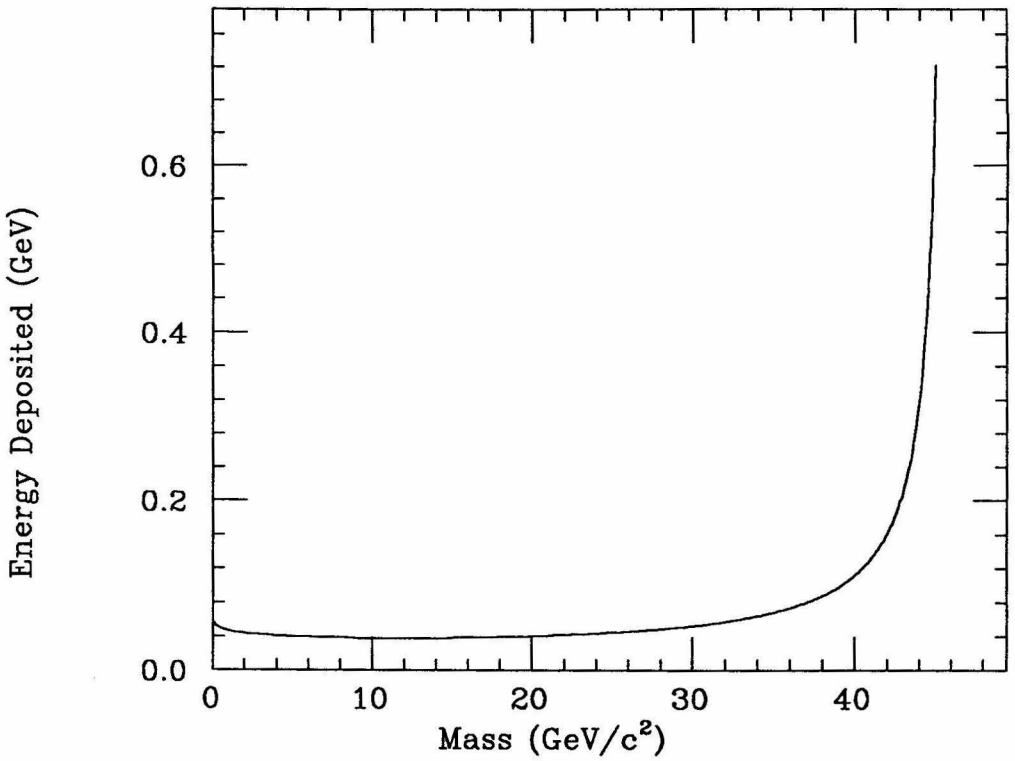

Figure 6.15. The maximum ionization energy in the liquid argon calorimeter as a function of particle mass for stable charged particles produced in pairs in Z boson decay. This plot assumes the particles traverse the liquid argon module at an angle of 45° in θ and 22.5° in ϕ. Note that this is a plot of the ionization energy loss in the argon only and does not include the losses in the lead.

the largest contribution coming from the change in the size of the QCD radiative corrections.

The systematic error on N_l due to the uncertainty in the center-of-mass energy is negligible for stable lepton masses below 40 GeV/c^2 but is included above this mass. The largest source of uncertainty in N_l comes from the 4.6% statistical error on the number of hadronic events selected.

We now use eqn. 6.4 to find the number of charged lepton pairs that are expected to have been produced during our data collection run. For the $n_h = 455$ hadronic events found in the data with an expected efficiency $\epsilon_h = 0.953$ (as found in section

6.2.3), we get the expected number of stable charged lepton pairs produced at the SLC as a function of mass shown in fig. 6.16. From the figure we see that about 23 charged lepton events are expected if the masses of the leptons are below about 2 GeV/c^2. This means that we would expect 23 events of each of the known charged lepton pairs e^+e^-, $\mu^+\mu^-$, and $\tau^+\tau^-$. We will later show that this is in good agreement with the numbers of these events found in the data after detection efficiencies have been taken into account. On the high end of the mass scale in fig. 6.16 we see that, above about 43 GeV/c^2, the rate drops to less than one pair produced during our data run. Now that we have found the number of stable charged lepton pair production events expected to have been produced during our data run at the SLC, we can turn to the problem of selecting from our data sample those that triggered the detector.

6.3.6 Number of candidate events found in the data

If we keep only those events from our data sample which satisfy the above five criteria, we select 13 events as listed in Table 6.3. We now compare this finding to our expectations from known Standard Model processes.

6.3.7 Backgrounds to heavy particle production

The backgrounds from beam halo, synchrotron radiation and beam-gas events (described in section 6.1.3), together with cosmic ray events were again studied by displacing the volume which defines the e^+e^- interaction region in requirement 1) to $3 < |z| < 50$ cm and $|r| < 1.5$ cm. In this case, one cosmic ray event passes the candidate selection cuts. Since the volume of this search region is 33 times as large as that when $|z| < 3$, we expect at the 95% confidence level that fewer than 0.15 events in our candidate sample are due to these background sources. In a sample of two photon events from a Monte Carlo simulation representing 100 times the integrated luminosity of our data sample no events were found to pass the candidate event selection cuts. Therefore, a negligible 0.03 background events are expected from this

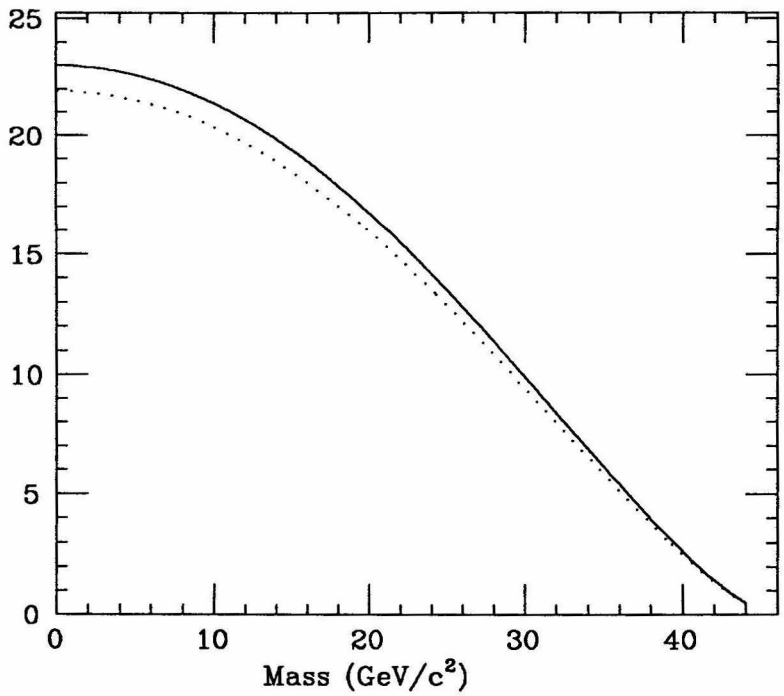

Figure 6.16. The expected number of stable lepton pairs produced at the SLC in the reported data sample as a function of particle mass. The dotted curve shows the expected number if the systematic and statistical errors discussed in the text conspire to reduce the expectation.

source. In what follows we choose to neglect the small expected backgrounds from all of these sources.

In section 6.3.5 we found that we expect 23 events of each of the Standard Model lepton pairs e^+e^-, $\mu^+\mu^-$, and $\tau^+\tau^-$ to have been produced by the SLC but not necessarily detected by the MARK II. With this number of events produced and the efficiencies from Table 6.2, we compute that 0.46 e^+e^- events, 13.1 $\mu^+\mu^-$ events, and 0.92 $\tau^+\tau^-$ events are expected to pass the candidate event selection cuts. Summing these numbers gives a total of 14.5 candidate events in a sample the size of our data set. This is in good agreement with the 13 events actually selected from the data. In the next chapter we will show that one of these data events is consistent with

Table 6.3. Number of events remaining after the cuts are applied in series to the 20,576 events of the reduced data sample.

Event types →	Data Events
Requirement 1): Two charged tracks must emanate from the IP	2,624
Requirement 2): Tracks must be back-to-back with $\mid \cos\theta_{acol} \mid > 0.99$	216
Requirement 3): Tracks must have equal momenta > 5 GeV/c^2	44
Requirement 4): At least one track must hit the active TOF system	22
Trigger emulation	22
Requirement 5): Shower energy must be < 20 GeV/c^2 for each track	13
Total data events	13

being a $\tau^+\tau^-$ pair and the remaining 12 are consistent with being $\mu^+\mu^-$ pairs. First, however, we will see how well we can set a limit on new stable lepton production based only on the fact that we selected 13 events and expected 14.5 from known processes.

6.3.8 New particle production limits based on candidate rate

We can exclude new stable charged pair production for masses above m_μ, the mass of the muon, using an indirect search method based on event rate only (the results do not hold for particle masses below m_μ due the 20 GeV limit on calorimeter

energy). The approach is to treat the 13 data events selected above as a combination of both signal from new stable pair production and expected background from known leptons. A conservative upper limit S on the number of signal events can then be determined[6] from the relation

$$CL = 1.0 - \frac{e^{-(B+S)} \sum_{n=0}^{n_0} \frac{(B+S)^n}{n!}}{e^{-B} \sum_{n=0}^{n_0} \frac{B^n}{n!}}, \tag{6.6}$$

where CL is the confidence level, n_0 is the observed number of events, B is the expected number of background events and S is the upper limit on number of signal events in n_0. Setting $CL = 0.95$ in eqn. 6.6 selects the 95% confidence level. We find the upper limit at 95% confidence level to be 8.1 signal events for 13 observed events and 14.5 expected background events. Taking this upper limit together with the charged lepton production rate, eqn. 6.4, and the efficiency for stable pairs to pass the selection criteria given in Table 6.2, we exclude the production of stable fourth generation charged lepton pairs with particle masses from m_μ to 22.7 GeV/c^2, that is, this is the range in mass for which more than 8.1 events are expected to be selected. For supersymmetric scalar leptons, where the production rate is given by eqn. 3.36, the excluded region extends from m_μ to 8.0 GeV/c^2. These limits are not as good as those found in other experiments as referenced in section 2.5.1. We must, therefore, develop further means of rejecting backgrounds from known pair production processes to see if any signal remains in our data for masses above the previous limits. This is the topic of the next chapter.

Chapter 7

The Search Analysis

In this chapter we develop a method to identify the masses of the particles in the candidate events. We use the maximum likelihood method to find the mass at which the expected values of the TOF, dE/dx, and momentum p best agree with the actual measured values for the tracks in the events. Those in which this mass is over 2 GeV/c^2 will be taken as signal events due to heavy stable charged particle production. Those with masses below 2 GeV/c^2 are indistinguishable from $\mu^+\mu^-$ pair events. In addition, such signal events must pass a chi-square test based on the same set of detector measurements to determine whether the stable charged particle pair production hypothesis holds. Removing those events which fail the chi-square test further reduces the background due to $\tau^+\tau^-$ events. Finally, assuming that they exist, we determine as a function of particle mass the expected number of stable charged fourth generation lepton events that would remain as signal. We then compare this expectation to the number of signal events in the data. The results are also extended to the case of mirror fermion and supersymmetric scalar lepton production.

7.1 The maximum likelihood mass assignment

In section 2.1 it was shown that the values of the momentum p, the dE/dx, and the TOF measurements expected by the MARK II detector for stable particles produced in pairs from the decay of the Z boson could be calculated as a function of particle mass. This information, shown in fig. 2.1, is now used to find for each

candidate event the mass M at which these predicted values best match the actual detector measurements for both tracks. We use the maximum likelihood method[72] to find this mass. We construct the likelihood function

$$\mathcal{L}(M) \equiv \prod_{\substack{i=1 \\ \text{tracks}}}^{2} f(t_i)\, g(\frac{dE}{dx_i})\, g(\frac{1}{p_i}), \tag{7.1}$$

where $f(t)$ is defined in eqn. 5.4 with $t = TOF_{\text{measured}} - TOF_{\text{expected}}(M)$ and the Gaussian distribution $g(x)$ is given by

$$g(x) = \frac{1}{\sqrt{2\pi}\sigma_x(M)} \exp\left(-\frac{1}{2}A(x)\right), \tag{7.2}$$

with argument

$$A(x) = \left(\frac{x_{\text{measured}} - x_{\text{expected}}(M)}{\sigma_x(M)}\right)^2. \tag{7.3}$$

This likelihood function is simply the product of the six individual probability distributions for the TOF, dE/dx, and $1/p$ measurements for the two tracks. The resolutions used in the likelihood function for $1/p$ and dE/dx are consistent with those given in section 4.2.1 of $\sigma_p/p = [(0.0031p)^2 + (0.014)^2]^{1/2}$ and $\sigma_{dE/dx} = (0.085)dE/dx$. They are, however, calculated on a track-to-track basis depending on the quality of the fits in the track and dE/dx reconstruction. A justification of the Gaussian form of these measurement error distributions can be found in Appendix A.

The six individual probability distributions all have their maxima at the particular mass where the measured value of the TOF, dE/dx, or momentum is equal to the expected value calculated at that mass. In general, these maxima occur at slightly different masses due to measurement error. A single most probable mass is determined based on these six functions using the maximum likelihood principle. Here, the mass $M \geq 0$, which maximizes the product of the six independent distributions $\mathcal{L}(M)$, provides the most probable mass assignment for the particles in a candidate

event. It is this most probable mass that we will use to distinguish heavy stable charged particle production from the $\mu^+\mu^-$ background.

7.1.1 The mass resolution for new stable particles

The resolution of the most probable mass assignment method is not constant over the mass range accessible for stable particle production at the SLC. This is due to the fact that the ratios of the measured quantities to their resolutions, i.e., TOF/σ_{TOF}, $(dE/dx)/\sigma_{dE/dx}$, and p/σ_p, all vary as a function of mass as shown in fig. 2.1. In fig. 7.1 are shown some examples of distributions of the mass assignment determined from Monte Carlo simulations* of stable charged lepton pair production events at the SLC. From these distributions we see that the resolution of the most probable mass assignment does not vary in a simple way as a function of particle mass. Therefore, if a signal were present at a high mass value in the data, we would need to use these distributions, together with the expected event rates for candidate signal particles, to unfold the mass of the particles in the signal events.

The resolution of the mass assignment is best above 25 GeV/c^2 where the distribution assigned masses is strongly peaked at the true mass of the particles. This is fortunate as the expected event rate for new stable charged particle pairs decreases with increasing energy (see eqns. 3.13 and 3.14). The resolution is worst for masses in the range between about 5 and 25 GeV/c^2. This is due to the fact that for any two masses in this region, the differences between the expected TOF, dE/dx, and momentum measurements at the two masses are small compared to their corresponding measurement errors for these quantities. This fact can be observed from the plots of the expected measurement values and resolutions shown in fig. 2.1. It should also be noted that the expected values of the dE/dx measurement in this range can be consistent with two separate mass assignments. This fact explains the double peaking in the distributions of the most probable mass assignments shown in fig. 7.1.

---

* The details of the Monte Carlo simulations are discussed in Appendix A.

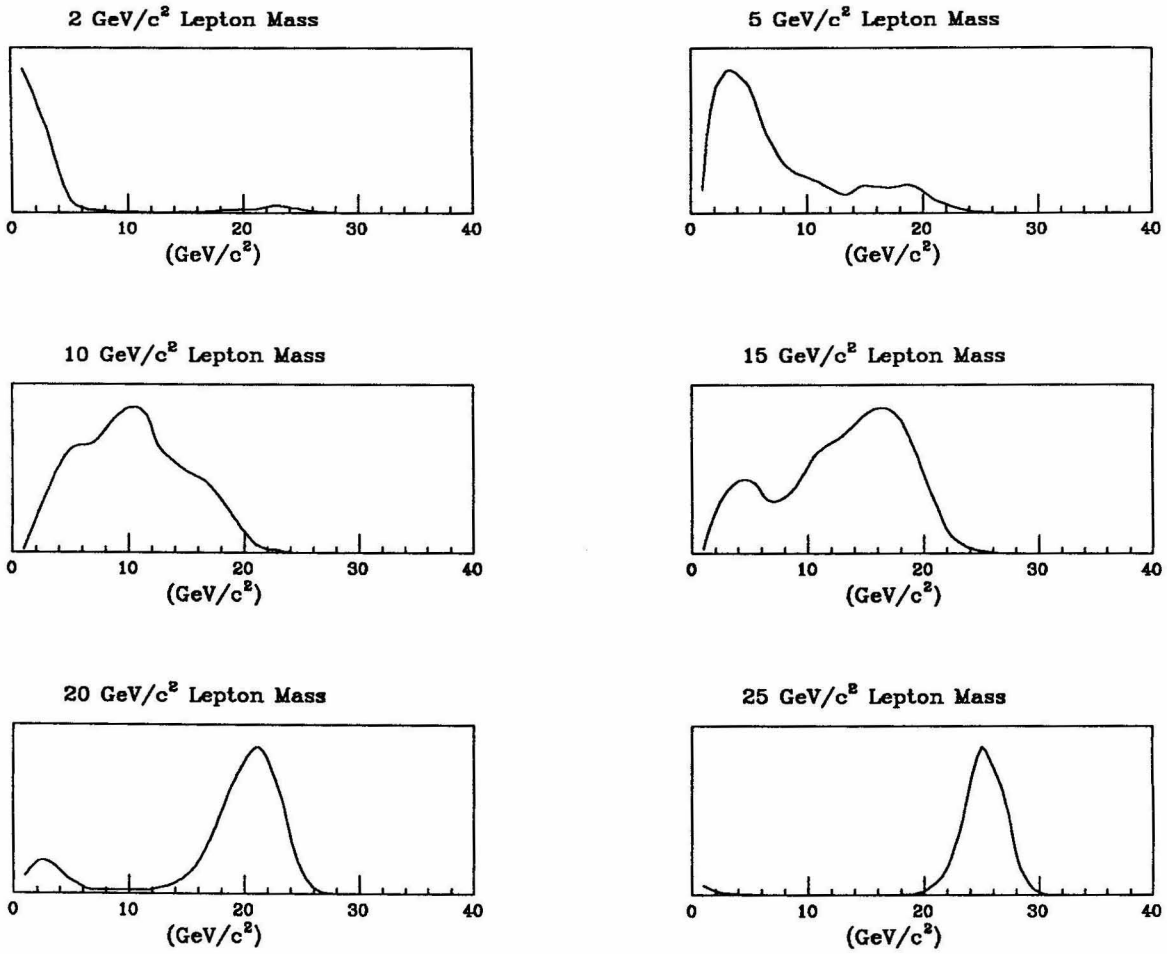

Figure 7.1. Examples of the maximum likelihood mass assignment distributions expected for stable charged leptons of different masses.

7.1.2 *Mass resolution for $\mu^+\mu^-$ pairs and the 2 GeV/c^2 mass limit*

The criteria developed to select stable charged pair production candidates from the data have the same efficiency for selecting both $\mu^+\mu^-$ events and heavy stable forth generation charged lepton pair production events. We therefore need some way to separate these two classes of events. In fig. 7.2 is shown the most probable mass

distribution for $\mu^+\mu^-$ pairs. This distribution falls to zero at about 1 GeV/c^2 (with the exception of a few events around 30 GeV/c^2 due to the double peaking of the most probable mass assignment distribution as discussed in the previous section). We use this fact to distinguish heavy stable fourth generation lepton pairs from $\mu^+\mu^-$ pairs by requiring that the most probable mass assigned to them be greater than 2 GeV/c^2. The efficiency to pass this limit should be high for stable charged pair production events in which the particle masses are above 5 GeV/c^2. That this is in fact true can be seen from the distributions for the most probable mass assignment shown in fig. 7.1. The actual values of this efficiency as a function of particle mass will be found later after another important requirement, introduced next, is applied.

7.1.3 *A chi-square test for pair production*

There are Z decay processes that are not due to stable particle-antiparticle production but still have the topology expected for candidate events. The only one of these processes with a significant rate at the SLC is that of $\tau^+\tau^-$ production where both τ's decay to one stable charged particle and neutrals. For example, a $\tau^+\tau^-$ event with the subsequent decays $\tau^+ \rightarrow \mu^+\nu_\tau\bar{\nu}_\mu$ and $\tau^- \rightarrow \pi^-\nu_\tau$ could be selected as a candidate event if the tracks from the μ and π ended up back-to-back in the detector and had nearly equal momenta. In this case, the most probable mass assigned to the particles is larger than their actual masses because the energy carried by the invisible neutrinos is mistakenly attributed to the rest masses of the charged particles.

If the neutrinos in $\tau^+\tau^-$ events selected as candidates have large enough energies, then there will be a disagreement between the mass assignments for the charged particles that are favored by the individual momentum, dE/dx, and TOF measurements alone. As a result, the magnitude of the likelihood function at the most probable mass will be lower than that found for true stable charged pair production events. We could, therefore, make a cut on the magnitude of the likelihood function at the most probable mass as a test of the stable particle pair production hypothesis. This is

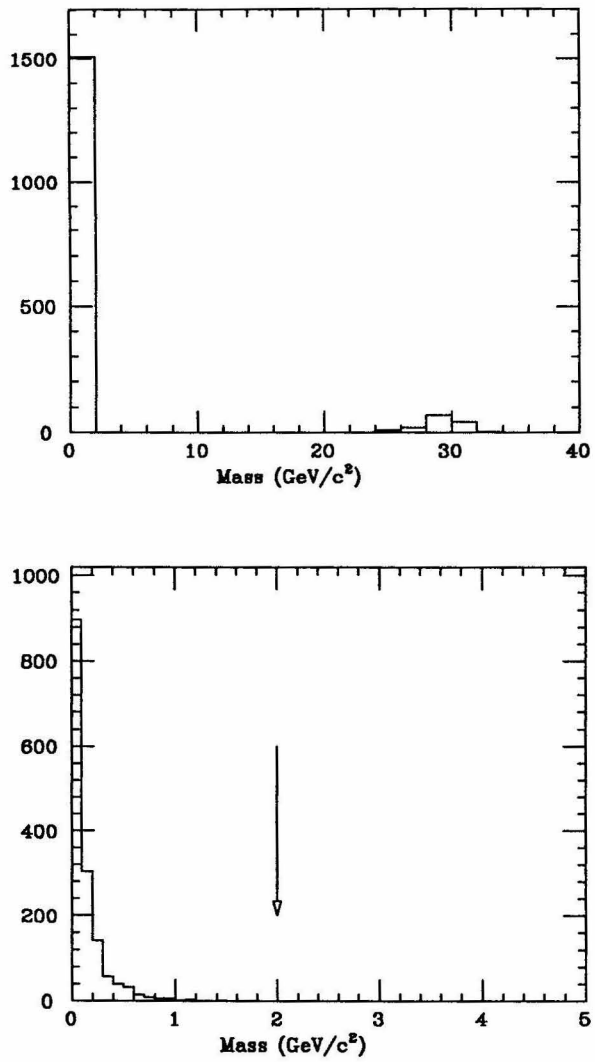

Figure 7.2. Most probable mass distribution for a sample of 3,000 Monte Carlo simulated $\mu^+\mu^-$ events. The events are first required to pass the stable particle selection cuts before the mass assignment is made. The two plots show the same distribution with different scales.

equivalent to making a cut on the magnitude of the more commonly used chi-square[73]

$$\chi^2(M) = \sum_{\substack{i=1 \\ \text{tracks}}}^{2} \left(A(t_i) + A(\frac{dE}{dx_i}) + A(\frac{1}{p_i}) \right), \tag{7.4}$$

at the most probable mass M where $A(x)$ is given by eqn. 7.3. Here, we assume the Gaussian approximation to the TOF measurement error distribution given by eqn. 5.4 for $t \geq t'$. Also, if one of the two tracks does not have a good TOF measurement as defined by requirement 4) of the candidate events selection criteria (section 6.3.2), then we do not include $A(t)$ for that track in the sum for the chi-square.

A plot of the expected chi-square distribution for 3,000 stable charged lepton events from a Monte Carlo simulation is shown in fig. 7.3. Also shown in the figure is the chi-square distribution

$$\chi^2(x) = \frac{1}{2^{\frac{k}{2}}\Gamma(\frac{k}{2})} x^{\frac{k}{2}-1} \exp(-\frac{x}{2}) \tag{7.5}$$

for k = 5 degrees of freedom. This is the expected distribution for $\chi^2(M)$ since we have six independent measurements and one constraint, the mass M. The deviation from the expected distribution comes about because we have made a Gaussian approximation to the TOF measurement error distribution. It is also caused by non-Gaussian tails in the $1/p$ and dE/dx measurements which arise from SLC backgrounds.

We set a limit at 50 on the value of $\chi^2(M)$ to serve as a test of the stable pair production hypothesis. The limit is set at 40 if only one of the two tracks has a good TOF measurement as defined by event selection requirement 4). In other words, we require the chi-square per degree of freedom to be less than 10. We see from fig. 7.3 that this cut has little effect on stable charged pair production events. It does, however, have an effect on $\tau^+\tau^-$ events. Shown in fig. 7.4. is the distribution of the value of $\chi^2(M)$ for the 127 events which satisfy the candidate event selection from a total of 3,000 Monte Carlo simulated Z decays to $\tau^+\tau^-$. The limit at 10, shown by an arrow in the figure, further reduces by 74% the background from the $\tau^+\tau^-$ events which pass the selection requirements, leaving a final 1% contamination in our sample of candidate events. Since we expect that 23 $\tau^+\tau^-$ events were produced during our data run, there should be only 0.23 candidate $\tau^+\tau^-$ events remaining after this test.

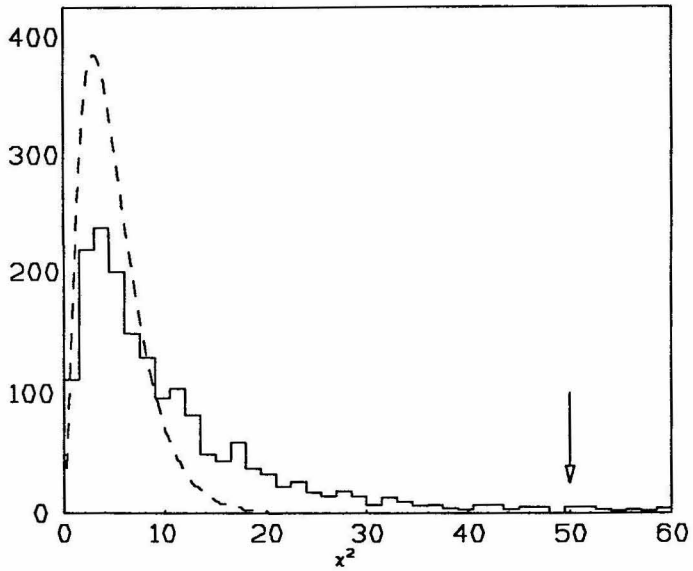

Figure 7.3. The expected χ^2 distribution for pair production of stable charged particles. The χ^2 distribution for 5 degrees of freedom is indicated by a dotted line.

7.1.4 *Testing the candidate events*

The chi-square per degree of freedom for the 13 candidate events is shown in fig. 7.5. One of the 13 selected events from the data fails the chi-square test with a value of 179 per degree of freedom. This high chi-square places it off-scale in the figure and makes the stable pair production hypothesis highly improbable. The event is shown in fig. 7.6. Its topology is consistent with a Z decay to $\tau^+\tau^-$ (so much so, in fact, that it was shown to represent a "typical" $\tau^+\tau^-$ event in another student's thesis[74]) with the subsequent tau decays $\tau^+ \rightarrow \mu^+\nu_\mu\bar{\nu}_\tau$ and $\tau^- \rightarrow e^-\nu_\tau\bar{\nu}_e$. The tracks in fig. 7.6 are back-to-back and the proposed e^- has a momentum of 17.5 GeV/c and a 17.2 GeV shower in the barrel calorimeter. The μ^+ has a momentum of 14.6 GeV/c and penetrates the full muon system.

We now discuss the details of why the $\tau^+\tau^-$ event shown in fig. 7.6 fails the chi-square test for stable pair production. If we average the momenta of the two tracks we get $\bar{p} = 16.0$ GeV/c. If we use this average momentum as the value for p in eqn. 2.2 and solve for the mass M we get a value of 42.6 GeV/c^2. The dE/dx

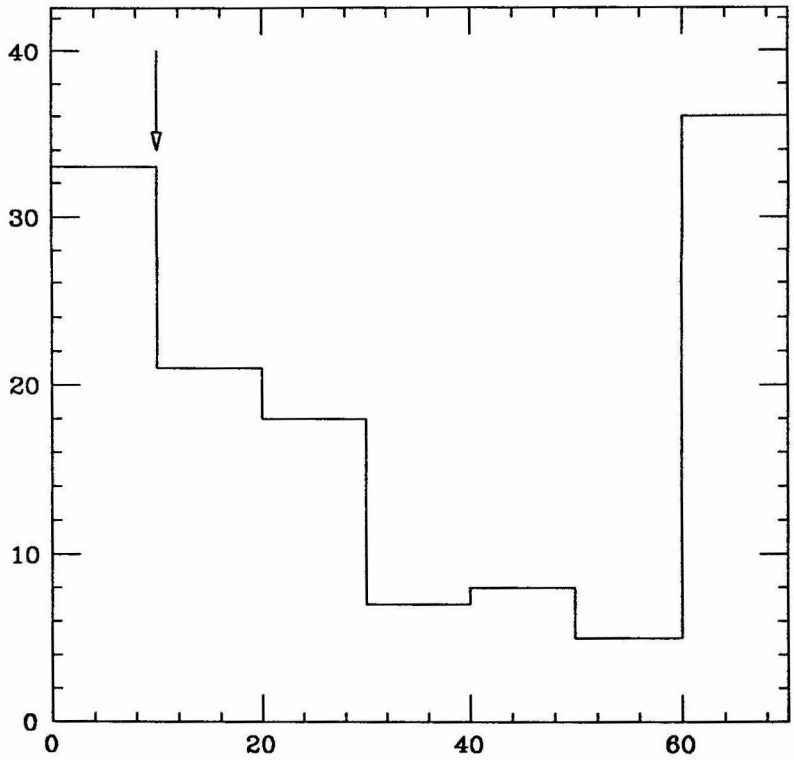

Figure 7.4. Distribution of the chi-square per degree of freedom for $\tau^+\tau^-$ events which pass the candidate event selection cuts. The overflows are included in the last bin.

measurements of 16.5 and 13.0 KeV/83.3 cm for the e^- and μ^+ respectively are consistent with the expectations for these particle types but they are also consistent with the expectations for 30 GeV/c^2 particles (see the curve showing the expected dE/dx as a function of mass in fig. 2.1). The TOF measurements for both tracks agree with the times expected for electrons or muons. Although the three systems strongly disagree as to the mass of the particles under the pair production assumption, the likelihood function still has a maximum at 41.6 GeV/c^2 where the tails of the dE/dx and momentum probability distribution functions overlap. The large $\chi^2(M)$ value for this event arises due to the fact that the TOF expected for this most probable mass is 20 sigma away from the TOF that is actually measured.

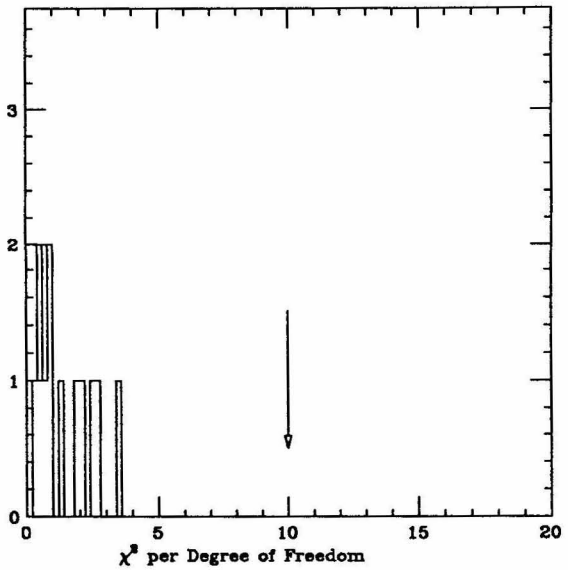

Figure 7.5. Chi-square per degree of freedom for the 13 events passing the stable pair production selection cuts. One of the 13 events has a chi-square per degree of freedom of 179 placing it off-scale in this figure. This one event is clearly separated from the other 12 events which pass the cut set at 10.

7.1.5 *The mass assignments for candidate events*

The most probable mass assignments for the 12 candidate events which pass the chi-square test are shown in fig. 7.7. The mass assignments are all less than 2 GeV/c^2, which makes these events consistent with being $\mu^+\mu^-$ events. This means that there are no events in the data that can be considered as signal events for new stable particle production.

We have designed our event selection and pair production tests in such a way as to limit the expected background in our candidate sample from Z decays to e^+e^- and $\tau^+\tau^-$ to 0.46 and 0.23 events respectively. Recall that in section 6.3.7 one cosmic ray event in the data was found to pass the candidate event selection cuts when the volume defining the e^+e^- interaction region was displaced to $3 < |z| < 50$ cm and $|r| < 1.5$ cm. This cosmic ray is eliminated by the pair production test due to the 10 ns difference in the TOF times for the tracks. The expected contribution to the

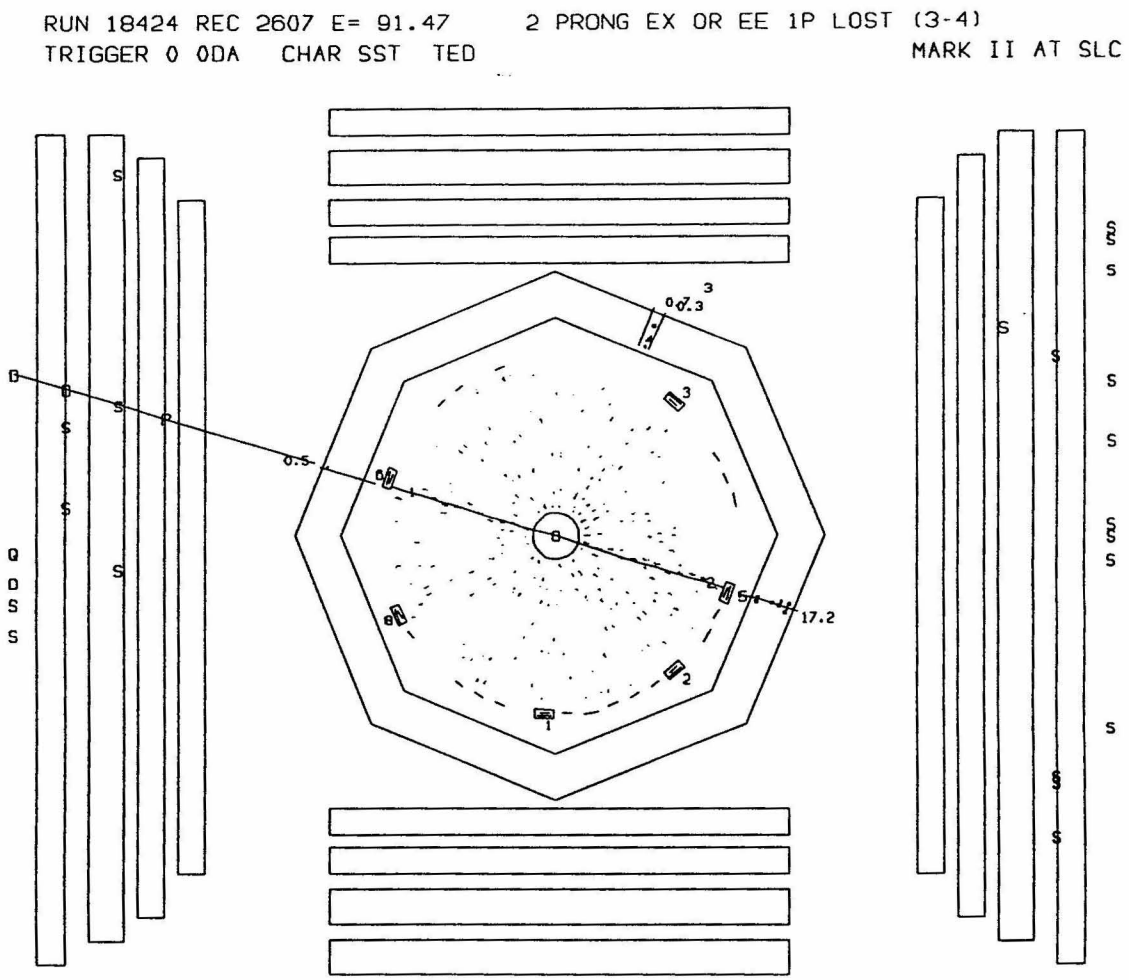

Figure 7.6. The $\tau^+\tau^-$ event in the MARK II which satisfies the candidate event selection criteria but fails the chi-square test for pair production.

background from the combination of the beam halo, synchrotron radiation, beam-gas, or cosmic ray events described in section 6.1.3 is now < 0.09 events and the contribution due to two photon events remains at < 0.03 events. In what follows we make the conservative approximation of assuming that we expect no background events from these sources in our candidate sample. We also assume that we expect no

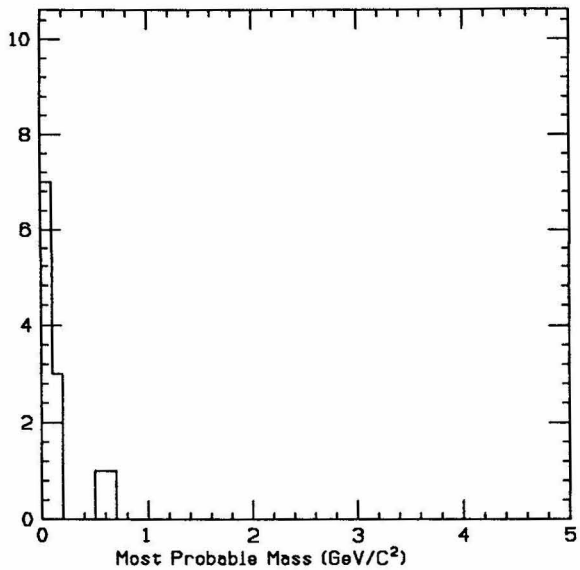

Figure 7.7. Most probable mass distribution for the 12 events passing all the cuts.

background in the mass range above 2 GeV/c^2 from $\mu^+\mu^-$ pair events. Under these assumptions, the absence of observed events with particle masses above 2 GeV/c^2 corresponds to an upper limit of 3.0 signal events at the 95% confidence-level as given by eqn. 6.6. We now need to determine in which mass ranges the different particle production models predict that more than three events from our data will pass all the cuts. It is for these ranges that production under the given model is excluded.

7.2 Final results

In this section we interpret the 95% confidence level upper limit of three signal events in terms of the expectations from the different new particle production rates discussed in Chapter 3. We begin by considering fourth generation stable charged lepton production. In this case, the expected number of signal events as a function of mass M is given by the product $N_l(M)\epsilon_l(M)$ where $N_l(M)$ is the expected number of stable charged lepton events produced during our data run and $\epsilon_l(M)$ is the efficiency for these events to pass all the cuts necessary to be considered signal events. The

expected number of events produced, $N_l(M)$, has already been determined and is given by eqn. 6.16. We will now determine the efficiency $\epsilon_l(M)$.

The efficiency $\epsilon_l(M)$ is determined by finding the percentage of Monte Carlo simulated stable charged fourth generation lepton pair production events that remain after the candidate event selection, the pair production test and the 2 GeV/c^2 limit on the most probable mass assignment have been applied. This efficiency is shown as a function of particle mass in fig. 7.8. From the figure, we see that the efficiency rises from 0.06 at 1 GeV/c^2 to 0.56 at 5 GeV/c^2 where the effect of the 2 GeV/c^2 minimum requirement on the most probable mass becomes small. The systematic error at each point is found by shifting the values and resolutions of the TOF, dE/dx, and momentum measurements by one standard deviation so as to reduce the efficiency (see Appendix B for a complete description of this procedure). This error is of order 1% for masses above 20 GeV/c^2. An additional 2% systematic error is also included to account for uncertainties in the lepton production Monte Carlo model. The error bars in fig. 7.8 represent both of these sources of systematic error added in quadrature.

A slow increase in the efficiency $\epsilon_l(M)$ is observed above 10 GeV/c^2. This is due to the fact that the angular distribution of the differential cross-section for e^+e^- annihilation to two spin 1/2 fermions near the Z pole, given by eqn. 3.10, becomes isotropic for higher fermion masses, i.e., as $\beta \rightarrow 0$, a greater proportion of events are produced in the angular region of the detector used for this search.

The product $N_l(M)\epsilon_l(M)$ that gives the number of fourth generation stable charged lepton events expected in our data as a function of lepton mass M is shown in fig. 7.9(a). The dotted curve is the number of events, assuming that all of our statistical and systematic errors conspire to reduce the expectation. These errors include the systematic and statistical errors on $N_l(M)$ and the systematic errors on the efficiency for stable pairs to pass all the requirements as discussed above. The net reduction is about 10% in the 2 GeV/c^2 mass range and falls to about 5% above 15 GeV/c^2. The upper and lower limits on stable heavy lepton production can be

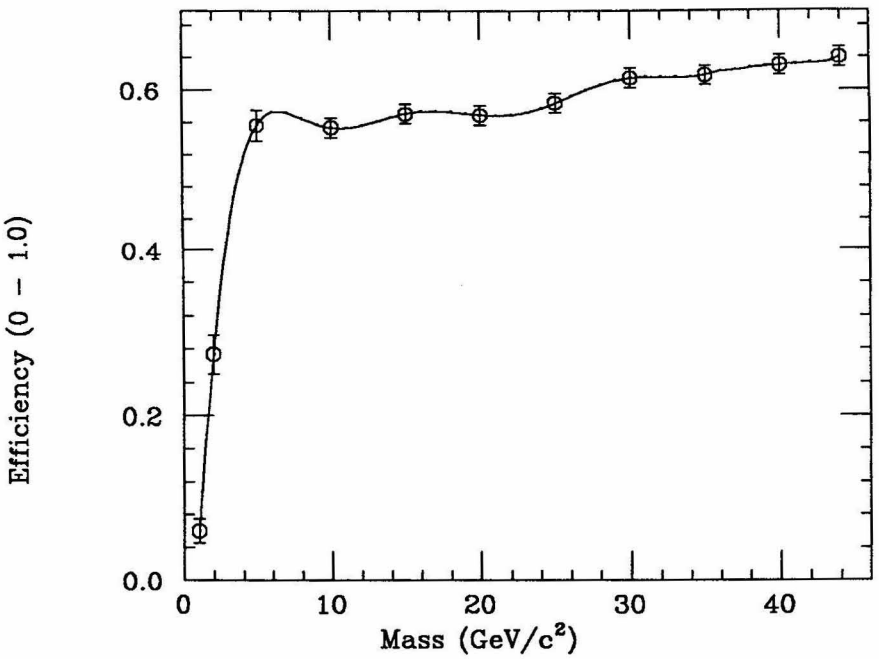

Figure 7.8. The efficiency of candidate events to pass all the requirements, $\epsilon_l(M)$, plotted as a function of particle mass.

read from the intersection of the dotted curve describing the expectations with the upper limit of 3 observed events. This direct search excludes the production of stable leptons with masses between 2.0 and 36.3 GeV/c^2 as indicated in fig. 7.9(a). The analysis and limits presented also apply to stable mirror fermions as they have the same total production cross-section as a function of mass as the standard leptons (see section 3.8).

The above analysis may be extended to set a limit on the possible masses of supersymmetric scalar leptons. Their production rate from Z decays, assuming that the left- and right-handed scalar leptons, $\tilde{l}_{\rm L}$ and $\tilde{l}_{\rm R}$, are degenerate in mass, is given by eqn. 3.36. Using this rate and a decay angular distribution proportional to $\sin\theta$ in the above analysis, we exclude the production of stable scalar leptons with masses between 2.0 and 32.6 GeV/c^2 as shown in fig. 7.9(b).

Finally, we can exclude new stable charged pair production for masses below

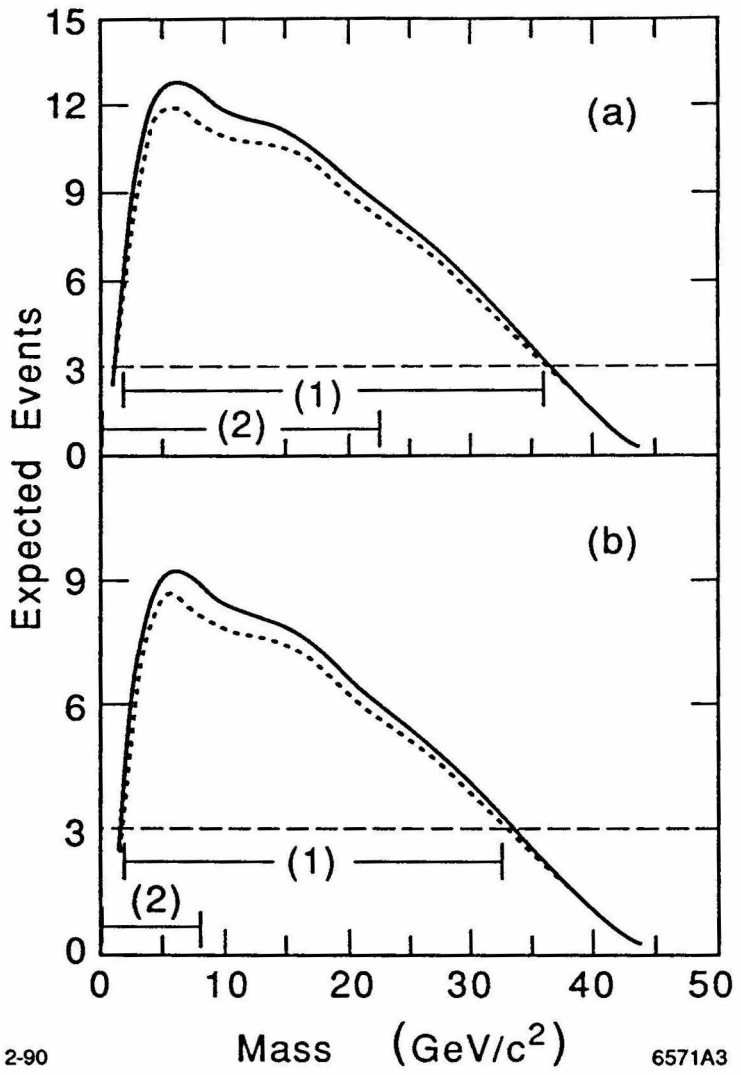

Figure 7.9. The expected number of (a) stable heavy lepton and (b) stable scalar lepton events which pass the selection and identification requirements described in the text. Dotted lines mark the lower bounds obtained by the inclusion of statistical and systematic errors. Dashed lines show the 95% confidence level upper limits of 3.0 events detected in the reported data sample at the SLC. Also indicated are the mass regions for which production is excluded by (1) the direct and (2) the indirect search analyses described in the text.

2 GeV/c^2 down to m_μ, the mass of the muon, using the results of the indirect search method discussed in section 6.5.4. These mass regions are indicated in fig. 7.9.

Chapter 8

Conclusions

In conclusion, we have performed a general search for the production in pairs of new stable charged particles in the decays of the intermediate vector boson Z with the MARK II detector at the SLAC Linear Collider. No candidates for new particles have been found.

We have set a limit[75] excluding the production of pairs of stable fourth generation charged leptons and stable mirror fermions with masses between the muon mass and 36.3 GeV/c^2 at the 95% confidence level. This limit supersedes the best limits set previously by the JADE[46] Collaboration at PETRA and the and TOPAZ[45] Collaboration at TRISTAN. The new and previous limits are shown in fig. 8.1.

We have also excluded[75] at the 95% confidence level the production of pairs of stable supersymmetric scalar leptons with masses between the muon mass and 32.6 GeV/c^2. This mass limit is obtained under the assumption that the left- and right-handed scalar leptons are degenerate in mass. It supersedes the lower limit of 26.3 GeV/c^2 set by TOPAZ.[45]

Our motivation for conducting the search for new stable charged particles is twofold. First, the copious production of the Z boson in the clean e^+e^- environment of the SLC opened up a new energy range in which a general search for new particle production is, in some senses, an obligation. The search for the Z decays to a stable charged particle-antiparticle pair is part of this general search. Second, the current

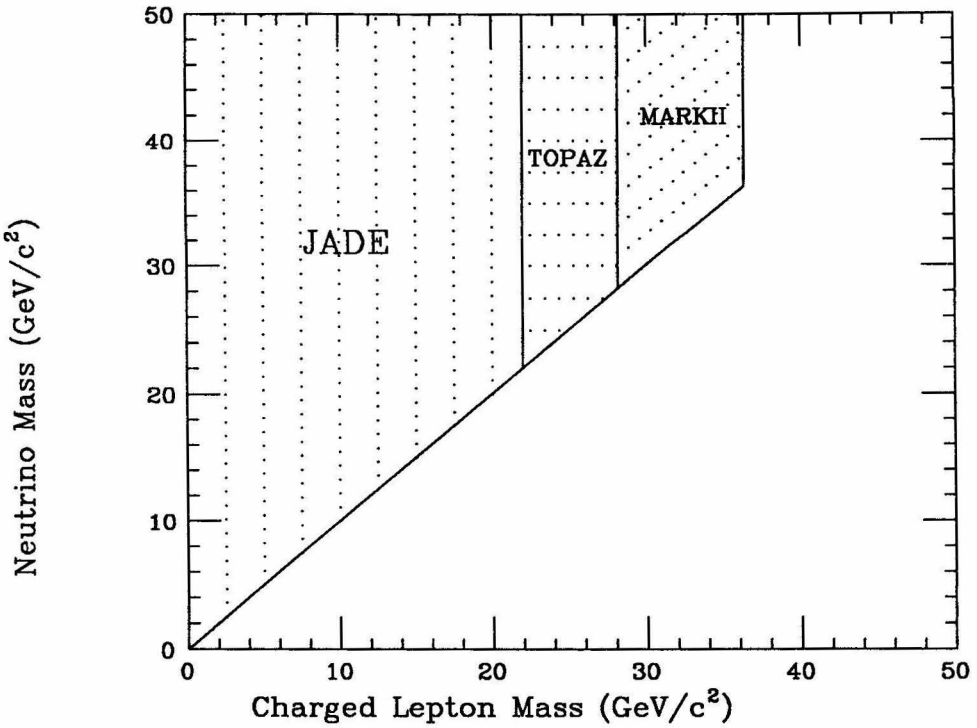

Figure 8.1. Mass limits on fourth generation stable charged leptons.

theories of particle physics provide few limitations regarding the possible existence of new stable charged particles. On the contrary, we have shown that under certain circumstances, the left-right symmetric and supersymmetric extensions of the Standard Model of particle interactions actually predict the existence of new stable charged particles in the form of mirror leptons and supersymmetric scalar leptons. We have also shown that a new stable charged particle is also possible within the Standard Model in the form of a fourth generation charged lepton with a mass which is less than that of the fourth generation neutrino.

Our search for a stable fourth generation charged lepton complements the many other searches for the quarks and leptons of a possible fourth generation. The results of the searches with the highest mass reach for fourth generation quarks and leptons are reported in Chapter 2 of this thesis. The combination of the search results from SLC and LEP basically exclude, at the 95% confidence level, the possible existence

of stable or unstable fourth generation neutrinos, unstable fourth generation charged leptons, and fourth generation charge -1/3 quarks (b') with masses that are smaller than one half the Z boson mass. Especially significant is that the combination of the measurements of the Z boson resonance parameters at SLC and LEP specify the number of light neutrino generations in the Standard Model to be $N_\nu = 2.95 \pm 0.11$. Searches for the top quark at SLC and LEP have also set a lower limit on its mass of $M_Z/2$, but the best lower limit on the top quark mass has been set at 77 GeV/c^2 by the CDF Collaboration[8] working at the Tevatron at Fermilab. The remaining gap between the lower mass limit of 36.3 GeV/c^2 for stable charged fourth generation leptons set in this thesis and half the Z mass should soon be closed by experimenters at LEP.

The mass limits reported above force the search for the possible existence of fourth generation quarks and leptons to still higher energies. Unfortunately, we do not know if future searches at higher energies will find anything beyond the three generations observed so far. We have shown that the Standard Model does not provide us with any information regarding the mass values of any of the quarks and leptons including those of any possible new generation. In fact, the number of generations is not specified in the theory. Therefore, the search for new generations is driven by a lack of knowledge rather than motivated by theoretical predictions.

Searches for new particles with masses above the current limits of $M_Z/2$ can soon be carried out at the planned upgrade of LEP to LEP-II where the maximum center-of-mass e^+e^- collision energy will be about 200 GeV. As discussed in the introduction to Chapter 4, the search beyond this energy scale in e^+e^- collisions will require the construction of a Next Linear Collider.[76] The SLC was designed to develop and test this new collider concept. This search and, in fact, all of the Z boson studies at the SLC are a testament to the physics potential of such a collider.

The search for new heavy particles can also be conducted in the $p\bar{p}$ collisions of the Fermilab Tevatron or the pp collisions of the Superconducting Super Collider

(SSC). The proposed 40 TeV center-of-mass energies of the SSC will provide the highest energies yet for new heavy particle production. In addition to evidence for the possible production of new stable charged particles, one hopes to find evidence for any new quarks and leptons or the Higgs particle or supersymmetric particles. It is through the discovery of such particles that our understanding of the interactions between the fundamental particles of matter can be further enriched.

Appendix A

The Monte Carlo Simulations

The search analysis presented in this thesis was developed using Monte Carlo simulations of Z decays to stable charged fourth generation charged lepton-antilepton pairs. The physics of the decays was simulated using the LUND 6.3 Monte Carlo generator[77] driven by LULEPT,[78] a MARK II specific program which allows the masses and lifetimes of the final state leptons to be specified. This allowed the generation of the simulated pair production of stable charged leptons at masses of 1, 2, 5, 10, 15, 20, 25, 30, 35, 40 and 44 GeV/c^2. The detector response was also simulated for these events and the effects of beam related backgrounds were included.

The simulation of beam backgrounds for the stable charged lepton events was accomplished by mixing the data from random SLC beam crossings with the simulated data. These random events were sampled through the data collection run at arbitrary beam crossings when the data acquisition is started whether or not there is a valid trigger. Typically, none of the charged track, total energy or luminosity triggers are satisfied by these events. The signals read out for the detector subsystems on random events are taken to be representative of the electronics noise or low energy accelerator backgrounds signals present at every beam crossing.

In addition to the simulations of new stable charged particle production, simulations of e^+e^-, $\mu^+\mu^-$ and $\tau^+\tau^-$ events were also made so that these processes could be studied as background. The $\mu^+\mu^-$ and $\tau^+\tau^-$ events were generated by LULEPT as

described above. The generator used for simulating e^+e^- events was that of Berends, Hollik, and Kleiss. Its general features are discussed in ref. 79.

In this analysis, Monte Carlo simulated data was used to find the efficiency for both signal and background events to pass the event selection requirements as well as the chi-square pair production test and 2 GeV/c^2 minimum mass requirement. It was further used to check the resolution of the maximum likelihood mass assignment technique. Some of the event selection requirements, as well as the mass assignment, depend on the drift chamber momentum, dE/dx, and the TOF measurements. The verification that these measurements are in agreement between the simulated data and real data collected at the SLC is presented in the following sections.

A.1 The vertex constrained momentum measurement

The e^+e^- interaction point (IP), or vertex, can be included as a constraint in the charged particle track reconstruction. The advantage of including the vertex in the fit is that the increased lever-arm due to the 19.2 cm distance from it to the first of the 72 drift chamber layers results in a roughly 30% improvement in the momentum resolution. It is not included in general because there is no *a priori* knowledge as to whether a given track actually originated at the IP or came from the subsequent decay of a particle that had traveled away from the IP. The stable particles that we are searching for, however, come from the IP by definition so we can take advantage of the improved momentum resolution of the vertex constrained fit in this analysis.

The error on the location of the IP due to uncertainties in the beam positions is taken to be 200 μm in both x and y, which is comparable to the drift chamber track position resolution of 170 μm. The resolution of the location of the IP is taken to be 1 mm in z. It was found that these errors must be included in the fit to get the proper agreement in the momentum resolution between the data and the Monte Carlo simulation.

The resolution, $\sigma_{\frac{1}{p}}$, of the inverse of the vertex constrained momentum measure-

ment p, is that quantity for which the function

$$f(p) = \frac{\frac{1}{p_{measured}} - \frac{1}{p_{expected}}}{\sigma_{\frac{1}{p}}}, \tag{A.1}$$

forms a unit width Gaussian distribution centered at zero for the data. For $\mu^+\mu^-$ pairs we expect, to zero'th order in the radiative corrections, that $p_{expected} = E_{cm}/2$, where $E_{\rm cm}$ is the center of mass energy in the e^+e^- collision (this is not the case for e^+e^- pairs where final state radiation is known to have a significant effect on the momentum distribution). The transverse momentum p_t is defined as $p_t = \sqrt{p_x^2 + p_y^2}$. A number proportional to the error on the inverse of the transverse momentum is determined as part the MARK II track fitting procedure. The constant of proportionality is found to be 1.3 for $\mu^+\mu^-$ pairs at the SLC. This error on the inverse of the transverse momentum can be converted to the error on the momentum from the relation

$$p = p_t\sqrt{1+s^2}, \tag{A.2}$$

where s is the dip angle defined as $\frac{p_z}{p_t}$. From eqn. A.2 we have

$$\sigma_{\frac{1}{p}} \approx \sigma_{\frac{1}{p_t}} \frac{1}{\sqrt{1+s^2}}. \tag{A.3}$$

We now use this equation to plot the distribution given by eqn. A.1 for $\mu^+\mu^-$ pairs at the SLC as shown in fig. A.1. The agreement between the vertex constrained momentum measurements for the data and Monte Carlo simulation is evident in the figure. Also evident is the fact that the resolution is of the proper magnitude as reflected by the unit width of distribution shown in fig. A.1(c).

A.1.1 Effects of low particle velocity on tracking

The standard MARK II track reconstruction code assumes that the particles are moving with velocity $\beta = 1$. This would not be the case for pair production of very

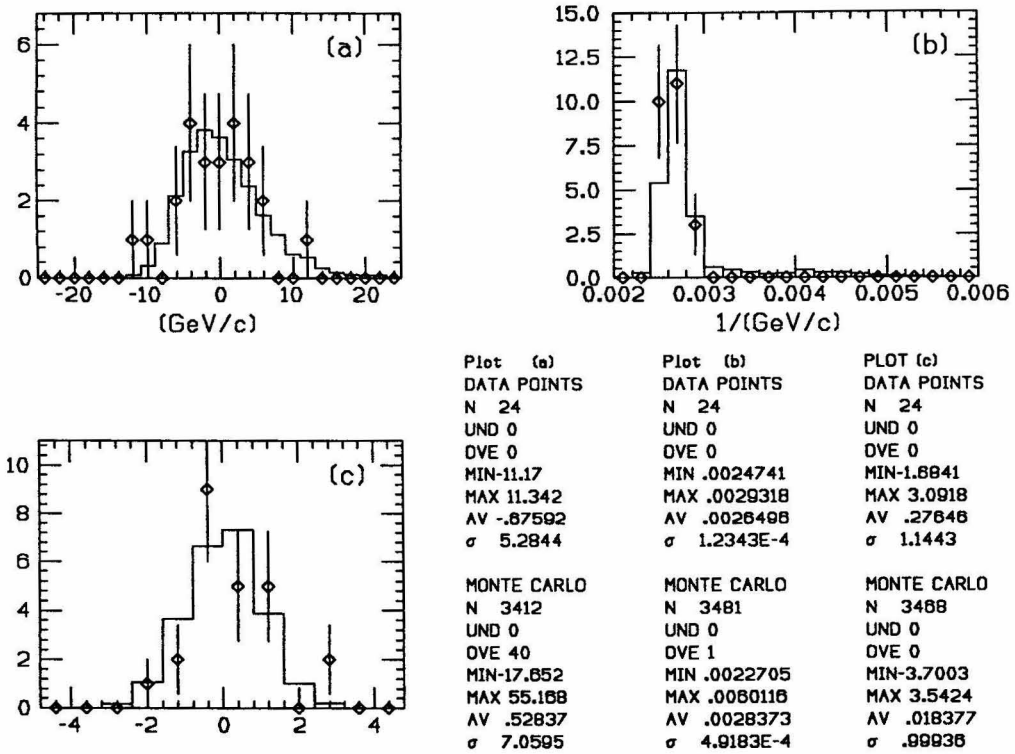

Figure A.1. The drift chamber vertex constrained momentum measurement and error for $\mu^+\mu^-$ pairs at the SLC that are required to hit the TOF system. The SLC data are shown as points and the histogram is Monte Carlo simulation. Ordinate labels refer to the data. The three figures show (a) $p - p_{expected}$, (b) $\sigma_{1/p}$ and (c) $(1/p - 1/p_{expected})/\sigma_{1/p}$ where $p_{expected} = E_{cm}/2$.

heavy particles. The effect of the lower actual velocity does not become significant until the particle masses approach the beam energy. For example, at a particle mass of 44 GeV/c^2 the velocity is $\beta = 0.26$. This leads to a flight time of 20 ns to traverse the drift chamber as opposed to a 5 ns time for $\beta = 1$ particles. The difference due to flight time between the hits on the first and last layer of the chamber is now significant when compared to the drift times of the ionization electrons to the wires. This average drift speed is 52 μs/ns and coupled with the maximum drift distance of 3.3 mm as shown in fig. 4.4 gives drift times of 660 ns with the average being half this number. The net result of these time differences at 44 GeV/c^2 is a 13% degradation

in the momentum resolution and a 1% shift in the mean momentum value. This effect becomes more severe above 44 GeV/c^2, but, due to the low expected event rate in our data for this mass range, it can be neglected in this analysis.

A.2 The dE/dx measurement

The dE/dx system performance has been determined from the SLC data and is simulated in the Monte Carlo. In fig. A.2 is shown the fit of the expected dE/dx curve to the data covering the full range of $\beta\gamma$. The fit was performed[80] by Rick Van Kooten using SLC data. In addition to protons at low $\beta\gamma$, minimum ionizing pions and cosmic rays on the relativistic rise, the $\mu^+\mu^-$ and e^+e^- data from the SLC were included in the fit to constrain the relativistic rise and plateau region for $\beta\gamma$ values greater than about 2. The resultant agreement in the absolute scale of the dE/dx measurement and its resolution for the data and Monte Carlo for selected $\mu^+\mu^-$ events at SLC is shown in fig. A.3. The corresponding plots for e^+e^- events are shown in fig. A.4.

The dE/dx FADC system saturates at ionization levels above 4 KeV/8.33 cm. For particle masses in excess of 35 GeV/c^2, a greater number of saturated hits are expected than for minimum ionizing tracks. Because of this, no limit is imposed on the number of saturated hits used in the truncated dE/dx sample to avoid throwing out new signal events with large ionization energy loss.

A.3 The TOF measurement

The TOF measurement error in the Monte Carlo is taken directly from the parameterization of eqn. 5.4 as shown in fig. 5.10 and fig. 5.12. The TOF efficiency shown in fig. 5.14 is also included in the Monte Carlo simulation. For the case in which only one phototube fires, parameters of eqn. 5.4 shown in fig. 5.13 are used.

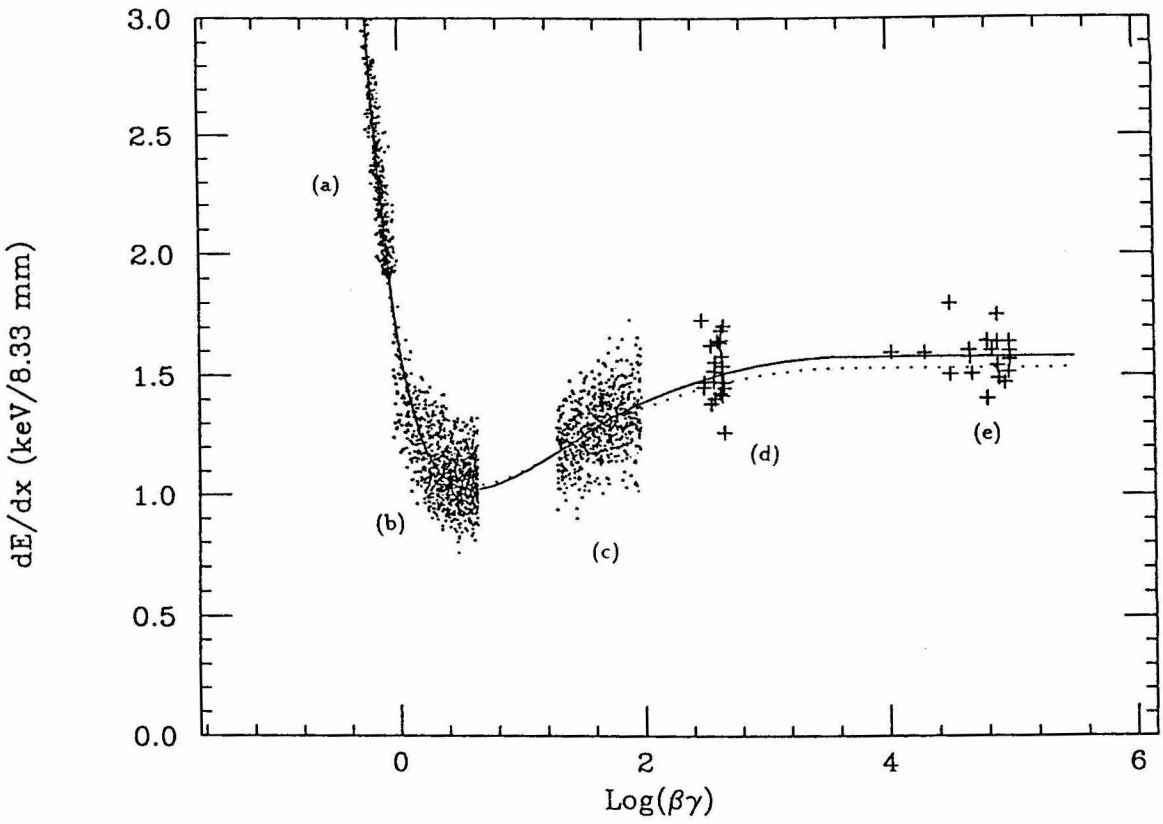

Figure A.2. Fit of the dE/dx theory curve to the SLC data covering the full region of $\beta\gamma$. The solid curve is the fit obtained from the SLC data. The dotted line shows the theory curve before the e^+e^- and $\mu^+\mu^-$ data were included in the fit. The data selected are: (a) protons, (b) minimum ionizing pions, (c) cosmic rays, (d) $\mu^+\mu^-$ pairs and (e) e^+e^- pairs.

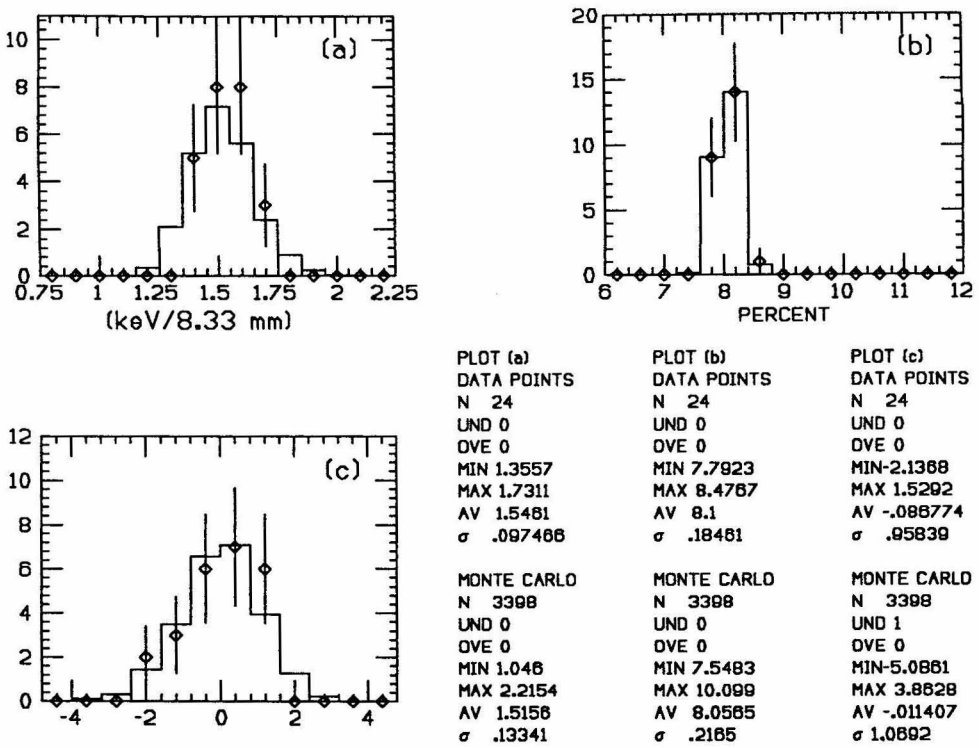

Figure A.3. The dE/dx measurement and resolution for $\mu^+\mu^-$ pairs from the SLC data (points) and Monte Carlo (histogram). Both tracks in an event are required to hit the TOF system. The three figures show: (a) $dE/dx_{measured}$ (b) dE/dx resolution ($\sigma_{dE/dx}$) and (c) $(dE/dx_{measured}\text{-}dE/dx_{expected})/\ \sigma_{dE/dx}$. The ordinate labels refer to the data.

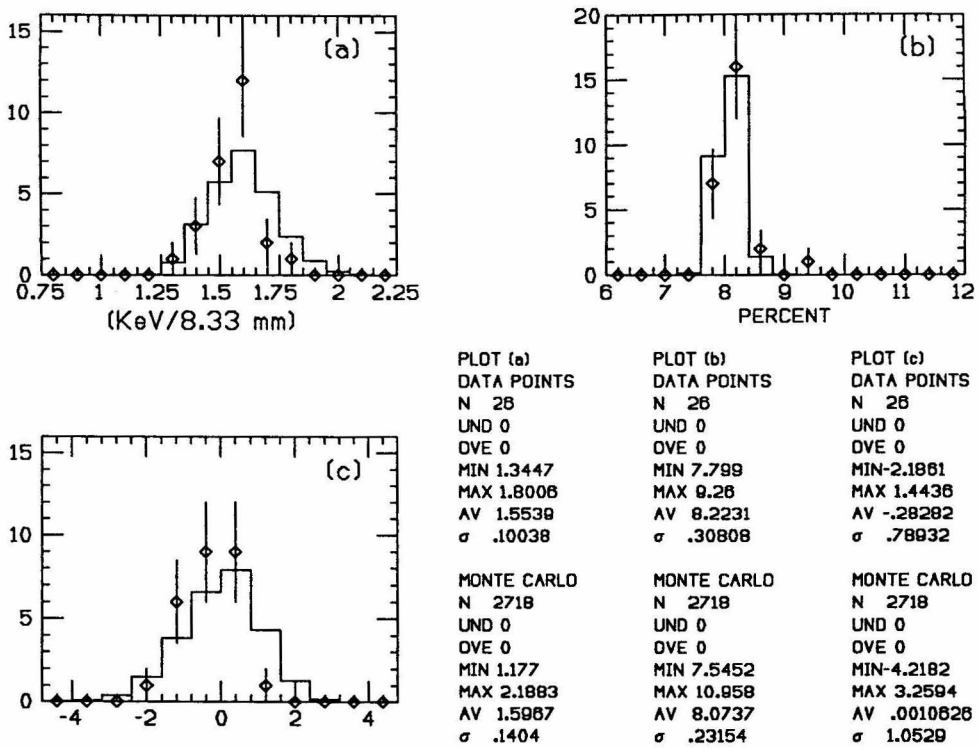

Figure A.4. The dE/dx measurement and resolution for e^+e^- pairs from the SLC data (points) and Monte Carlo (histogram). Both tracks in an event are required to hit the TOF system. The three figures show: (a) $dE/dx_{measured}$ (b) dE/dx resolution ($\sigma_{dE/dx}$) and (c) $(dE/dx_{measured}\text{-}dE/dx_{expected})/\ \sigma_{dE/dx}$. The ordinate labels refer to the data.

Appendix B

Systematic Errors

The mass limits for new stable charged particles set in this thesis depend directly on the expected efficiency for detecting these particles. We used Monte Carlo simulations to find the efficiency as a function of particle mass for events to pass all of the candidate event selection requirements as well as the pair production test and the 2 GeV/c^2 lower limit on the most probable mass. These requirements and tests depend largely on the TOF, dE/dx, and momentum measurements, and their associated errors. Therefore, any systematic error in these measurements resulting from the improper tuning of the Monte Carlo simulation to the data will be transferred to the systematic error in the efficiency of events to pass all the requirements. To estimate the magnitude of these systematic errors, we shift the values and resolutions of the TOF, dE/dx, and momentum measurements together by 1 σ so as to reduce the efficiency for events to pass the requirements. This will be demonstrated below after we have determined what a 1 σ shift would be for each system.

First we examine the drift chamber momentum measurement. From fig. A.1(a) in Appendix A we see that the error on the mean is $\sigma/\sqrt{N} = 5.2844/\sqrt{24} = 1.08$ GeV/c or about 3% of the beam energy. This is also the extent to which the mean values of the momentum measurement distributions differ between the data and Monte Carlo as shown in fig. A.1(a). Therefore, we take this as our systematic uncertainty in the momentum scale. We take the systematic uncertainty in $\sigma_{\frac{1}{p}}$ to be equal to ± 0.0005.

This conservatively large error is based on the data in fig. A.1(b).

The error in the dE/dx scale is found from the data in fig. A.3(a). We see that the error in the mean for the data, $\sigma/\sqrt{N}$, is $0.097/\sqrt{24}$ or about 2% of the dE/dx measurement. The difference between the mean values of the dE/dx measurement distributions for the data and Monte Carlo is also about 2%. The error on the dE/dx resolution is taken to be ± 0.02. This large value is chosen is to account for the fact that we do not make a cut on the number of saturated hits for each measurement. Therefore, as in the case for e^+e^- pairs in fig. A.4(b), we sometimes get a track with poorly measured dE/dx as the one entry in that plot with an error of 9.5%.

For the TOF system we use errors of $\pm$20ps for both the time-of-flight value and resolution. These errors were determined when finding the fit parameters associated with fig. 5.10. We also take a 1% error on the TOF efficiency shown in fig. 5.14.

B.1 Systematic error in event detection efficiency

We now find the effect of the above systematic errors on the efficiency of stable charged pair events to pass all the requirements. As an example, consider a candidate event with particles of mass 5 GeV/c^2. From fig. 2.1 we see that if the TOF, dE/dx, and momentum measurements were all systematically high, we would assign a mass that was systematically low in this case. Furthermore, if the corresponding resolutions were systematically low, we would have increased faith that the systematically high measurements were correct. This would cause more events to fail the 2 GeV/c^2 lower limit on most probable mass (the resolution of the most probable mass assignment causes the 5 GeV/c^2 mass distribution to have a tail that extends below 2 GeV/c^2 as shown in fig. 7.1). To find out the actual magnitude of this effect we simply shift the TOF, dE/dx, and momentum measurement values, together with their corresponding resolutions in the Monte Carlo simulation by the amounts found above for each system and compare the number of events passing all of the cuts to the same quantity when no shift is made. For the 5 GeV/c^2 case, we find that 3.4% fewer events pass the

requirements when things are shifted. This then is taken as the systematic error in the efficiency for 5 GeV/c^2 stable pairs to pass the requirements.

The above procedure was carried out for other masses and the results are included in the error bars for the Monte Carlo simulated data shown in fig. 7.8.

References

1. See, for example, C. Quigg, *Gauge Theories of the Strong, Weak, and Electromagnetic Interactions*, Benjamin-Cummings (1983); or
V. Barger and R. Phillips. *Collider Physics*, Addison-Wesley (1987); or
Particle Physics, A Los Alamos Primer, edited by N.G. Cooper and G.B. West. Cambridge University Press (1988).

2. J. Va'Vra *et al.*, Nucl. Instrum. Methods **203**, 109 (1982).

3. U. Fano, Ann. Rev. Nucl. Sci. **13**, 1 (1963).

4. J. Dorfan, Z^0 *Physics at the SLC*, Invited lectures at Banff Summer Institute and Nato Advanced Study Institute. SLAC-PUB-4816 (1989).

5. W. Marciano and H. Pagels, Phys. Reports **36,** 137 (1978).

6. Particle Data Group, G.P. Yost *et al.*, Phys. Lett. **204B,** 1 (1988).

7. S. Raby, R. Slansky, and G. West, Particle Physics and the Standard Model in *Particle Physics, A Los Alamos Primer*, edited by N.G. Cooper and G.B. West. Cambridge University Press, (1988).

8. CDF Collab., F. Abe *et al.*, Phys. Rev. Lett. **64,** 142 (1990).

9. See, for example, R.P. Feynman, *Quantum Electrodynamics*, New York, Benjamin, Inc., (1962). For the original papers of Feynman as well as others, see *Selected Papers on Quantum Electrodynamics*, edited by J. Schwinger, Dover Publications (1958).

10. S.L. Glashow, Nucl. Phys. **22**, 579 (1961);
S. Weinberg, Phys. Rev. Lett. **19,** 1264 (1967);
A. Salam and J.C. Ward, Phys. Lett. **13**, 168 (1964).

11. R.E. Shrock and L.L. Wang, Phys. Rev. Lett. **41,** 1692 (1978).

12. ALEPH Collab., D. Decamp *et al.*, Phys. Lett. **246B,** 306 (1990).

13. E. Eichten, I. Hinchliffe, K. Lane and C. Quigg, *Higgs Bosons at the SSC*, Presented at DPF Summer Study on Design and Utilization of the Superconducting Super Collider. Snowmass, Colo., 1984. Published in Snowmass Summer Study (1984).

14. L. Wolfenstein, Comm. Nucl. Part. Phys. **14**, 135 (1985).

15. N. Cabibbo, Phys. Rev. Lett. **10**, 531 (1963).

16. B.C. Barish and R. Stroynowski, Phys. Reports **157**, 1 (1988).

17. K.K. Gan, Phys. Lett. **209B**, 95 (1988);
ARGUS Collab., H. Albrecht *et al.*, Phys. Lett. **185B**, 228 (1987);
CLEO Collab., T. Bowcock *et al.*, Phys. Rev. **D41**, 805 (1990);
D.H. Miller, Phys. Rev. **D23**, 1158 (1981).

18. M. Dine and J. Sapirstein, Phys. Rev. Lett. **43**, 668 (1979).

19. MARK II Collab., G.S. Abrams *et al.*, Phys. Rev. Lett. **63**, 2173 (1989).

20. ALEPH Collab., D. Decamp *et al.*, Phys. Lett. **235B**, 399 (1990).

21. DELPHI Collab., A. Abreu *et al.*, Phys. Lett. **241B**, 425 (1990).

22. L3 Collab., B. Adeva *et al.*, Phys. Lett. **237B**, 136 (1990).

23. OPAL Collab., M.Z. Akrawy *et al.*, Phys. Lett. **235B**, 379 (1990).

24. A. Buijus, *New Particle Searches at LEP*. Proceedings of the Slac Summer Institute, July (1990).

25. R.E. Shrock, Phys. Rev. **D24**, 1275 (1981);
Y.S. Tsai, Phys. Rev. **D4**, 2821 (1971);
Y.S. Tsai, Phys. Rev. **D19**, 2809 (1979).

26. The MARK II Collab., P. R. Burchat *et al.*, Phys. Rev. **D41**, 3542 (1990).

27. R. Van Kooten and C.K. Jung, Mark II/SLC Note #254 (1989). Presented at the Annual Meeting of the Division of Particles and Fields of the American Physical Society, Houston, Tex., Jan. 3-5 (1990).

28. MARK II Collab., G.S. Abrams, *et al.*, Phys. Rev. Lett. **63,** 2447 (1989).

29. The MARK II Collab., C. K. Jung *et al.*, Phys. Rev. Lett. **64,** 1091 (1990).

30. Mark II Collab., C. Wendt *et al.*, Phys. Rev. Lett. **58**, 1810 (1987).

31. ALEPH Collab., D. Decamp *et al.*, Phys. Lett. **236B,** 511 (1990).

32. OPAL Collab., M.Z. Akrawy *et al.*, Phys. Lett. **240B,** 250 (1990).

33. C. Albajar *et al.*, Z. Phys. **C 37**, 505,(1988).

34. V. Barger *et al.*, Phys. Rev. **D30,** 947 (1984).

35. W. Hou and R.G. Stuart, Phys. Rev. Lett. **62,** 617 (1989);
V. Barger *et al.*, Phys. Rev. Lett. **57,** 1518 (1986).

36. OPAL Collab., M.Z. Akrawy *et al.*, Phys. Lett. **236B,** 364 (1990).

37. DELPHI Collab., A. Abreu *et al.*, Phys. Lett. **242B,** 536 (1990).

38. J.C. Pati and A. Salam. Phys. Lett. **58B,** 333 (1975).

39. J. Maalampi and M. Roos, Phys. Reports **186,** 53 (1985).

40. T. Banks and M. Karliner, Nuc. Phys. B**281,** 399 (1987);
G. Senjanović, F. Wilczek, and A. Zee, Phys. Lett. **141B,** 389 (1984).

41. H. E. Haber and G. L. Kane, Phys. Reports **117,** 75 (1985).

42. J. Weiss *et al.*, Phys. Lett. **101B,** 439 (1981).

43. New particle searches at PEP and PETRA are summarized by K. Hagiwara and S. Komamiya, KEK-TH 145 (1987).

44. VENUS Collab., K. Abe *et al.*, Phys. Rev. Lett. **61,** 915 (1988)

45. I. Adachi *et al.*, Phys. Lett. **244B,** 352 (1990).

46. JADE Collab., W. Bartel *et al.*, Z. Phys. **C29**, 505 (1985).

47. JADE Collab., W. Bartel *et al.*, Phys. Lett. **152B,** 392 (1985).

48. CDF Collab., F. Abe *et al.*, Phys. Rev. Lett. **63,** 1447 (1989).

49. B. Andersson *et al.*, Phys. Reports **97,** 31 (1983).

50. R.D. Field and S. Wolfram, Nuc. Phys. B**213,** 65 (1983).

51. T. Sjöstrand, Nuc. Phys. B**289,** 810 (1987).

52. T.D. Gottschalk and M.P. Shatz, Phys. Lett. **150B,** 451 (1985).

53. G. Marchesini and B.R. Webber, Nuc. Phys. B**238,** 1 (1984);
B.R. Webber, Nuc. Phys. B**238,** 492 (1984).

54. T.D. Gottschalk and D. Morris, Nuc. Phys. B**288,** 729 (1987).

55. MARK II Collab., G. S. Abrams *et al.*, Phys. Rev. Lett. **63,** 1558 (1990).

56. MARK II Collab., G. S. Abrams *et al.*, Phys. Rev. Lett. **64,** 1334 (1990).

57. J. H. Kühn, A. Reiter, and P. M. Zerwas, Nuc. Phys. B**272,** 560 (1986).

58. MARK II Collab., S. Komamiya *et al.*, Phys. Rev. Lett. **64,** 987 (1990).

59. J. Alexander *et al.*, Phys. Rev. **D37,** 56 (1988).

60. R.N. Cahn, Phys. Rev. **D36,** 2666 (1987).

61. W. J. Marciano and A. Sirlin, Phys. Rev. **D22,** 2695 (1980)

62. T. Kobayashi and M. Kuroda, Phys. Lett. **134B,** 271 (1984).

63. M. Sands, SLAC-PUB-121 (1970).

64. B. Richter, SLAC-Report-229 (1980);
D.L. Burke, SLAC-PUB-4851 (1989).

65. MARK II Collab., G. S. Abrams *et al.*, Nucl. Instrum. Methods **A281**, 55 (1989).

66. Manufactured by Kyowa Gas Chemical Industry, Japan;
T. Inagaki and R. Takashima, Nucl. Instrum. Methods. **201**, 511 (1982).

67. E. Soderstom, M. Nelson, and R. Stroynowski, MarkII/SLC Note #84 (1984).

68. J. E. Grund, IEEE Trans. Nucl. Sci. NS-27, 1, 599 (1980);
J. S. Brown, *et al.,* Nucl. Instrum. Methods. **221**, 503 (1984).

69. M. Breidenbach, *et al.,* IEEE Trans. Nucl. Sci. NS-25, 1, 706 (1978).

70. W. Braunschweig *et al.,* Nucl. Instrum. Methods. **134**, 261 (1976).

71. F.A. Berends, P.H. Daverveld, and R. Kleiss, Comp. Phys. Comm. **C40**, 309 (1986).

72. J. Mathews and R.L. Walker, *Mathematical Methods of Physics*, Benjamin-Cummings (1970).

73. B.W. Lindgren, *Statistical Theory*, Macmillan (1976).

74. J.A. Nash, Ph.D. thesis, SLAC-Report-356 (1990).

75. MARK II Collab., E. Soderstrom *et al.,* Phys. Rev. Lett. **64,** 2980 (1990).

76. F.Gilman, SLAC-PUB-5204 (1990).

77. M. Bengtsson and T. Sjöstrand, Comp. Phys. Comm. **43**, 367 (1987).

78. D. Stoker, Phys. Rev. **D39,** 1811 (1989);
D. Stoker, MarkII/SLC Note #161 (1986).

79. F. A. Berends, W. Hollik, and R. Kleiss, Nuc. Phys. B**304,** 712 (1988).

80. R. Van Kooten. Internal MARK II note decribing data selection and fitting in detail.